Cardiac Calcium Transport Regulation Probed by Electron Paramagnetic Resonance Spectroscopy

A DISSERTATION

SUMBITTED TO THE FACULTY OF THE GRADUATE SCHOOL

OF THE UNIVERSITY OF MINNESOTA

BY

Kurt Daniel Torgersen

IN PARTIAL FULFILLMENT OF THE REQUIREMENTS

FOR THE DEGREE OF

DOCTOR OF PHILOSOPHY

David D. Thomas, advisor

July, 2010

ACKNOWLEDGEMENTS

I want to first and foremost thank my thesis advisor, David D. Thomas, without whom this work would not have been possible. Dave's unwavering support and enthusiasm have always motivated me to work harder, think more critically and always question results without sound proof. He has taught me to be a better scientist, not only by asking good questions and designing proper experiments but by effectively communicating my results with a larger audience.

I would like to thank my committee members; Dr. Carrie Wilmot, Dr. David Bernlohr, Dr. Kylie Walters and Dr. Gianluigi Veglia for their guidance and helpful discussions.

I would also like to thank Dr. Christine Karim who first taught me the necessary techniques of reconstituting spin labeled PLB in a lipid bilayer and acquiring an EPR spectrum. She has continued to provide sound advice on these first steps towards my thesis and has always provided an abundant source of TOAC labeled PLB.

This work would not have been possible without the friendship and helpful advice from Elizabeth Lockamy who started graduate school with me. Elizabeth was always kind enough to lend me purified SERCA and help me with co-reconstitution questions. As time went by, we spent a great deal of time optimizing SERCA purification and even more time working out procedures to quantify PLB phosphorylation. She has always been very helpful and provided critical feedback concerning every aspect of graduate school life from experimental design to manuscript writing to the mounds of paperwork required to finish graduate school. I am eternally grateful to her.

I also wish to thank Zach James for his unending questions, curiosity help and friendship. I have always been impressed by his diligence, hard work but most importantly his willingness to help anyone in the lab who has a question. I am specifically grateful for his help preparing my samples over the last year when I was at home with my kids.

For his helpful advice on EPR theory, spectrometer use and data analysis I am very grateful to Dr. Yuri Nesmelov who was always willing to take time to answer any questions I had and to help me troubleshoot spectrometer issues.

I wish to thank Edmund Howard for many useful discussions on EPR theory and spectral analysis. I also wish to thank him for writing the Contours and WACY EPR analysis software which I have used almost every day of my life over the last six years.

For his helpful discussions on sarcoplasmic reticulum protein structure and function I would like to thank Dr. Mike Autry. His knowledge of the massive body of literature on this subject, generosity of time and the ability to effectively identify and communicate key issues has greatly enhanced my education and experience in the lab.

I wish to thank Dr. Bengt Svensson for always providing me with beautiful models of PLB and the SERCA-PLB complex which have greatly added to talks and fellowship applications over the last several years.

I was fortunate enough to have the expert guidance of Octavian Cornea in matters of fellowship application submission, manuscript submission, navigating the paperwork requirements of a graduate student and all of the other untold tasks he performs behind the scenes in Dave's lab. I am truly thankful for his consistent support and his friendship over the last six years.

For ordering all of the supplies, managing the lab and helping with general scientific questions over the last six years, I am grateful to Sarah Blakely. Dave's large and diverse lab would not function without Sarah's commitment and hard work.

For maintaining the DDTLab network and always helping me troubleshoot any computer or software issues I am grateful to both Roy Collins and Stephen Acrand, our resident computer boys.

I am eternally grateful to my parents, Daniel and Mary Torgersen for their unwavering support throughout this journey. Although they didn't understand exactly what I did, they did understand the commitment necessary to complete this thesis and have always provided support, encouragement and optimism. I cannot thank them enough. I wish to specifically thank my mother for making the trip to River Falls every week to watch my children so I could continue to work on and complete this thesis.

To my mother and father-in-law, Betty and Jerry Fenna, I am thankful for their support, concern and understanding. I am also grateful to Betty for her weekly child care visits that enabled me to finish this thesis.

Finally to my wife, Carrie Torgersen M.D., words cannot describe my gratitude for giving me a little nudge down this path six years ago. It has been a long and sometimes difficult journey, but I would have been lost without your constant love and encouragement. Thank you for your financial support, sacrifice and for giving me two beautiful daughters during this journey.

DEDICATION

For Carrie, Frankie and Emme

ABSTRACT

Muscle contraction and relaxation is regulated by calcium flux between the sarcoplasmic reticulum and the cytoplasm. Subsequent to muscle contraction, calcium must be sequestered to the sarcoplasmic reticulum in order for muscle relaxation to occur. The sarco-endoplasmic reticulum Ca-ATPase (SERCA) is a P-type ATPase embedded in the SR membrane which uses ATP hydrolysis to pump calcium back into the SR lumen to facilitate muscle relaxation. In cardiac muscle, SERCA activity is regulated by phospholamban (PLB) a 52-residue integral membrane protein which exists in a dynamic equilibrium between monomeric and pentameric species. Previous data have shown that monomeric PLB is the primary regulator of SERCA activity but recent publications have proposed that the PLB pentamer may also bind to and inhibit SERCA activity. This inhibition can be relieved by phosphorylation of PLB at Ser16, although the mechanism is not known.

Electron Paramagnetic Resonance (EPR) experiments were designed to test two proposed models of the PLB pentamer, the pinwheel and bellflower. Dynamics data using the TOAC amino acid spin label showed that, like the monomer, the pentamer is in a dynamic equilibrium between ordered (T) and dynamically disordered (R) states, with the T state being predominant. Accessibility of spin labels attached to the cytoplasmic domain to the lipid bilayer showed that, like the monomer, the pentamer cytoplasmic domains strongly interact with the lipid bilayer surface. Finally, pulsed EPR (DEER) experiments measuring long range distances between spin labels attached to the cytoplasmic domain showed a bimodal distance distribution with centers at 3 and 5 nm. All of these data support the pinwheel model.

To investigate SERCA binding and phosphorylation affects on PLB dynamics, a monomeric mutant, AFA-PLB, was spin labeled with TOAC either the 11 position in the cytoplasmic domain or the 36 position in the transmembrane domain. Conventional EPR measurements showed that phosphorylation induced and order-to-disorder conformational change in the cytoplasmic domain and that SERCA preferentially binds the PLB R state. Phosphorylation of SERCA bound PLB resulted in a disorder-to-order conformational change, suggesting that pPLB is still bound to SERCA. Conventional dynamics from 36-TOAC in the transmembrane indicated a stable helix which was unaffected by phosphorylation or SERCA binding. Dipolar EPR measurements revealed that phosphorylation of PLB in the absence of SERCA induces oligomerization and that SERCA destabilizes the pPLB oligomer. Saturation Transfer EPR data which measures the rotational diffusion of PLB in the lipid bilayer supported the conclusion that phosphorylation of PLB in the absence of SERCA induces oligomerization and showed directly that phosphorylated PLB is still bound to active SERCA. These data support the model that phosphorylation dependent relief of SERCA inhibition does not require dissociation of the SERCA-PLB complex, but is rather the result of a structural change in the complex.

TABLE OF CONTENTS

LIST OF FIGURES

LIST OF EQUATIONS

ALPHABETICAL LIST OF ABBREVIATIONS

5-PCSL, 1-palmitoyl-2-stearoyl-(5-doxyl)-*sn*-glycero-3-phosphocholine
ATP, adenosine triphosphate
Ca, divalent calcium ion (Ca^{2+})
CaMKII, calcium/calmodulin-dependent protein kinase II
CVD, cardiovascular disease
CW, continuous wave
DEER, double electron electron resonance
DHPC, 1,2-dihexanoyl-sn-3-glycero-phosphocholine
DMPC, 1,2-dimyristoyl-sn-3-glycero-phosphocholine
DOGS-NTA-Ni, 1,2-dioleoyl-sn-glycero-3-{[N-(5-amino-1-carboxypentyl)iminodiacetic acid]succinyl}nickel salt
DOPC, 1,2-dioleoyl-sn-3-glycero-phosphocholine
DOPE, 1,2-dioleoyl-sn-3-glycero-phosphoethanolamine
DPC, dodecylphosphocholine
EPR, electron paramagnetic resonance
MOMD, microscopic order, macroscopic disorder
MTSSL, methanethiosulfonate spin label
Ni^{2+}, divalent nickel ion
NiAA, Ni(II) acetylacetonate
NIEDDA, Ni(II) ethylenediamine diacetic acid
NKA, Na^{+}, K^{+}-ATPase
NMR, nuclear magnetic resonance
PADS, peroxylamine disulfonate
PLB, phospholamban
PLM, phospholemman
PMCA, plasma membrane calcium ATPase
PKA, cAMP dependent protein kinase A
PRE, paramagnetic relaxation enhancer
SDS-PAGE, sodium dodecyl sulfate polyacrylamide gel electrophoresis
SERCA, sarco-endoplasmic reticulum calcium ATPase
SR, sarcoplasmic reticulum
STEPR, saturation transfer electron paramagnetic resonance
TM, transmembrane
TOAC, 2,2,6,6-tetramethylpiperidine-1-oxyl-4-amino-4-carboxylic acid

CHAPTER 1. Introduction

1.1 The Sarcoplasmic Reticulum

Precise regulation of calcium flux in muscle cells is necessary for proper function. High [Ca^{2+}] (micromolar) in the cytoplasm induces contraction, but in order for relaxation to occur, calcium is removed from the cytoplasm, reducing [Ca^{2+}] to nanomolar levels. The sarcoplasmic reticulum (SR) is a specialized organelle found in muscle cells which functions as a calcium repository. After depolarization of the muscle cells, calcium is released from the sarcoplasmic reticulum (SR) by the ryanodine receptors, large membrane protein channels embedded in the SR. Because calcium is flowing down its concentration gradient, no energy is required to move calcium from the SR lumen to the cytoplasm. Calcium binds to the force generating proteins and the muscle contracts. The sarco-endoplasmic reticulum calcium-ATPase (SERCA) is a P-type ATPase also located in the SR membrane which functions to move calcium back into the SR to

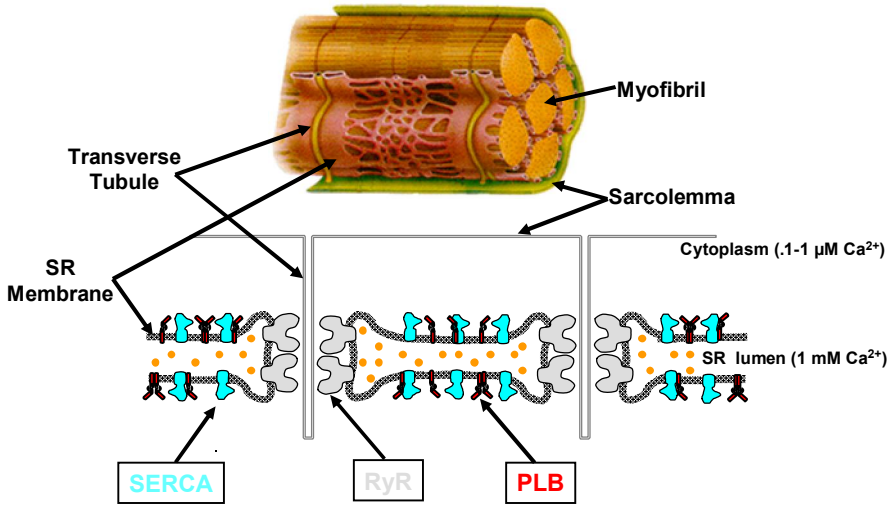

Figure 1. The sarcoplasmic reticulum.
The sarcoplasmic reticulum functions as a calcium storage organelle in muscle cells. The principal calcium regulatory proteins, SERCA (blue), ryanodine receptor (grey) and PLB (red) in cardiac muscle cells are highlighted.

facilitate muscular relaxation (Figure 1). In this case, calcium is pumped against its concentration gradient, requiring energy input. SERCA hydrolyzes 1 molecule of ATP for every two calcium ions pumped back into the SR [1-3]. SERCA activity must be regulated to accomplish time-dependent calcium flux.

In cardiac muscle, SERCA activity is regulated by phospholamban (PLB), a 52-residue integral membrane protein also located in the SR membrane [5]. PLB exists in an equilibrium between monomeric and pentameric species but it has been shown that the monomer is the primary regulator of SERCA activity and the pentamer is thought to be a storage form of PLB [6-8]. Monomeric PLB binds to and inhibits SERCA activity by decreasing SERCA's apparent affinity for calcium. This inhibition can be overcome by micromolar [Ca^{2+}] or by phosphorylation of PLB at Ser16 and/or Thr17 by PKA or CamKII, respectively (Figure 2). The significance of dual site phosphorylation is still controversial but studies indicate that Ser16 phosphorylation is the major effector of phosphorylation-dependent relief of inhibition [9, 10]. While there is agreement that high [Ca^{2+}] or PLB phosphorylation does reverse SERCA inhibition, there are two main models proposing different

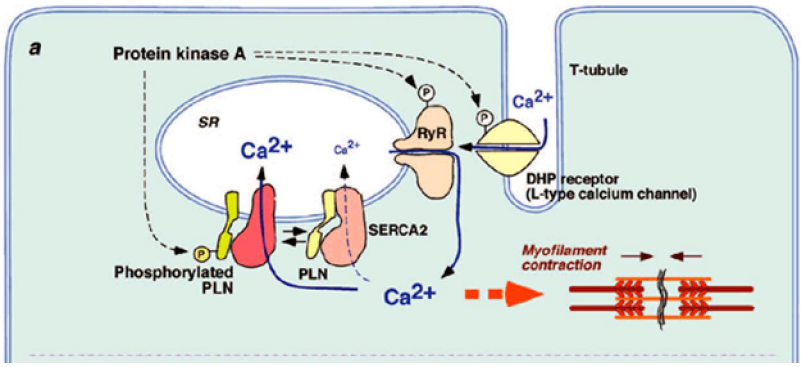

Figure 2. PLB phosphorylation relieves SERCA inhibition.
Phosphorylation of PLB at Ser16 by PKA relieves SERCA inhibition leading to translocation of calcium into the SR which facilitates muscle relaxation. Reproduced from [4].

mechanisms of inhibition relief. One model, proposes that PLB phosphorylation or high [Ca^{2+}] dissociate the SERCA-PLB complex, thereby relieving inhibition [7, 11-14]. The other model proposes that high [Ca^{2+}] induces a structural change in SERCA and that Ser16 phosphorylation induces a structural change within PLB but neither structural change dissociates the SERCA-PLB complex [15-19].

1.2 SERCA Function and Structure

SERCA is a member of the P-type ATPase family whose constituents undergo an autophosphorylation step during their catalytic cycle. In addition to SERCA, the sodium-potassium ATPase (NKA) and plasma membrane calcium ATPase (PMCA) are members of this large family. NKA has recently been crystallized and shows remarkable structural similarity to SERCA [20]. In addition to structural themes, there are similarities in the regulation of SERCA, NKA and PMCA function. SERCA activity is regulated by PLB while NKA activity is regulated by a member of the FXYD family of proteins, phospholemman (PLM) which has been shown to be structurally and functionally similar to PLB [21-25]. The PMCA has a long C-terminal tail which has been hypothesized to regulate the pump's activity [26]. Clearly, there are common structural and regulatory themes within the P-type ATPase family.

SERCA is a ubiquitous protein expressed in higher order eukaryotes. It is a product of three different genes, each with different splice variants. The SERCA1 (ATP2A1) gene is expressed in fast-twitch skeletal muscle and has two different isoforms, SERCA1a and SERCA1b. SERCA1a is expressed in adult tissue while SERCA1b is expressed in fetal tissue. The SERCA2 (ATP2A2) gene is expressed in slow-twitch skeletal and cardiac muscle and contains three isoforms, SERCA2a,

SERCA2b and SERCA2c while SERCA3 (ATP2A3) has six isoforms (a-f), is expressed in non-muscle cells and appears to be a minor component in some muscle tissues . The primary structure is highly conserved across all there genes with 84% identity between SERCA1a and SERCA2a and 74% identity between these isoforms and SERCA3a [27].

The SERCA catalytic cycle has been well studied and characterized over the last several decades [1, 28-33]. SERCA exists in two major biochemical states, a low calcium affinity (E2) state and a high calcium affinity (E1) state. Binding of two calcium ions from the cytoplasm to the calcium binding sites in the transmembrane domain induces a conformational shift from E2 to E1. This structural rearrangement opens the nucleotide binding site in the N domain, allowing Mg-ATP to bind. Following ATP hydrolysis, the γ-phosphate is transferred to Asp351 in the P domain, the autophosphorylation residue conserved in the P-type ATPase family. ADP is released, forming a high energy phosphoenzyme intermediate with low calcium affinity leading to the release of the two calcium ions into the SR lumen. Finally, inorganic phosphate is released, completing the catalytic cycle and returning SERCA to the E2 state to begin the next round of calcium transport (Figure 3).

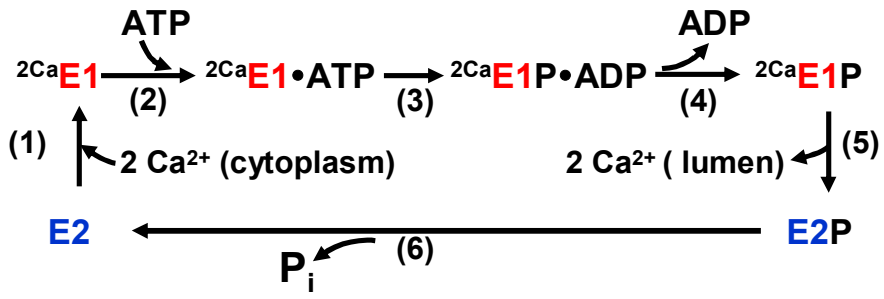

Figure 3. SERCA catalytic cycle.

The catalytic cycle of SERCA. High Ca^{2+} affinity (E1) states are shown in red while low Ca^{2+} affinity (E2) states are shown in blue.

SERCA is a rather large protein made up of ~ 1,000 residues with a molecular weight of 110 kDa. Studies including cryo electron microscopy and X-ray crystallography have provided a wealth of structural information [28, 35-44]. SERCA can be divided into four distinct domains; the nucleotide binding (N), phosphorylation (P), actuator (A) and transmembrane (TM) domains. While the N, P and A domains are located in the cytoplasm, the TM domain is composed of ten α-helices which act to anchor the protein in the SR membrane and also contain the calcium binding sites (Figure 4). The N domain contains the nucleotide (ATP) binding site. Subsequent to ATP hydrolysis, the γ-phosphate is transferred to Asp351 in the P domain. The A domain acts as the calcium gate, moving the TM helices to open and close the calcium channel. The TM domain also contains a groove between TM helices two, four, six and nine which is believed to be the binding site for PLB.

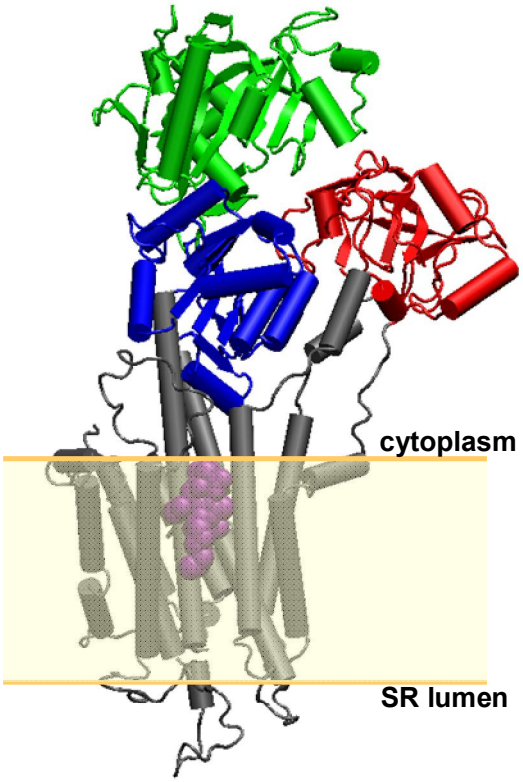

Figure 4. SERCA structure.

The E2 (1IWO) crystal structure of SERCA showing the nucleotide binding (green), phosphorylation (blue) actuator (red) and transmembrane (grey) domains. Thapsigargin, which is necessary to crystallize the E2 form is shown in purple [34]. Structural representation made using PyMol.

Since the first high resolution structure of SERCA published in 2000, there have been 24 high resolution structures published representing all of the biochemical states in the catalytic cycle. Interestingly, there are no large scale domain movements between the

different biochemical states, except the high calcium affinity (E1) state. Here, SERCA is in an open position with a 6.6 nm distance between the centers of the A and N domains [45]. All other structures published so far show about a 4 nm distance. In 2008, *in-vivo* fluorescence resonance energy transfer (FRET) showed that the A to N interdomain distance is significantly shorter than the crystal state indicating that the E1 high calcium affinity state is more compact, similar to the other crystal structures published [46]. Although a significant amount of research has been focused on the SERCA catalytic cycle and obtaining high resolution crystal structures of all the biochemical states, I have been focusing on the E2 low calcium affinity structure since it has been proposed that PLB binds to the E2 state of SERCA, thereby preventing the E2-to-E1 structural change and inhibiting catalytic activity.

1.3 PLB

A study of SERCA structure and function would not be complete without an understanding of the structural and functional dynamics of PLB. PLB exists in an equilibrium between monomeric and pentameric species but it has been shown that the monomer is the primary regulator of SERCA activity and the pentamer is thought to be a storage form of PLB [6-8]. Consequently, a considerable amount of work has been done to determine the structures of both monomeric and pentameric PLB. To this end, a fully functional monomeric mutant (AFA-PLB) has been made by replacing the three native Cys residues in the transmembrane domain with Ala, Phe and Ala, respectively [48, 49]. An NMR structure of AFA-PLB in DPC micelles shows the hydrophobic C-terminus is buried in the micellar core while the amphipathic N-terminus lies outside the micellar core and interacts with the phosphocholine headgroups. This average NRM structure shows PLB adopting an "L-shape" with three distinct structural domains; domain Ia (residues 2-16), domain Ib (residues 17-21) and domain II (residues 22-52). Domains Ia and II are α-helices connected by a flexible loop, domain Ib (Figure 5). Additional NMR

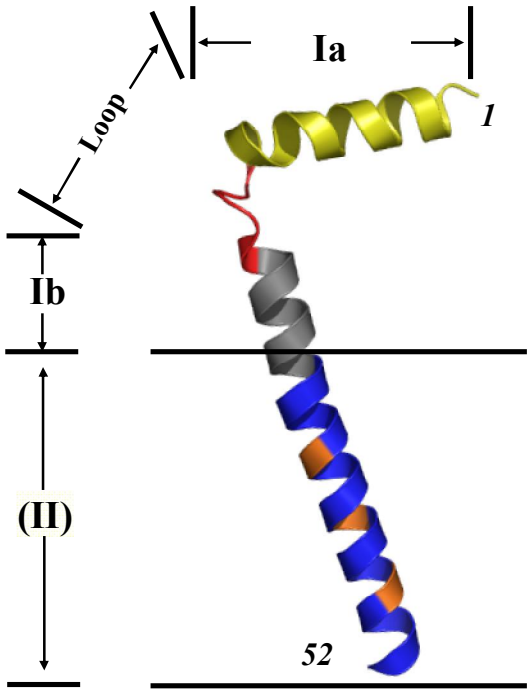

Figure 5. AFA-PLB structure in DPC micelles.

The NMR determined structure of AFA-PLB in DPC micelles (1N7L). Domain Ia is in yellow, the loop is in red, domain Ib is in grey and domain II is in blue. The three Cys residues which are mutated to Ala, Phe and Ala, respectively are colored in orange [47]. Structural representation made using PyMol.

data further divides PLB into four domains, based on backbone dynamics. Domains Ia (residues 1-16), the loop (residues 17-22) and Ib (residues 23-30) all have dynamics on the μs-to-ms timescale but domain II (residues 31-52) dynamics are considerably more restricted [50].

These dynamics measurements and sub-division of PLB into four different domains agree with EPR data on the same monomeric mutant reconstituted into lipid bilayers [51]. EPR spectra from PLB labeled with the amino acid spin label, TOAC, which reports directly the peptide backbone dynamics, show that unlike domain II which consists of a single, highly ordered state, the N-terminus, domains Ia and Ib exist in equilibria between an ordered T state and a dynamically disordered R state. Quantitative spectral analysis reveals that the mol fractions and dynamics of the T and R states vary between the different domains (Figure 6).

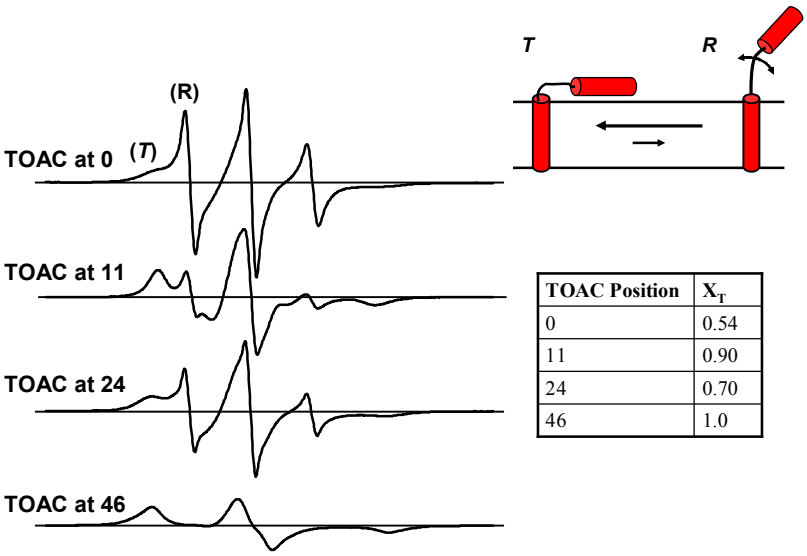

TOAC Position	X_T
0	0.54
11	0.90
24	0.70
46	1.0

Figure 6. TOAC detected dynamics of AFA-PLB

EPR spectra of AFA-PLB labeled with TOAC at positions 0, 11, 24 and 46 with the corresponding T-state mol fractions [51]. The cartoon illustrates the T-state and R-state structures.

To date, the most accurate structure and topology of PLB in lipid bilayers (its native environment) has been generated with molecular modeling using restraints from a multi-dimensional NMR approach incorporating both solution and solid-state NMR data

(Figure 7). It should be noted that while this and other structures published so far show the T state which is the major component, a high resolution structure of the R state has eluded researchers so far, most likely because it is a disordered state with large amplitude nanosecond dynamics.

In addition to the structural data and corresponding models of monomeric PLB, there is a significant amount of functional data which provide insight into how PLB alters SERCA function. Functional studies of SERCA co-reconstituted with a truncated derivative of PLB consisting of only the TM domain (residues 26-52) shows normal inhibition compared to WT-PLB [49]. In addition, similar studies showed that the cytoplasmic domain of PLB (residues 2-25) alone or tethered to a lipid anchor does not affect SERCA function [53, 54]. Despite the lack of inhibitory function of the cytoplasmic domain, EPR data shows a topological change upon SERCA addition. Specifically, PLB binding to SERCA reduces the mobility of the cytoplasmic domain at position 11 and decreases the interaction of the cytoplasmic domain with the bilayer surface [55].

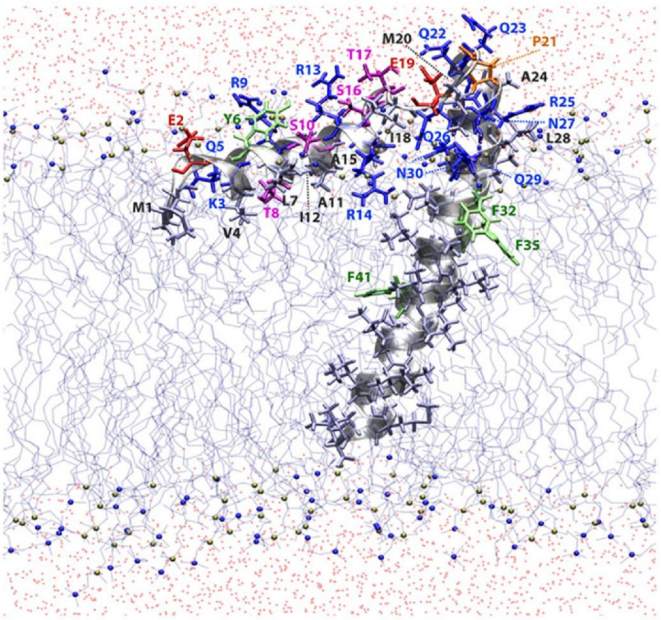

Figure 7. Structure of monomeric PLB in a lipid bilayer.

The high resolution structure of monomeric PLB in a lipid bilayer shows both secondary structure and topology. The cytoplasmic domain is partially buried in the lipid and makes a 102 ° angle with respect to the bilayer normal. The TM domain is a continuous helix and is tilted 24 degrees with respect to the membrane normal. Figure adapted from [52].

NMR and molecular dynamics simulations have also been used to study the effects of Ser16 phosphorylation on monomeric PLB structural dynamics [56-59]. Results from simulations and spectroscopic experiments both show that PLB phosphorylation at Ser16 increase the dynamics of the cytoplasmic domain by partially unfolding the peptide backbone without significantly affecting the dynamics of the TM domain. In addition to affecting the dynamics of the cytoplasmic domain, data also show that phosphorylation induces PLB oligomerization [8, 60]

Although cryo-EM data and docking simulations suggest that the PLB pentamer may bind to SERCA [63, 66], the general consensus of opinion at this point is that the pentamer functions merely as a storage form. Mutagenesis studies have revealed that the pentamer is stabilized by a Lue-Ile zipper and mutations in the TM domain of PLB which interfere with the helix-helix packing destabilize the pentamer [48, 67, 68]. Four

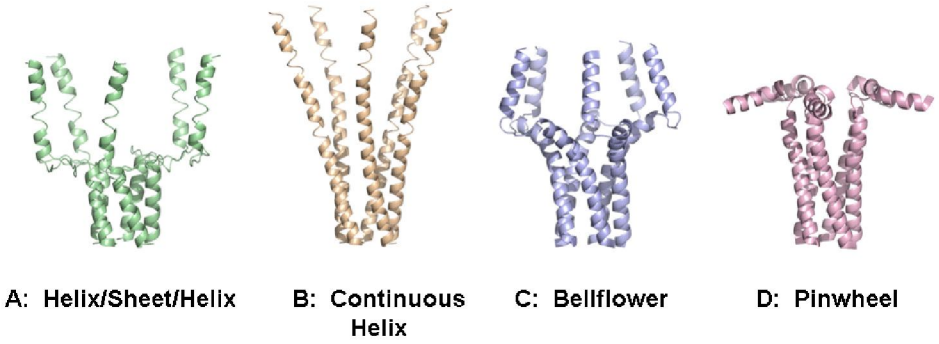

Figure 8. Proposed PLB pentamer structures.

(A) Extended helix/sheet/helix [61]. (B) Continuous helix [62]. (C) Bellflower [PDB:ID 1ZLL [63] (D) Pinwheel [PDB:ID 1XNU [64]. Structural representations made using PyMol. Figure adapted from [65].

different structures of the PLB pentamer have been proposed (Figure 8). While the structure and topology of the transmembrane helices are similar in all four models,

significant differences can easily be seen in the cytoplasmic helices. The helix/sheet/helix, continuous helix and bellflower models show that both the TM and cytoplasmic helices are parallel or nearly parallel with the bilayer normal. The pinwheel model is the only structure predicting that the cytoplasmic helices are nearly perpendicular to the membrane normal and interacting with the bilayer surface, similar to the PLB monomeric structure (Figure 5). All other models suggest minimal to no interaction of the cytoplasmic helices with the bilayer surface. Data from other labs suggest that, like the monomer, the pentamer cytoplasmic helices do interact with the lipid bilayer surface, evidence against the helix/sheet/helix, continuous helix and bellflower models [69-72]. Additionally, in the helix/sheet/helix model, the phosphorylation sites Ser16 and Thr17 are oriented towards the bilayer surface, making it difficult to imagine how PKA or CamKII could bind to and phosphorylate PLB. Although the pentamer is thought to be a storage form for PLB and not directly involved in SERCA regulation, therapeutic strategies for cardiovascular disease may involve stabilization of the pentamer, thereby shifting the monomer-pentamer equilibrium and activating SERCA. Consequently, one my thesis projects was to use EPR spectroscopy in collaboration with NMR spectroscopic experiments to determine the pentamer structure in lipid bilayers as well as DPC micelles.

1.4 The SERCA-PLB Complex

Although several high resolution structures for SERCA and PLB have been published, no high resolution structure for the SERCA-PLB complex exists.

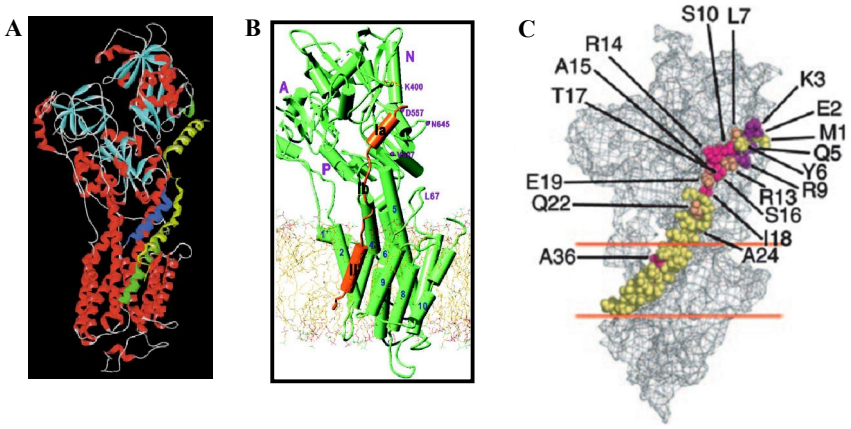

Figure 9. Models of the SERCA-PLB Complex.

(A) Model of monomeric PLB docked to E_2 SERCA crystal structure [73] showing PLB in yellow. (B) Model of monomeric PLB docked into E_2 SERCA crystal structure showing SERCA in yellow and PLB in green [74]. (C) SERCA-PLB model shown in (B) color coded to show PLB residues affected by SERCA binding based on NMR experiments [75].

Several structural models have been proposed based on mutagenesis, cross-linking and spectroscopic experiments. Cross-linking experiments have established close proximity of Leu321Cys in SERCA to Asn27Cys in PLB, Val89Cys in SERCA to Val49Cys in PLB and Lys397/Lys400 in SERCA to Lys3 in PLB. Figure 9A and Figure 9B both show structural models generated by docking structures of monomeric PLB in organic solvent onto calcium free (E_2) structures of SERCA. In both cases, distance restraints obtained from cross-linking and mutagenesis were used during the docking. Both models show the TM domain of PLB lying in a groove formed by SERCA TM helices two, four six and nine. Figure 9C is the same SERCA-PLB complex model shown in Figure 9B but is color coded (based on NMR experiments) to represent residues affected by SERCA binding. In all three models, the TM and 1a domains are predicted to remain helical

when bound to SERCA, but the loop region and residues in domain 1b are predicted to lose their helical structure in order for PLB to adopt the extended conformation and interact with residues Lys397-Ile402 on SERCA. These models support previously published data indicating that SERCA reduces the interaction of the PLB cytoplasmic domain with the lipid bilayer surface by binding the an extended form of PLB [55].

1.5 SERCA and PLB Implications in Cardiovascular Disease

According to World Health Organization data, cardiovascular disease is now the leading cause of mortality, globally. In 2004 29% (17.1 million) of all deaths were attributed to cardiovascular disease and that number is expected to rise to 23.6 million by the year 2030. Recent data has shown that both SERCA and PLB are implicated, either directly or indirectly in cardiovascular disease.

To date, there have been no SERCA mutations directly associated with cardiovascular disease. The only identified SERCA mutations cause Brody's disease, a skeletal muscle disorder or Darier's disease, a skin disorder. Brody's disease is the result of mutations in the SERCA1a isoform. One mutation has been identified at the splice site of intron three while two others have been identified, each of which lead to premature stop codons resulting in truncated protein expression [76]. While patients afflicted with Brody's disease suffer from exercise induced muscle cramping, stiffness and impaired muscular relaxation, their lifespan is unaffected, possibly because of SERCA2a upregulation [27]. Darier's disease is the result of an autosomal dominant missense mutation in the SERCA2 gene, affecting both SERCA2a and SERCA2b isoforms. Patients with Darier's disease suffer from loss of adhesion between epidermal cells and

abnormal keratinization [77]. Interestingly, patients diagnosed with Darier's disease do not suffer from any abnormal cardiovascular function even though the SERCA2 gene is mutated.

Despite the lack of SERCA mutations directly involved with CVD, SERCA protein levels have been implicated in cardiovascular disease. Tissue extracts from animal models and human hearts diagnosed with heart failure showed low SERCA protein levels and/or low SERCA activity [78-80]. Whether heart failure is a cause or an effect of low SERCA levels/activity has yet to be determined.

Although there have been no SERCA mutations which have been directly linked to cardiovascular disease, there are currently six identified human PLB mutations implicated in cardiovascular disease. There are three mutations in the coding sequence of the PLB gene and three are mutations in the upstream promoter region of the PLB gene.

Two mutations in the coding region of PLB have been classified as gain-of-function due to the fact that they result in chronic SERCA inhibition. The third mutation in the coding region of PLB is classified as a loss-of-function mutation due to the lack of PLB inhibition on SERCA activity. Interestingly, all three mutations lead to cardiovascular disease and in some cases premature death.

The R9C mutation was first reported in 2003 [81]. Genetic and pedigree analysis of a large American family suffering from dilated cardiomyopathy and heart failure showed an autosomal dominant inheritance of a PLB mutant where arginine at position nine is mutated to a cysteine residue. Characteristics of affected individuals included increased heart chamber diameter and decreased contractile function at an early age. A transgenic mouse model heterozygous for the R9C mutation showed similar anatomical

and physiological defects. Quantitation of PLB phosphorylation levels and immunoprecipitation experiments on excised human tissue, transgenic mouse tissue and HEK-293 cells heterozygous for the R9C mutation showed clearly that the R9C mutation traps PKA resulting in decreased levels of PLB phosphorylation, chronic SERCA inhibition and the development of CVD.

The other gain-of-function mutation, R14del, was first reported in 2006 [82]. Here, a mutation in the coding region of the PLB gene results in the deletion of the arginine residue at position 14. Like the R9C mutation, the R14Del mutation has been shown to be autosomal dominant. Human individuals heterozygous for this mutation exhibit dilated cardiomyopathy and contractile dysfunction by middle age and in some cases premature death due to heart failure. A transgenic mouse model heterozygous for the mutation recapitulated the human phenotype. Activity assays of HEK-293 cells coexpressing WT and R14Del PLB showed a synergistic effect of the mutant on WT PLB resulting in superinhibition of SERCA activity which could be not be reversed upon phosphorylation.

Unlike the R9C and R14Del gain-of-function mutations, L39Stop is a loss-of-function mutation. Here a premature stop codon at L39 results in a truncated PLB mutant lacking the majority of the TM domain. Humans heterozygous for the mutation develop cardiac hypertrophy, but contractile function is not diminished. In contrast, humans homozygous for the mutation develop dilated cardiomyopathy and heart failure. Functional assays measuring calcium transport by SERCA were performed in HEK-293 cells transfected with wild type, mutant PLB (L39Stop) or a combination of both. Results showed that L39Stop PLB was unable to inhibit SERCA, but when L39Stop was

combined with wild type PLB, SERCA activity was inhibited to the same extent as wild type only levels.

Western blots performed on HEK-293 cells infected with mutant phospholamban detected no peptide in the endoplasmic reticulum (both monomeric and pentameric wild type PLB were found here). However, low levels of mutant PLB were found in the insoluble fraction of the cell digests, proving that mutation does not prevent transcription and translation, but may reduce these activities. Phospholamban immunoblots of excised left ventricle myocytes from four different subjects further confirmed the absence of the L39Stop mutant [83]. Interestingly, PLB ablation in mouse models enhances cardiac contractility while the naturally occurring null PLB mutation decreases cardiac contractility leading to heart failure in humans.

In addition to the three mutations in the coding region of the PLB gene, three additional mutations have been found in the upstream promoter region of patients with CVD [84-86]. Two of these mutations lead to increased PLB expression/enhanced promoter activity while the third mutation results in decreased PLB promoter activity in a model system. CVD resulting from increased PLB expression supports data from a transgenic mouse study which showed a direct correlation between decreased SERCA activity and decreased cardiac contractility due to increased PLB/SERCA protein ratios. This seems to contradict the finding that decreased PLB promoter activity causes CVD but data also shows that a null PLB phenotype in humans also results in CVD.

Clearly, the regulation of SERCA activity by phospholamban is important for - normal calcium cycling and cardiovascular health. Although a great deal is already known about the structure and function of both proteins and their interaction, information

from studies on the natural human PLB mutations indicate that more research is needed for a complete understanding of this process. As cardiovascular disease rates increase a need for cures besides heart transplant surgery will concurrently rise.

CHAPTER 2. Electron Paramagnetic Resonance Spectroscopy

2.1 EPR Introduction

Electron Paramagnetic Resonance (EPR), like any other spectroscopy, is the study of light interacting with matter. When a molecule absorbs a photon, there is a resulting transition in energy levels from the ground state to an excited state of higher energy. Planck's law (Equation 1) states that absorption will only occur if the energy of the photon matches the difference in energy levels (ΔE):

$$\Delta E = h\nu \qquad \textbf{Equation 1}$$

where ν is the photon's frequency and h is Planck's constant. In magnetic resonance, the absorption of a photon causes a spin flip.

All electrons possess angular momentum which gives them spin (S). The magnetic moment (μ) is a product of the electron spin (S) and the gyromagnetic ratio (γ). Spin itself cannot be measured but its component along a given axis can. Consider a system where a static magnetic field

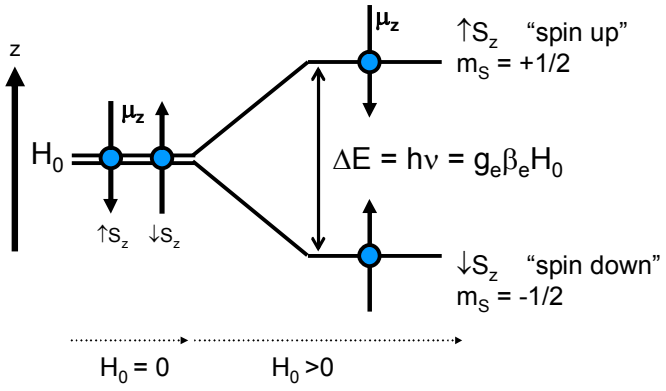

Figure 10. The electron Zeeman interaction

The magnetic dipole moment along the z-axis (μ_z) in a static magnetic field (H_0) applied in the z-axis. If the magnetic field strength is zero, there will be no energy difference in the two possible orientations of μ_z. As the magnetic field strength increases, the energy gap between the aligned "spin down" and counter aligned "spin up" magnetic moments increases linearly with the field strength.

(H_0) is applied in the z-axis (Figure 10). The magnetic dipole (μ) can adopt two possible orientations with respect to H_0, aligned or counter aligned. If the strength of the static field is zero, then there will be no energy difference between the two orientations but in non-zero field, the energy (E) of the interaction between the static field (H_0) and the magnetic moment (μ) in the z-axis can then be defined as the vector product of the static field and electron spin:

$$E = -\gamma S_z \bullet H_0 \qquad \textbf{Equation 2}$$

Since spin is quantized, S_z can only have vales of $m_s\hbar$ where the spin magnetic quantum number, $m_s = \pm$ ½ and $\hbar$ is the reduced Planck's constant $h/2\pi$. The gyromagnetic ratio (γ) can be expressed as $-g\beta/\hbar$ where g is the electron g value, β is the Bohr magneton and $\hbar$ is the reduced Planck's constant. Equation 2 can now be rewritten:

$$E = g\beta H \qquad \textbf{Equation 3}$$

Selection rules dictate that $\Delta m_s = 1$ leading to the fundamental EPR equation:

$$\Delta E = h\nu = g\beta H \qquad \textbf{Equation 4}$$

which describes the electron Zeeman interaction (Figure 10).

In EPR spectroscopy,.absorption is detected by keeping the static magnetic field (H_0) constant and adjusting the microwave frequency (ν) to find the resonance field positions, H_{res}:

$$H_{res} = \frac{h\nu}{g\beta}$$ **Equation 5**

Unlike optical spectroscopy, it is not the electric component of the microwave radiation which induces absorption, but the magnetic component (H_1) applied perpendicular to the static magnetic field (H_0) which induces the spin flips. Typically EPR spectra are not recorded as absorption spectra, but the first harmonic by applying a small modulation amplitude to the static magnetic field. This allows for phase sensitive detection which increases the signal/noise ratio.

The most common method to measure protein structure and dynamics using EPR is to attach a nitroxide spin label to the protein (see chapter 2.2). The nitroxide spin label contains the unpaired electron which gives rise to the EPR signal. This unpaired electron is coupled to a ^{14}N nucleus which has an intrinsic nuclear spin and associated magnetic moment. Just like the electron spin, the nuclear spin has allowed orientations in a magnetic field. The ^{14}N nucleus has three allowed orientations in a magnetic field, m_I = -1, 0 and 1. The

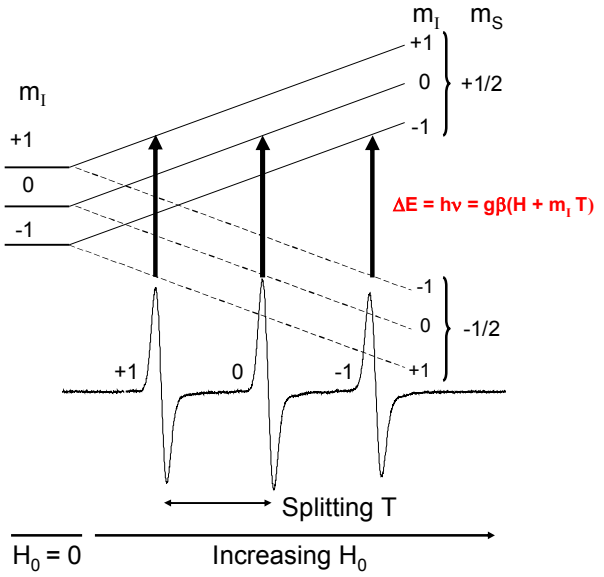

Figure 11. Nuclear hyperfine interaction

Derivative EPR spectra illustrating the nuclear hyperfine effect. The nuclear spin state (m_I) splits each electron spin state (m_s) into three different energy levels. Quantum mechanical selection rules forbid nuclear spin transitions coupled to electron spin transitions. Consequently, the unpaired electron absorption line is split into three equally spaced derivative lines with splitting T, as a function of the nuclear spin state.

nuclear magnetic moment affects the strength of the static magnetic field felt by the unpaired electron and splits the single resonance position into three resonance positions, dependent on the nuclear spin state (m_I). The splitting (T) is anisotropic and dependent on θ, the angle between the static magnetic field and the nitroxide principal axis (see chapter 2.3).

2.2 The TOAC Spin Label

The EPR signal can arise from an unpaired electron in a transition metal or the unpaired electron in a nitroxide spin label. Traditionally, the study of protein structure and dynamics has been accomplished using site-directed spin labeling (SDSL), a technique pioneered by Dr. Wayne Hubbell. Here, site-directed mutagenesis is used to introduce a specific amino acid residue (usually Cys) at a selected site in the protein. Most commercial spin labels are produced with a sulfhydral reactive group such as an iodoacetamide or methanethiolsulfonate which reacts with the Cys residue side chain. The mutated protein is reacted with a nitroxide spin label to produce an EPR active protein. Spin labels are much smaller (about the size of Trp residue) and less hydrophobic than fluorescent probes which is a significant advantage.

Although SDSL is a powerful tool and has been used extensively over the last two decades, it may not provide accurate, quantitative data concerning the peptide backbone dynamics. In most spin labels, there are several single bonds between the unpaired electron and the peptide backbone. Consequently, slower peptide backbone dynamics may be obscured by nanosecond or sub-nanosecond spin label dynamics. TOAC is a unique spin label in that it is really an amino acid. The α-carbon is a part of the six member nitroxide ring. This direct fusion of the nitroxide to the peptide backbone yields increased spectral resolution when compared to spin labels attached to Cys side chains (Figure 12). In addition to increased sensitivity to backbone dynamics, interspin distance measurements are more precise.

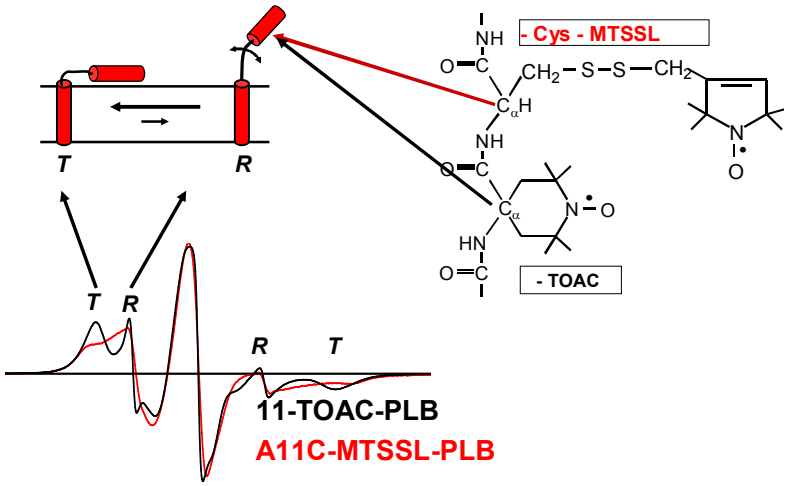

Figure 12. TOAC enhanced resolution of peptide backbone dynamics.

Spectra of PLB labeled at position 11 in the cytoplasmic domain with either TOAC (black) or MTSSL (red). Although both spins labels report the T and R states, spectral resolution is increased with the use of TOAC. The cartoon is representative of structural and dynamics data and the peptide backbone is drawn to illustrate how TOAC and MTSSL are coupled.

2.3 Orientation and Conventional Dynamics

The EPR spectrum is dependent on the anisotropy of the spin label. That is to say that the resonance field positions are determined by the angles the spin label makes with respect to the applied magnetic field, . The center of the EPR spectrum is determined by the g-anisotropy while the splitting is dependent on the nuclear hyperfine anisotropy. When the nitroxide principal axis as aligned with H_0 (θ = 0°), the splitting is maximal compared to the cases where the x or y axes are aligned with H_0 (θ = 90°) and the splitting is minimal (Figure 13). In a randomly oriented sample, all values of θ and ϕ are present and the spectrum is the sine-weighted sum of the resonance positions. Rotational motion on the time-scale comparable to the nitroxide T_2 (~ 10 ns) averages the spectral anisotropy, producing more complex lineshapes.

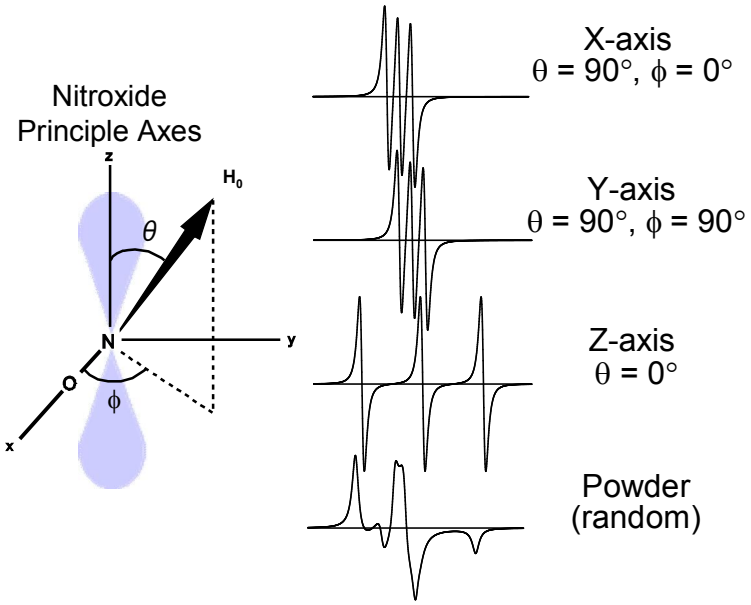

Figure 13. Spin label anisotropy.
The nitroxide spin label axes and corresponding anisotropic EPR spectra.

Rotational motion can be modeled as either isotropic rotational diffusion or anisotropic rotational diffusion. Isotropic rotational diffusion assumes the spin label undergoes unrestricted rotational motion. In this case, the EPR spectra are dependent on the correlation time (τ_R) of the spin label. The anisotropic rotational diffusion model assumes the spin label undergoes restricted rotational motion with sub-nanosecond correlation time. Here the spectra are dependent on the amplitude of motion. This amplitude of motion, defined as the order parameter (S) is the observed anisotropy compared to the maximum anisotropy. The order parameter can be calculated with the following equation:

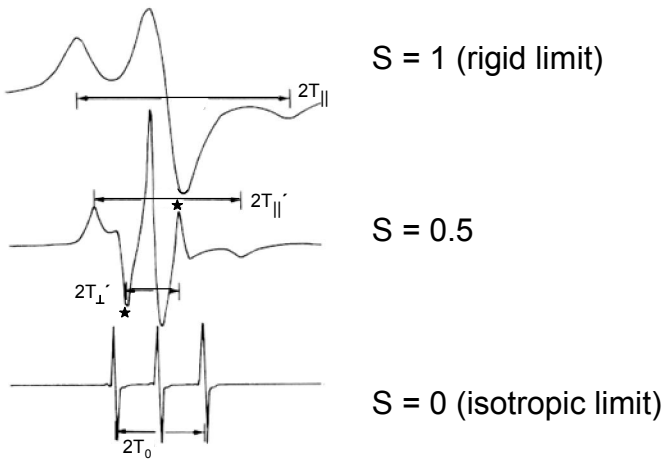

Figure 14. Anisotropic EPR spectra.

EPR spectra undergoing rapid restricted rotational motion. Examples shown correspond to the rigid limit (top), intermediate motion (middle) and unrestricted motion (bottom). The order parameter (S) and its derivation are discussed in the text. Figure adapted from [87].

$$S = \frac{T_{\parallel}' - T_{\perp}'}{T_{\parallel} - T_{\perp}} \approx \frac{T_{\parallel}' - T_0}{T_{\parallel} - T_0} \qquad \textbf{Equation 6}$$

where T_{II}' and $T_{\perp}'$ are the observed parallel and perpendicular splittings and T_{II} and $T_{\perp}$ are the maximal parallel and perpendicular splittings obtained from a frozen sample with no rotational motion. In some cases, it is difficult to measure $T_{\perp}'$ so the order parameter is often calculated using T_0, the isotropic hyperfine splitting constant. Order parameter

values range from 0, isotropic motion at the rapid limit where all of the anisotropy has been averaged resulting in a very narrow spectrum to 1, anisotropic motion at the rigid limit where none of the anisotropy has been averaged out resulting in a wide spectrum (Figure 14). The anisotropic rotational diffusion model can be conceptualized as a wobble in a cone where the amplitude of motion, represented by the order parameter, is defined as the half-cone angle (θ_c) using the following function:

$$S = \tfrac{1}{2}(\cos\theta_c + \cos^2\theta_c) \qquad \textbf{Equation 7}$$

Isotropic rotational diffusion assumes that the spin label undergoes unrestricted motion ($S = 0$) and that the spectra are dependent on the rate of motion (τ_R). Slow motion at the rigid limit results in a powder pattern because none of the anisotropy has been averaged. As motion increases (shorter correlation times) the anisotropy begins to be averaged resulting in narrowing of the lineshapes and the splittings until a narrow spectrum consisting of three

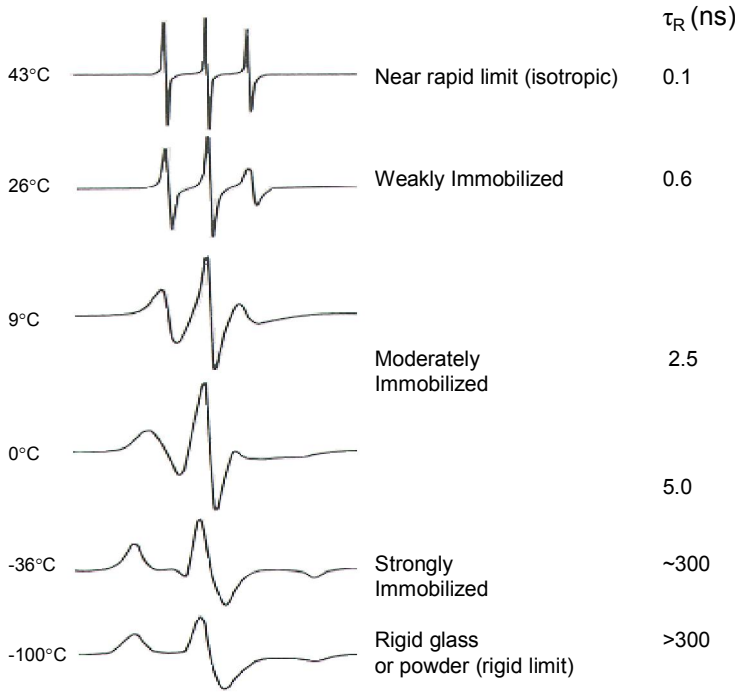

Figure 15. Isotropic EPR spectra

EPR spectra of a spin label undergoing isotropic motion in a glycerol solution as a function of temperature. The calculated correlation times (in ns) are shown to the right of the figure and the temperatures of the samples are shown at the left. Figure adapted from [87].

equally spaced sharp lines representing the rapid limit is observed (Figure 15). If the spectrum is representative of slow or strongly immobilized motion, that is, motion near the rigid limit, the correlation time can be estimated from either the splitting (T_{II}') or the outer half-width at half-height of the low field line (Δ_L) using the following functions and constants from simulations:

$$\tau_R = a[1-(T_{||}'/T_{||})]^b \qquad \textbf{Equation 8}$$

$$\tau_R = x[(\Delta L'/\Delta L)-1]^y \qquad \textbf{Equation 9}$$

where a = 5.4 x 10^{-10} s, b = -1.36, x = 1.15 x 10^{-8} s and y = -0.944. However, if the spectrum is representative of fast or weakly immobilized motion, the correlation time can be estimated based on the rapid limit spectrum using the following function and constant from simulations:

$$\tau_R = z \bullet \Delta H_0' [(h_0/h_{-1})^{1/2}-1] \qquad \textbf{Equation 10}$$

where z = 6.5 x 10^{-10} s/G (Figure 16).

In reality, the motion of a spin label attached to a membrane protein reconstituted into a lipid vesicle is probably anisotropic, but the correlation time may not be sub-nanosecond as is assumed in the anisotropic rotational diffusion model. In order to extract both the correlation time and order parameter from the EPR spectrum, spectral simulations and fitting are done using NLSL with the MOMD model. For more information refer to Chapter 4.

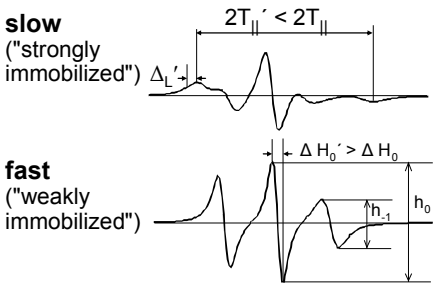

Figure 16. Strongly immobilized and weakly immobilized isotropic EPR spectra.

EPR spectra representative of slow and fast isotropic motion and the spectral features used to estimate correlation times. Figure adapted from [87].

2.4 Saturation Transfer EPR

Conventional dynamics is useful when the motion of the spin label is in the picosecond to nanosecond timescale, such as peptide backbone motion. If the goal is to measure the global dynamics of large protein complexes or large membrane bound proteins with rotational motion on the microsecond to millisecond timescale, saturation transfer EPR (STEPR) is required (Figure 17).

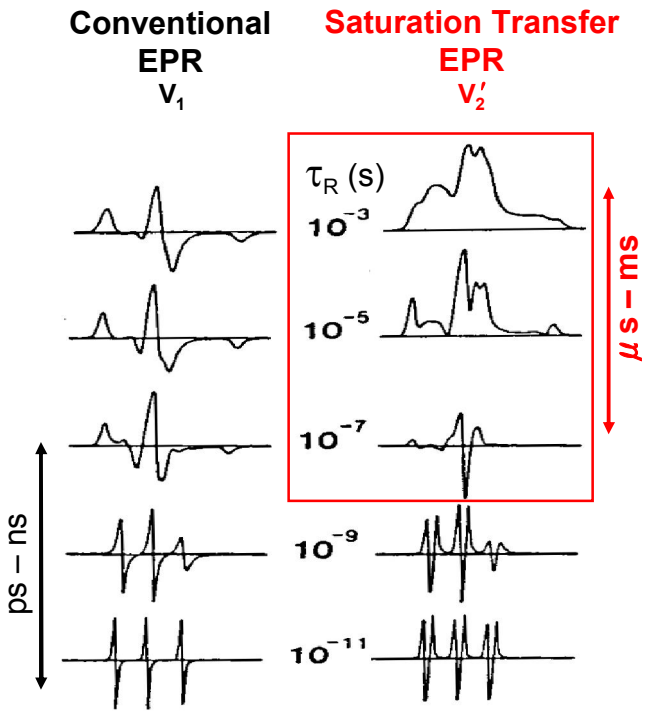

Figure 17. Conventional dynamics and saturation transfer EPR spectra.

Conventional dynamics (left) EPR is sensitive to spin label motion on the picosecond to nanosecond timescale while saturation transfer ERR (right) is sensitive to spin label motion on the microsecond to millisecond timescale [88].

Where conventional dynamics are sensitive to the spin label T_2 relaxation time (nanosecond timescale), STEPR dynamics are sensitive to the spin label T_1 relaxation time (microsecond timescale). In conventional dynamics, spectra are acquired at non-saturation microwave powers to avoid lineshape broadening due to spin system saturation. However, because STEPR measurements are based on T_1, sensitivity to rotational motion is achieved by using saturating microwave powers. This is because rotational motion is capable of transferring saturation from one part of the spectrum to another via spectral diffusion. Consequently, microsecond spin label motion which is faster than or comparable to T_1 is capable of transferring saturation while millisecond spin label motion is slower than T_1 and is unable to transfer saturation. In addition to using saturating microwave power, STEPR data are acquired as the second harmonic out-of-phase absorption spectra. Figure 18A shows three different sets of spectra representing fast (microsecond) and slow (millisecond) rotational correlation times. The V_1 spectra are first harmonic in-phase typical of conventional dynamics spectra. Here,

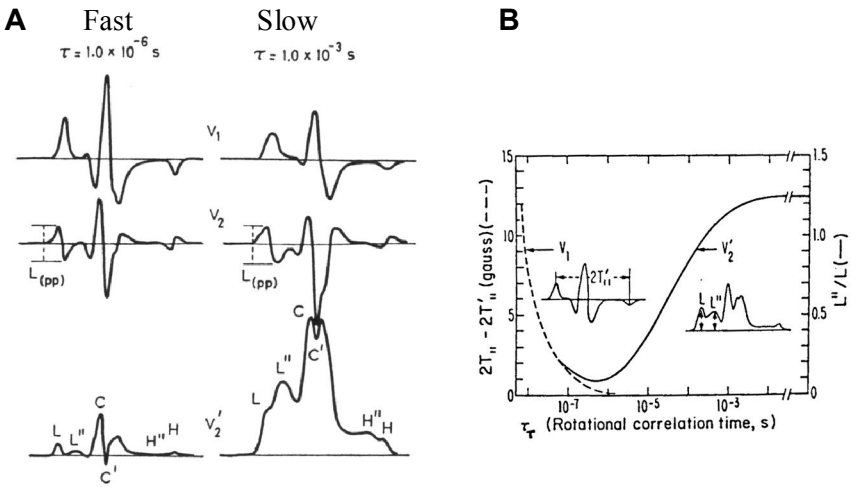

Figure 18. Saturation effects on fast and slow motion and an empirical plot to estimate rotational correlation time.

(A) Microsecond (fast) and millisecond (slow) rotational correlation time and the corresponding V_1, V_2 and V_2' spectra. The V_2' spectra show spectral features used to estimate rotational correlation time. (B) An empirical plot used to estimate rotational correlation time from conventional and STEPR spectra.

there is very little difference in the two spectra, other than saturation induced lineshape broadening of the slow spectrum. The V_2, second harmonic absorption spectra show little difference between microsecond and millisecond motion. Significant differences are only observed in the V_2' (second harmonic out-of-phase) spectra. Here, the shape and intensity of the STEPR spectra are highly dependent on rotational correlation time. A model system using spin labeled hemoglobin undergoing isotropic rotational diffusion in glycerol solutions of varying viscosities has been used to estimate rotational correlation time from the splitting (conventional ERP) and L''/L (STEPR) (Figure 18B). For more detailed information on the application of STEPR, refer to chapter 5.

2.5 Accessibility Measurements

Spin label accessibility has been used extensively to determine the environment of the spin labeled protein. More specifically, accessibility measurements are commonly used to determine if the spin label is buried in a membrane, solvent exposed or interacting with the bilayer surface.

Absorption of microwave radiation induces transitions from the ground state energy level to an excited state energy level, depleting the population of spins in the ground state level. Without spin-lattice (T_1) relaxation mechanisms to repopulate the ground state and return the spin system to the Boltzmann distribution, the system would become saturated and unable to absorb microwave radiation. The EPR signal (S) is dependent on the gyromagnetic ratio (γ), microwave magnetic field amplitude (H_1), the T_1 (spin-lattice) and T_2 (spin-spin) relaxation times:

$$S = \gamma H_1 T_2 / (1 + \gamma^2 H_1^2 T_1 T_2)$$ **Equation 11**

At low microwave power the T_1 relaxation mechanisms are sufficient to keep the ground state populated and the signal is linearly dependent on H_1. However, at sufficiently high microwave power, the T_1 relaxation mechanisms are insufficient to maintain the Boltzmann distribution, the system becomes saturated and the signal is no longer linearly dependent on H_1. When H_1 is high enough and $\gamma^2 H_1^2 T_1 T_2 = 1$, the signal intensity is ½ the value expected in an unsaturated system, a well characterized point defined as $P_{1/2}$, the corresponding microwave power value.

Microwave power (P) is proportional to H_1:

$$H_1 = CP^{1/2}$$ **Equation 12**

where C is a conversion factor which is dependent on the sample composition, sample volume, and sample placement in the resonator cavity. Since the EPR signal is dependent on H_1, but saturation measurements are commonly done as a function of microwave power, comparisons of $P_{1/2}$ values between samples can only be done if H_1 values are equivalent. This can be accomplished by either calibrating the system with a well characterized standard such as PADS to determine C, or by controlling sample composition, volume and placement within the resonator cavity such that the conversion factors are equivalent between samples. Power saturation experiments for my thesis work were performed by ensuring that the conversion factors between samples were equivalent.

A saturation rollover curve is generated by plotting the signal intensity (center line peak-to-peak height) as a function of microwave power. The normalized saturation (S_N) rollover curve is then generated by plotting $S/P^{0.5}$ as a function of microwave power (Figure 19). $P_{1/2}$ is determined by fitting the normalized saturation rollover curve with the following function

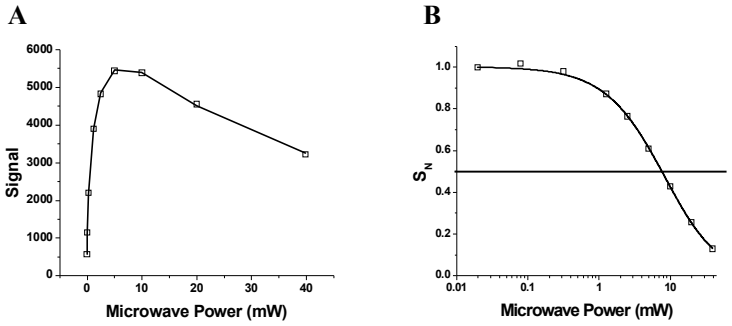

Figure 19. Saturation and normalized saturation rollover curves.

(A) Saturation rollover curve generated by plotting the signal intensity (centerline peak-to-peak height) as a function of microwave power. (B) Normalized saturation rollover curve generated by plotting $S/P^{1/2}$ as a function of microwave power.

$$S_N = I \cdot \left[1 + \frac{\left(2^{1/\varepsilon} - 1\right) \cdot P}{P_{1/2}} \right]^{-\varepsilon} \qquad \textbf{Equation 13}$$

where I is a scaling factor, P is the incident microwave power, ε is a measure of the homogeneity of the saturation line which varies between 0.5 (inhomogenous saturation) and 1.5 (homogenous saturation) and $P_{1/2}$ is the incident microwave power at half-saturation [89].

Paramagnetic relaxation enhancers (PREs) such as O_2 and transitions metal complexes containing Ni^{2+}, Cu^{2+}, or Gd^{3+} have spin-lattice (T_1) relaxation times much shorter than nitroxide spin labels. Collisional spin exchange between the PRE and the spin label results in a decrease in the spin label's spin-lattice relaxation time (T_1), thereby enhancing the spin label's spin-lattice relaxation rate, R_1. This enhanced R_1 consequently reduces the saturation of the spin system thereby increasing $P_{1/2}$ compared to an equivalent sample lacking a PRE. The difference in $P_{1/2}$ values due to the presence of the PRE is defined as $\Delta P_{1/2}$ (Figure 20). Thus, $\Delta P_{1/2}$ is proportional to the difference in spin-lattice relaxation rates ΔR_1 due to the collision frequency with the PRE. If the PRE concentration is constant, then if follows that $\Delta P_{1/2}$ is proportional to the accessibility of the spin label to the PRE.

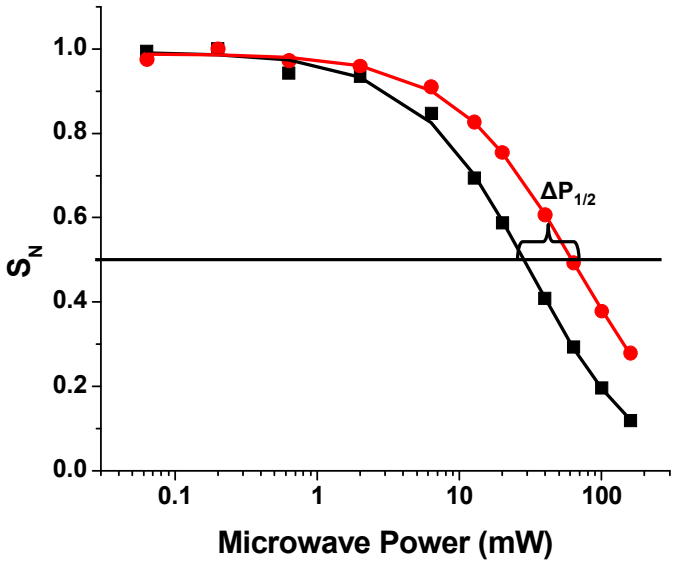

Figure 20. Normalized saturation curves showing $\Delta P_{1/2}$. Normalized saturation curves in the absence (black) and presence (red) of a PRE. The difference in $P_{1/2}$ values is defined as $\Delta P_{1/2}$ which is proportional to spin label accessibility.

This can be employed to determine the environment of the spin label. PRE solubility is dependent on the chemical nature of the relaxation enhancer. Accessibility of the spin label to the lipid bilayer can be probed using O_2, a PRE which is considerably more soluble in lipid than in water. Conversely, relaxation enhancers such as NiAA and NiEDDA are soluble in water and insoluble in the lipid bilayer. DOGS-NTA-Ni, a lipid

with Ni^{2+} chelated to the lipid headgroup can by used to measure accessibility to the bilayer surface. Accessibility measurements employing the theory outlined here are found in chapters three and six.

2.6 Distance Measurements

Distance measurements between two spin labels are based on the dipolar coupling principal. Consider a system of two spin labels, A and B in close proximity. The magnetic moment of spin B creates a small magnetic field which affects the applied field (H_0) felt by spin A. Since the spin state (spin-up or spin-down) of the A and B spins are independent of each other and the probability of spin B being up or down is equal, the magnetic field of spin B adds to or subtracts from the applied field. This splits the resonance field position of spin A (H_A) into two new positions separated by twice the dipolar coupling field (H_{dd}). The dipolar coupling is proportional to the inverse cube of the interspin distance (r) and is also dependent on θ, the angle between the interspin vector and H_0 (Figure 21). In continuous wave (CW) EPR spectroscopy, the dipolar

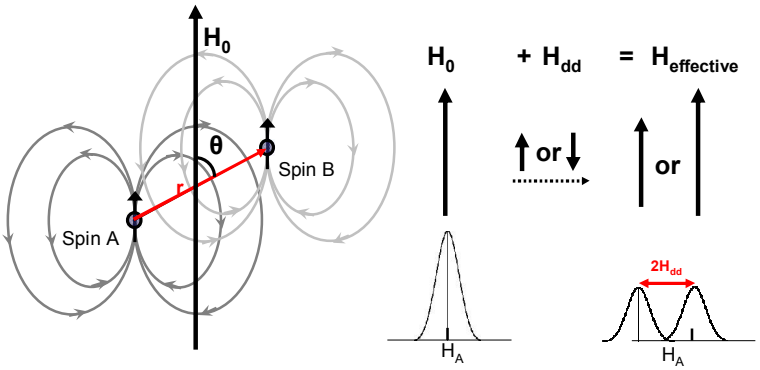

Figure 21. The dipolar coupling interaction.

The applied magnetic field (H_0) felt by spin A is affected by the small magnetic field of spin B. This dipolar coupling splits the resonance position of spin A (H_A) into two new resonance positions centered around H_A and separated by twice the dipolar coupling (H_{dd}). The dipolar coupling is proportional to the interspin distance (r) and (θ) the angle between the interspin vector and the applied magnetic field.

coupling broadens the EPR lineshape which is analyzed to determine the interspin distance. In pulsed EPR spectroscopy, the dipolar coupling frequency is directly detected in the double electron-electron resonance (DEER) time-domain experiment to determine the interspin distance.

CW is applied if the distance range is 1-2 nm and DEER is applied if the distance range is 2-5 nm. Both methods are sensitive to the mean and width of the distance distribution (Figure 22).

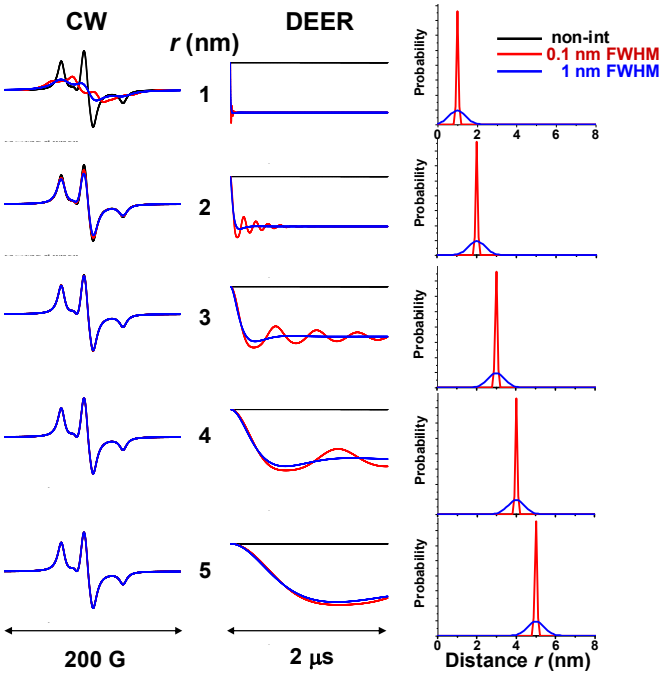

Figure 22. CW and DEER spectra and corresponding distance distributions.

Gaussian distance distributions with varying centers and full-width half-maximum values and the corresponding CW and DEER spectra. Black spectra are representative of a non-interacting system (no dipolar coupling). Red spectra correspond to the red Gaussian distance distributions representing little static disorder while blue spectra correspond to the blue Gaussian distance distributions representing moderate static disorder.

2.6.1 Continuous Wave Distance Measurements

CW distance measurements are applicable when the interspin distance is between ~ 0.8 nm and 2 nm. In order to determine the distance distribution, two spectra are required; a non-interacting spectrum comprised of a singly labeled protein (or monomer in my case) and an interacting spectrum comprised on a double labeled protein (or oligomer in my case). Because the EPR lineshape is sensitive to both rotational motion and dipolar broadening, samples are prepared with a cryoprotectant (usually glycerol), flash frozen and spectra

are acquired around 200K to ensure there is no rotational motion to affect lineshape. As stated above, the dipolar coupling between coupled spins causes a broadening of the EPR lineshape. The dipolar coupling strength can be calculated using the following equation:

$$H_{dd}(r,\theta) = \pm\left(\frac{\mu}{4\pi}\frac{g\beta}{r^3}(3\cos^2\theta - 1)\right)/2 \qquad \textbf{Equation 14}$$

where the μ is the permittivity of free space and the $\mu/4\pi$ factor is required for conversion to SI units. The cos^2 term dictates that the dipolar coupling will have maximum and minimum values when the interspin vector is parallel and perpendicular to H_0, respectively. Because most dipolar EPR samples are randomly oriented with respect to the magnetic field, θ is not a single value but rather a sine-weighted distribution of all possible values. Consequently, each resonance position is not split by H_{dd} but broadened by a Pake pattern:

$$P(H) = \frac{\alpha}{r^3}(H + \frac{\alpha}{2r^3})^{-1/2} + \frac{\alpha}{r^3}(-H + \frac{\alpha}{2r^3})^{-1/2} \qquad \textbf{Equation 15}$$

where $\alpha = \mu g\beta/4\pi$ and r is the interspin distance [90]. In most biological samples there is not a single discrete interspin distance but a distribution of interspin distances defined as ρ_r. Each value of r then has a corresponding Pake function which are summed to yield the broadening function, $P'(H)$

$$P'(H) = \int_0^\infty P(H,r)\rho(r)dr \qquad \textbf{Equation 16}$$

The dipolar broadened spectrum (V_{int}) is then the non-interacting (V_{non}) spectrum convoluted with the broadening function as defined below:

$$V_{\text{int}}(H) = \int_{-\infty}^{\infty} V_{non}(H')P'(H - H')dH' \qquad \textbf{Equation 17}$$

Simulation and fitting are used to extract the distance distribution from the dipolar broadened spectrum. Broadening functions are simulated from distance distributions and are then used to convolute the non-interacting spectrum. The resulting broadened spectrum is then fit to the experimental spectrum and the process is repeated until a non-degenerate solution is found.

2.6.2 Pulsed Distance Measurements

Generally, interspin distances greater than 2 nm cannot be resolved using continuous wave measurements because the dipolar broadening is less than the intrinsic linewidth. Pulsed EPR, specifically DEER is therefore employed if the interspin distances are expected to be greater than 2 nm (Figure 22).

DEER is a pulsed EPR technique which directly measures the dipolar coupling frequency of two coupled spins. For simplicity sake, consider a system where spin A is coupled to spin B. The resonant positions of the A and B spins, the pulse sequence and a typical DEER decay are shown in Figure 23. A $\pi/2$ pulse is first applied

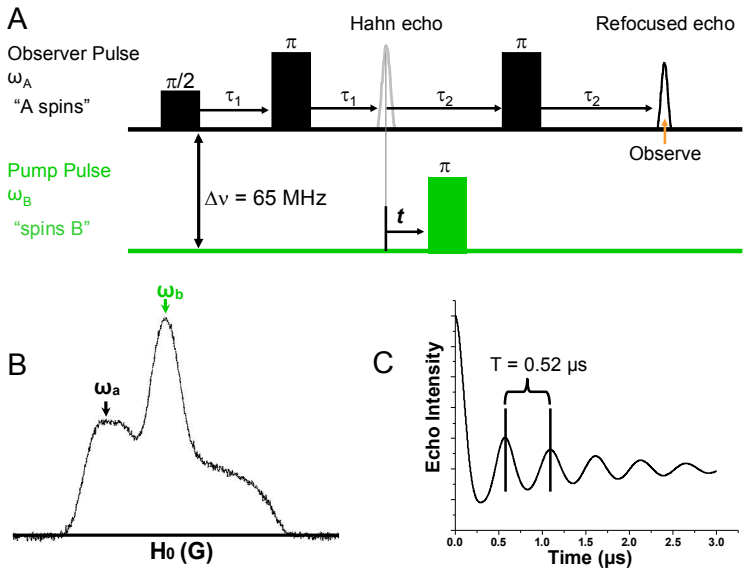

Figure 23. Typical DEER experiment.

(A) The 4-pulse DEER experiment showing the observer pulse sequence for the A spins and the pump pulse sequence for the B spins. (B) The echo-detected absorption spectrum showing the observation (ω_a) and pump (ω_b) frequencies for the A and B spins, respectively. (C) The DEER decay simulated from a Gaussian distance distribution with a center and FWHM equal to 3 nm and 0.1 nm, respectively. The x-axis is t, the timing of the ω_b pump pulse and the y-axis is the integrated refocused echo intensity. The oscillation frequency (T) is a function of the distance distribution and can be used to calculate the interspin distance.

to the A spins at frequency ω_a which tips the magnetization into the x-y plane. The spins begin to precess with the angular rage ω_A but due to local field inhomogeneities caused by phenomena such as spin-spin relaxation or dipolar coupling to other spins, the precession rates will slightly differ. For example, A spins coupled to B spins will precess with the angular rate $1/2\omega_{AB}$. These different precession rates dephase the spins which are subsequently refocused with a π pulse after τ_1 to form a Hahn echo. After time τ_2, another π refocusing pulse is applied to the A spins and a refocused echo at time τ_2 is integrated to generate the EPR signal. If a time dependent π pumping pulse is applied to the B spins at frequency ω_b between the Hahn echo and the second refocusing pulse, the

induced B spin flips will now cause the A spins to precess at angular rate -1/2$\omega_{AB.}$ This change in angular precession rate will dephase the A spins as a direct result of the dipolar coupling frequency.

The DEER decay, V(t). is a product of intramolecular and intermolecular dipolar coupling:

$$V(t) = V_{\text{int}\,ra}(t) \times V_{\text{int}\,er}(t) \qquad \textbf{Equation 18}$$

In order to analyze the DEER decay, the background signal ($V_{inter}(t)$) can be subtracted with the following function:

$$V_{\text{int}\,er}(t) = \exp(-kt^{d/3}) \qquad \textbf{Equation 19}$$

where k is the spin concentration and d is the dimensionality of the system, to yield a signal which is a function of only the intramolecular dipolar coupling such as in an oligomeric protein or a protein spin labeled at two different sites. The DEER decay due to intramolecular dipolar coupling is defined as:

$$V_{\text{int}\,ra} = V_0 \cos(\omega_{AB})(\tau - t) \qquad \textbf{Equation 20}$$

where V_0 is the echo amplitude in the absence of dipolar coupling, ω_{AB} is the dipolar coupling frequency, τ is the time between the $\pi/2$ and π pulses and t is the timing of the pump pulse (Figure 23). The dipolar coupling frequency is dependent on the angle between the interspin vector and the magnetic field (θ) and the interspin distance (r) and can be calculated from the following function:

$$\omega_{AB}(r,\theta) = \frac{g_A g_B \beta^2}{\hbar r^3}(3\cos^2\theta - 1) \qquad \textbf{Equation 21}$$

where g_A and g_B are the isotropic g values of the A and B spins, β is the Bohr magneton and $\hbar$ is the reduced Planck's constant. Just as in CW ERP a randomly oriented sample, such as a vesicle solution, θ is not a discrete value but assumes all orientations weighted by the sine function. In addition, r is unlikely to be a discrete value but a distribution of values. Consequently, ω_{AB} is a sum of Pake patterns (Equation 15) weighted by the interspin distance distribution.

CHAPTER 3. Spectroscopic Validation of the Pentameric Structure of Phospholamban

Spectroscopic Validation of the Pentameric Structure of Phospholamban

*Nathaniel J. Traaseth[1], Raffaello Verardi[2], Kurt D. Torgersen[2], Christine B. Karim[2], David D. Thomas[2], and Gianluigi Veglia[1,2]**

[1]Department of Chemistry, [2]Department of Biochemistry, Molecular Biology, and Biophysics, University of Minnesota, Minneapolis, Minnesota 55445.

*Corresponding Author

***Proc Natl Acad Sci U S A*. 2007. 104: 14676-14681. PMCID: 1976191**

Gianluigi Veglia
139 Smith Hall, 207 Pleasant St. SE
Minneapolis, MN 55455
Phone: (612) 625 0758
E-mail: veglia@chem.umn.edu

KEYWORDS: Phospholamban, Solid-State NMR, PISEMA, Oriented Bilayers, PISEMA, Membrane Protein, Ca^{2+}-ATPase, SERCA, Protein Dynamics, DEER, EPR

ABBREVIATIONS: Phospholamban, PLN; sarco(endo)plasmic reticulum Ca-ATPase, SERCA; dodecylphosphocholine, DPC.

Phospholamban (PLN) regulates calcium translocation within cardiac myocytes by shifting sarco(endo)plasmic Ca^{2+}-ATPase (SERCA) affinity for calcium. Although the monomeric form of PLN (6 kDa) is the principal inhibitory species, recent evidence suggests that the PLN pentamer (30 kDa) is also able to bind SERCA. To date, several membrane architectures of the pentamer have been proposed, with different topological orientations for the cytoplasmic domain: (*i*) extended from the bilayer normal by 50-60°; (*ii*) continuous α-helix tilted 28° relative to the bilayer normal; (*iii*) *pinwheel* geometry, with the cytoplasmic helix perpendicular to the bilayer normal and in contact with the surface of the bilayer, and (*iv*) *bellflower* structure, in which the cytoplasmic domain helix makes ~20° angle with respect to the membrane bilayer normal. Using a variety of cell membrane mimicking systems (i.e. lipid vesicles, oriented lipid bilayers, and detergent micelles) and a combination of multidimensional solution/solid-state NMR and EPR spectroscopies, we tested the different structural models. We conclude that the *pinwheel* topology is the predominant conformation of pentameric PLN, with the cytoplasmic domain interacting with the membrane surface. We propose that the interaction with the bilayer precedes SERCA binding and may mediate the interactions with other proteins such as protein kinase A and protein phosphatase 1.

Introduction

Calcium translocation into the sarcoplasmic reticulum (SR) of cardiac myocytes is controlled by the sarco(endo) plasmic reticulum calcium ATPase (SERCA). Phospholamban (PLN) regulates the activity of SERCA by shifting the apparent calcium affinity for the enzyme. This activity is relieved by phosphorylation of PLN at Ser16 and/or Thr17 or high calcium concentration within the cytosol. Wild-type PLN (wt-PLN) forms stable homopentamers in lipid bilayers and in detergent micelles, where each monomer is composed of a helical cytoplasmic domain (residues 1-16), a semiflexible loop (residues 17-21), and a helical transmembrane domain (residues 22-52) [47, 63]. Mutagenesis, molecular biology, and *in vivo* studies revealed that the PLN pentamer depolymerizes into active monomers that bind and inhibit SERCA [14]. Similar conclusions were reached by *in vitro* fluorescence studies [6]. Recently, Young and co-workers [66] have reported a cocrystal formed by SERCA and PLN pentamer, suggesting that the pentameric species is also able to bind SERCA. Furthermore, Jones and co-workers [91] hypothesized that the PLN pentamer may act as a chloride ion channel, which is supported by the *bellflower* structure recently determined by Oxenoid and Chou [63].

There are four principal proposed structural models of pentameric wt-PLN, which differ primarily in the topology of the more dynamic cytoplasmic domain. In each of these models (shown in Figure 24), residues 33-52 are in a coiled helix approximately parallel to the bilayer normal. The first model (*extended helix/sheet* model), based on polarized Fourier transform infrared (FTIR) spectroscopy in a supported lipid bilayer, has residues 22-32 to be in an antiparallel β-sheet configuration with the cytoplasmic domain helix oriented ~50-60° relative to the bilayer normal [61]. A second model (*continuous helix* model), based on rotational-echo double resonance (REDOR) solid-state NMR and polarized FTIR spectroscopy in lipid bilayers, depicts wt-PLN as a continuous helix [62, 92]. The third structural model (*pinwheel* model), based on fluorescence resonance energy transfer (FRET) in SDS gels, reveals a *pinwheel* arrangement of the pentamer, in which each monomer within the pentamer has an *L-shaped* geometry where the cytoplasmic domain is in contact with the lipid bilayer [64]. The most recent model (*bellflower* model), based on triple-resonance solution NMR in dodecylphosphocholine (DPC) detergent micelles, reveals a *bellflower* structure [63]. The *bellflower* model, like the *pinwheel* model, has three structural domains, but differs mainly in the pronounced bend in domain Ib (residues 22-31), and the cytoplasmic domain helices, which are oriented ~20° with respect to the bilayer normal. The ensemble

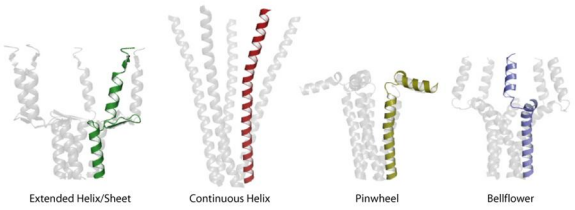

Figure 24. Structural models of wt-PLN. The extended helix/sheet and continuous helix models shown were reconstructed from the original papers [61, 62] to give the reader a graphical illustration of the models. Graphics were prepared using Pymol software (www.pymol.org). The pinwheel (1XNU [64]) and bellflower (1ZLL [63]) pentamers were taken directly from PDB coordinates.

for the *bellflower* is rather precise, having a root mean square difference of 0.6 Å for backbone atoms, indicating nearly no conformational disorder.

In contrast, the conformational ensemble of the PLN monomer has a much lower precision [47] due to psec-msec conformational disorder supported by EPR and solution and solid-state NMR spectroscopies [18, 51, 59, 75, 93]. Although the PLN structure is dynamic, extensive data in lipids and micelles shows that the predominant conformation of the monomer is *L-shaped*, with the cytoplasmic domain in contact with the surface of the lipid bilayer [47, 51, 55, 94, 95].

Recent spectroscopic data from Middleton [70, 71] and Lorigan [69, 96] groups suggest that the membrane association of the cytoplasmic domain of PLN is present in pentameric wt-PLN. These data are in disaccord with the *continuous helix* conformation, the *extended helix/sheet* model, and the *bellflower* structure.

In this manuscript, we use a combination of solution and solid-state NMR methods, as well as EPR techniques in both lipid bilayers and detergent micelles, to determine which, if any, of the proposed models is valid for wt-PLN.

Results

Characterization of Oligomerization State

To characterize the oligomeric states under our NMR and EPR conditions, we visualized PLN species using denaturing (SDS-PAGE) and non-denaturing (native) gel shift assays (Figure 31, Supporting Information). Both gels clearly show that in 1,2-dioleoyl-*sn*-glycero-3-phosphocholine (DOPC)/1,2-dioleoyl-*sn*-glycero-3-phosphoethanolamine (DOPE) lipid bilayers and DPC micelles, wt-PLN is pentameric.

Note that all of these preparations were tested for SERCA inhibition and under both NMR and EPR conditions PLN causes a shift in SERCA affinity for calcium as previously reported [18, 97]. These functionally identical preparations were then subjected to structural studies using both NMR and EPR spectroscopy.

Solid-State NMR in Oriented Lipid Bilayers

Solid-state NMR is the method of choice for the simultaneous identification of membrane protein structure, topology, and dynamics [98-100]. Unlike solution NMR, the ^{15}N chemical shift in solid-state spectra depends on its orientation with respect to the magnetic field. This basic principle allows for the measurement of orientation (topology) information with respect to the lipid membrane. Here, the [$^{1}H/^{15}N$] polarization inversion spin exchange at the magic angle (PISEMA) experiment was used. This experiment correlates ^{15}N chemical shift with ^{1}H-^{15}N dipolar coupling [101]. For α-helices within oriented lipid bilayers (B_0 parallel to the membrane normal), PISEMA spectra show wheel-like patterns called polarity index slant angle (PISA) wheels [102, 103]. From the PISA wheels it is possible to identify the tilt and rotation angles of the helix within the bilayer. Specifically, helices that are approximately parallel with respect to the bilayer normal give ^{15}N shifts ~200 ppm and ^{1}H-^{15}N dipolar couplings ~6-8 kHz, while those with an orientation perpendicular to the normal resonate at ~75 ppm and ~3-4 kHz, respectively. Because there are large orientation differences in the cytoplasmic domain within the four structural models, PISA wheel patterns measured in fully fluid lipid bilayers are able to distinguish between these models with high sensitivity.

Figure 25 shows an overlay of six different PISEMA experiments (high and low-field regions) acquired using selectively labeled [^{15}N-Leu], [^{15}N-Ala], [^{15}N-Ile], [^{15}N-Cys], [^{15}N-Thr], and [^{15}N-Asn] wt-PLN. The full PISEMA spectra are shown in the Supporting Information (Figure 32) indicating the degree of alignment for the samples. The overlaid spectra strongly show the presence of two PISA wheels for the transmembrane (Figure 25C) and cytoplasmic domains (Figure 25D). Residue assignments were carried out using an in-house software that exploits the periodic nature of the chemical shift and dipolar coupling for regular secondary structures [104, 105]. Analogous to the approach used by Nevzorov and Opella [106], this program uses an exhaustive search algorithm to find the assignment that best matches the observed resonances with those calculated from an ideal α-helix for given tilt (θ) and rotation (ρ) angles with respect to the lipid bilayer. The PISA wheel for the transmembrane domain of wt-PLN (Figure 25E) comprises 21 assigned resonances and reveals an ~15° tilt angle with respect to the bilayer normal. This tilt angle differs from that of the PLN monomer by ~6° [94], showing that formation of the leucine/isoleucine zipper imposes a smaller tilt

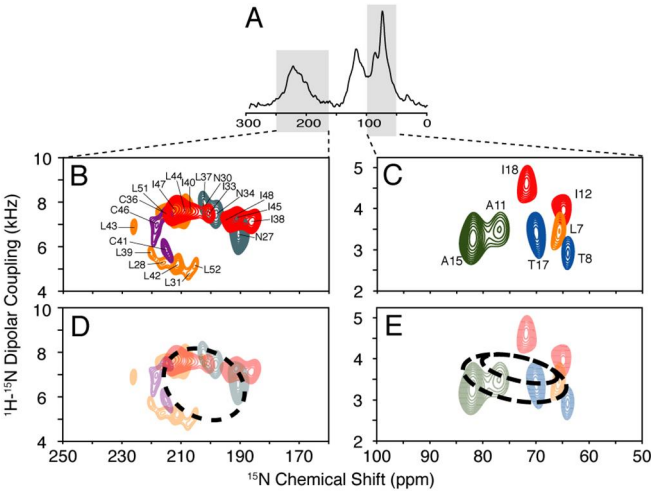

Figure 25. Solid-state NMR spectra of PLN pentamer in lipid bilayers. (A) 1D cross-polarization spectrum of [U-^{15}N] wt-PLN in DOPC/DOPE oriented lipid bilayers. (B and C) An overlay of selectively labeled PISEMA spectra for the transmembrane and cytoplasmic helixes, respectively. The resonances are color-coded: [^{15}N-Ala], green; [^{15}N-Cys], purple; [^{15}N-Leu], orange; [^{15}N-Ile], red; [^{15}N-Asn], grey; and [^{15}N-Thr], blue. (D and E) Simulated PISA wheels (dashed lines) for both transmembrane (θ = 15°) and cytoplasmic (θ = 92°) domains. The PISEMA simulations assumed a regular α-helical geometry for both helical domains.

to each monomer with respect to the depolymerized species. Two previous studies reported pentamer tilt angle values of 28 $\pm$ 6° [62] and 23° by using computation and mutagenesis [107]. The former study used dimyristoylphosphatidylcholine (DMPC) lipid bilayers. The difference in the tilt angle between our study and that of Arkin *et al*. [62] can be attributed to hydrophobic mismatch.

Unlike the change in tilt angle between the monomer and pentamer, the rotation angle of the transmembrane domain helix is very similar, indicating that the pentamer formation requires only a change in tilt angle to pack. Moreover, the regular PISA wheel obtained for the transmembrane domain shows an unbent helix, excluding the pronounced transmembrane helix curvature reported in the *bellflower* model as well as the proposed antiparallel β-sheet configuration for residues 22-32 in the *extended helix/sheet* model. The simulated PISA wheel in Figure 3E shows the expected pattern for the transmembrane domain within the *bellflower* structure. Note that the availability of Protein Data Bank (PDB) coordinates allows us to simulate PISEMA spectra for the *pinwheel* and *bellflower* models only.

Figure 25C shows the overlay of the upfield region (cytoplasmic domain) of the PISEMA spectrum (50-100 ppm). All of the expected resonances (Leu7, Thr8, Ala11, Ile12, Ala15, Thr17, and Ile18) are present for each selectively labeled sample, showing unambiguously that the cytoplasmic helix is oriented parallel to the surface of the lipid bilayer, supporting the *pinwheel* model. Structural fitting of an ideal PISA wheel gives an ~92° tilt angle of the cytoplasmic domain with respect to the bilayer normal, essentially the same as that previously described for the monomer [94]. A *bellflower* structure would give rise to cytoplasmic domain resonances within the range of 160-220 ppm (Figure 26B). Likewise the *continuous helix* and *extended helix/sheet* models would show the majority of cytoplasmic domain resonances in the same region as those expected for the *bellflower* model.

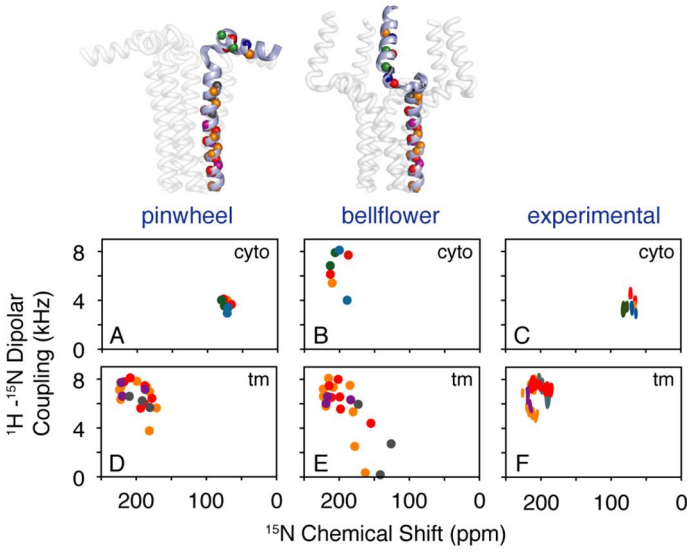

Figure 26. Simulated PISEMA spectra obtained for the pinwheel and bellflower models. The simulations for the cytoplasmic domain (A and B) assumed ideal α-helices with helix tilt angles of 92° (A) and 20° (B) with a rotation angle of 15°. PISEMA spectra for the transmembrane domains (tm) are calculated directly from the PDB coordinates (D and E). Unlike the pinwheel model, the bellflower model does not show any high-field resonances. Experimental PISEMA spectra show the remarkable agreement with the pinwheel model (C and F).

Solution NMR in DPC Micelles

Is the pentamer structure in micelles different from that in lipid bilayers? Following the sample preparation used by Oxenoid and Chou [63], we compared the transverse relaxation-optimized spectroscopy/heteronuclear sequential quantum correlation (TROSY-HSQC) spectrum of monomer and pentamer and tested the topology of the pentamer using three different paramagnetic probes: gadopentetate dimeglumine (Gd^{3+} for simplicity), 5′-doxyl stearic acid and 16′-doxyl stearic acid, which probe solvent exposed residues, hydrophobic residues underneath the phosphate headgroup, and those residues deeply embedded in the micellar core, respectively.

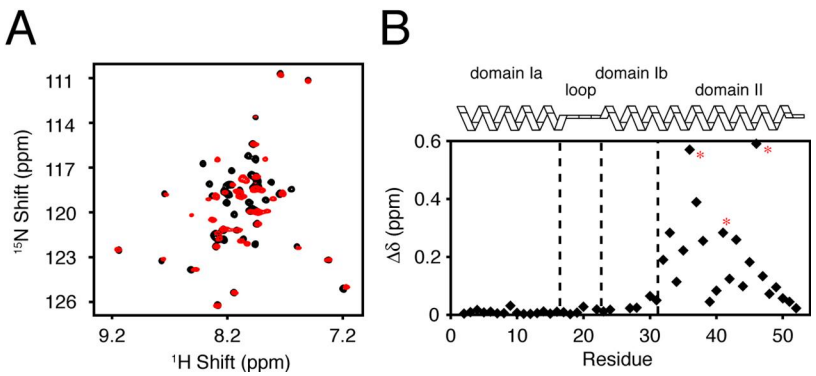

Figure 27. Solution NMR studies of PLN pentamer in DPC micelles. (A) Overlay of [^{1}H/^{15}N]-TROSY-HSQC spectra of AFA-PLN monomer (black) and wt-PLB pentamer (red). (B) Difference plot of the combined ^{1}H and ^{15}N chemical-shift variations between the monomeric and pentameric species ($\Delta\delta = [(\Delta\delta_H^2 + \Delta\delta_N^2/25)/2]^{1/2}$). The three mutations in AFA-PLN (C36A, C41F and C46A) are indicated with asterisks.

Remarkably, the resonance positions of the protein fingerprint in the [^{1}H/^{15}N]-TROSY-HSQC spectrum for residues 2-31 within wt-PLN and monomeric mutant AFA-PLN are nearly identical as shown in Figure 27. The largest differences between monomer and pentamer are located in domain II, resulting from the mutated residues and the quaternary interactions within the pentamer. The similarity in the cytoplasmic region (residues 2-31) suggests that the local chemical environment and the conformations for both monomer and pentamer are identical.

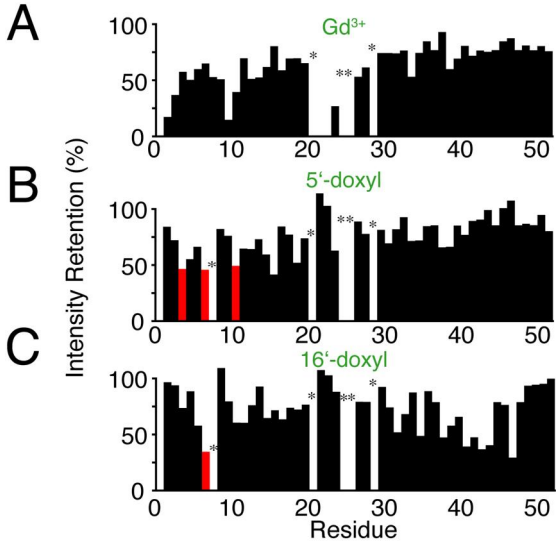

Figure 28. Paramagnetic mapping of PLN topology in DPC micelles. Intensity retention upon addition of Gd^{3+} (A), 5′-doxyl stearic acid (B), and 16′-doxyl stearic acid (C). The red bars in B and C highlight those residues quenched that face the micelle interior (Val-4, Leu-7, and Ala-11 in B and Leu-7 in C). The asterisks indicate overlapped resonances.

Figure 28A shows the intensity retention in the TROSY-HSQC spectrum of wt-PLN after adding Gd^{3+}. The quenching of residues Glu2, Lys3, Ser10, Gln22, Gln23 and Ala24 indicates that these residues are the most solvent-exposed, whereas the absence or minimal perturbation of the remaining residues of the transmembrane and cytoplasmic domains suggest that these are somewhat solvent-protected.

To investigate what residues were associated with or embedded within the DPC micelle, we used 5′- and 16′-doxyl stearic acid. Val4, Leu7, and Ala11 amide resonances are among the most quenched when exposed to 5′-doxyl stearic acid, whereas Ser10 (the most quenched in Gd^{3+} experiments) retains ~80% intensity (Figure 28B). Similarly, 16′-doxyl stearic acid shows Leu7 to be the most quenched in the cytoplasmic domain with

residues 41-45 embedded in the core of the micelle. These results support the conclusion that Val4 and Leu7 are buried in the micellar hydrophobic core, placing the cytoplasmic domain helix in contact with the surface of the micelle. If domain Ia (residues 1-16) were fully exposed to solvent, as in the *bellflower*, *continuous* helix, and *extended helix/sheet* models, one would expect to observe uniform quenching of these domains upon addition of Gd^{3+} and no differential quenching upon addition of 5′- or 16′-doxyl stearic acid. In the *pinwheel* model, one would expect to see differential quenching in the cytoplasmic domain from addition of Gd^{3+} and 5′-doxyl stearic acid, indicating a preferential surface for the cytoplasmic domain helix to interact with the lipid surface.

In summary, the similarity of spectra between the pentamer and monomer, and the topological mapping by paramagnetic agents, all establish that in DPC micelles both the monomer and pentamer have cytoplasmic domains that interact with the surface of the micelle.

EPR in DPC Micelles

To further test the structural models, we performed complementary EPR experiments. Although a single EPR experiment lacks the residue-by-residue view offered by NMR, it has several advantages stemming from the larger magnetic susceptibility of the electron, including increased sensitivity, resolution of distinct conformations based on dynamics [108], and the ability to probe distances up to 8 nm in length [109]. To measure intermonomer distances in the wt-PLN pentamer, a four-pulse double electron-electron resonance (DEER) experiment was used [109]. Wt-PLN was spin labeled at Lys3 with 2,2,6,6-tetramethylpiperidine-1-oxyl (TEMPO)-succinimide.

Assuming a rigid model, the shortest intermonomer distance for Lys3 is 3.8 nm in the *pinwheel* model and 2.0 nm in the *bellflower* model, as illustrated in Figure 6. The interaction between the spin labels is a dipole-dipole interaction (r^{-3} distance dependence). The closer the two spin labels are in space, the stronger the interaction between the dipoles and subsequently the faster the DEER decay curve relaxes. The results in DPC micelles are shown in Figure 29C, with the simulated decay curves based on the two models shown in solid lines. It is clear that the distribution of distances between the spin labels is in close agreement with those predicted using the *pinwheel* model. If the major population in detergent micelles were the *bellflower* arrangement, a much steeper decay would be expected, as illustrated in Figure 29C. Similar to NMR data, these EPR results indicate that, in DPC micelles, the *pinwheel* model is in much better agreement with the data than the bellflower model.

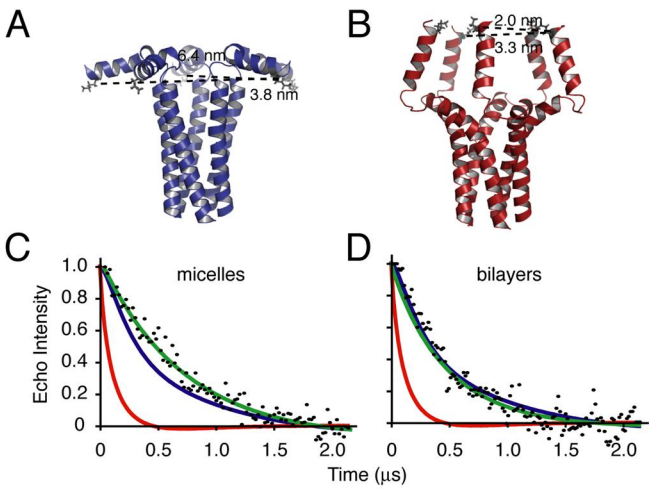

Figure 29. Structural models (A, pinwheel; B, bellflower) showing the sited of spin-label attachment (Lys-3) and the predicted interprotomer distances, measured from β-carbons. Pulsed EPR (DEER) decays (black squares) observed for wt-PLN, spin-labeled at Lys-3, in DPC micelles (C) and lipid bilayers (D). Solid curves in C and D show simulated decays predicted by the bellflower model (red), pinwheel model (blue) and the best-fit Gaussian distribution of distances (green).

EPR in Lipid Bilayers

DEER measurements were also performed on wt-PLN labeled at Lys3 with TEMPO-succinimide in DOPC/DOPE lipid bilayers. The results (Figure 29D) are only slightly different from those found in detergent micelles (Figure 29C), showing a decay profile that agrees well with the *pinwheel* model (blue curve). The decay in lipids is slightly faster than in micelles, indicating a slightly shorter distance that is in even better agreement with the *pinwheel* model, perhaps due to the curvature of the DPC micelle [110]. In both micelles and bilayers, at least 1 nm [half-width at half maximum, HWHM] of disorder in the *pinwheel* model (see Figure 33 and Figure 34, Supporting Information) is necessary to dampen the oscillations in the decay and fit the data. However, the *bellflower* model did not fit the data regardless of the amount of disorder modeled. The best fit of the data to a Gaussian distribution of distances (green curves in Figure 29C, D) is centered at 5.4 nm (HWHM 2.3 nm) in micelles (Figure 33B, D, Supporting Information) and 4.7 nm (HWHM 1.9 nm) in bilayers (Figure 34B, D), Supporting Information), which is in good agreement with the mean distance calculated using the *pinwheel* model (4.8 nm). In contrast, the best Gaussian fit to the *bellflower* model is a distribution of distances centered at 2.8 nm.

As shown previously [51, 75], EPR spectra of AFA-PLN, labeled in the cytoplasmic domain at either Lys3 with TEMPO-succinimide or at position 11 with 2,2,6,6-tetramethyl-piperidine-1-oxyl-4-amino-4-carboxyl (TOAC), have two dynamically dissimilar components within DPC micelles and DOPC/DOPE mixed lipid bilayers (Figure 30A, B). These two components are especially well resolved in the case of the 11-TOAC spin label (Figure 30B), which is attached rigidly to the α-carbon and thus accurately reflects the dynamics of the peptide backbone. The two components correspond to the T and R states of the PLN cytoplasmic domain [51], which are detected in DPC micelles by both EPR and solution NMR [75]. Also, a lipid anchor attached to the N-terminus of AFA-PLN stabilizes the membrane-bound conformation of the cytoplasmic domain, eliminating the EPR peak attributed to the R state [17], thus confirming that the R state corresponds to the more dynamic extended conformation (Figure 30).

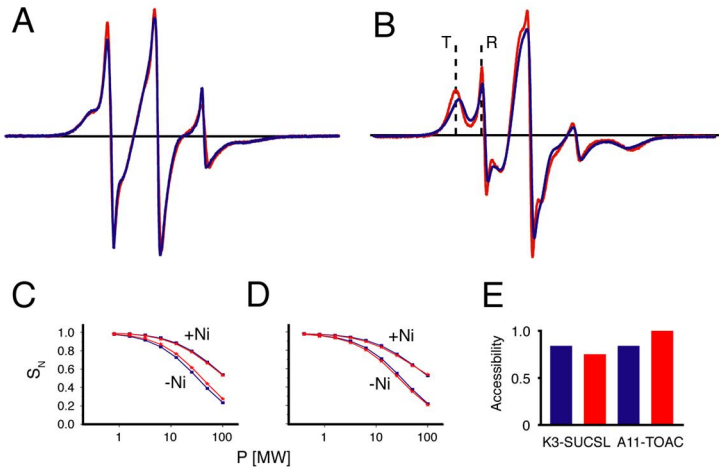

Figure 30. EPR dynamics (A and B) and Ni^{2+} accessibility (C-E) data comparing AFA-PLN (data shown in blue) and wt-PLN (data shown in red). EPR spectra were obtained from membrane-reconstituted PLN with TEMPO-succinimide (SUCSL) attached to Lys-3 (A and C) or with TOAC substituted for Ala-11 (B and D). In B, the two low-field peaks correspond to the resolved T and R states. C and D are progressive saturation curves, showing the enhanced relaxation caused by collisions with the membrane-surface-bound Ni^{2+}. Relative accessibilities derived from C and D are shown in E.

Figure 30A and Figure 30B shows that the spectra of AFA-PLN and wt-PLN in the same reconstituted DOPC/DOPE lipid bilayer system are nearly identical, indicating

that the T and R states have similar dynamics and mole fractions in the PLN pentamer and monomer. Two small but significant differences are seen: (*i*) in wt-PLN the mole fraction of the R state is slightly greater (9%) than in AFA-PLN (7%) and (*ii*) the resonance corresponding to the T state (or bent population) of wt-PLN has a larger splitting, indicating a slightly greater restriction of rotational motion than the corresponding T state in the monomer. Accessibility measurements using Ni^{2+} chelated to the lipid surface were also performed with both spin labels on AFA and wt-PLN (Figure 30C, D, E). These results show that both cytoplasmic spin labels interact strongly with the membrane surface, with little or no difference between AFA and wt-PLN. These results are in agreement with the solution NMR topological mapping using 5′- and 16′-doxyl stearic acids (Figure 28B, C).

In summary, all EPR results strongly support the conclusion that the predominant population of wt-PLN is one in which the overall geometry is a *pinwheel* with the cytoplasmic domain in direct contact with the surface of the bilayer.

Discussion

The fully-functional monomeric AFA-PLN mutant has been well-characterized by the G.V. and D.D.T. groups using solution NMR [18, 47, 59, 75, 93] and EPR in detergent micelles [75] , EPR in lipid vesicles [17, 51, 75], and solid-state NMR in mechanically oriented lipid bilayers [94]. In all of these experiments, the results are unambiguous: the major population of AFA-PLN is *L-shaped*. Our studies had focused on the monomeric mutant to study the complex with SERCA, given that the monomer is believed to be responsible for inhibition, as well as to eliminate potential complex

equilibria between various oligomers of wt-PLN. However, recent studies suggested that the pentameric form of PLN could play a larger role in SERCA regulation than was previously thought [66]. Therefore, we embarked in the elucidation of the structure and topology of the pentamer in lipid bilayers.

Four distinct structural models proposed for pentameric wt-PLN (Figure 1) differ primarily in the orientation of the cytoplasmic domain. In the present study, we investigated the topology of wt-PLN in detergent micelles, lipid vesicles, and oriented lipid bilayers using EPR and solution/solid-state NMR spectroscopies, representing the most exhaustive structural investigation of wt-PLN pentamer to date. Our data in detergent micelles and lipid bilayers all support the same conclusion: the cytoplasmic domain of wt-PLN, like that of the AFA monomer, lies on the surface of the membrane, supporting an overall *pinwheel* geometry for the pentamer.

The *pinwheel* model qualitatively describes the NMR and EPR data yet is not a definitive high-resolution structure of pentameric PLN. It was constructed based on the AFA monomer structure with the addition of three distance restraints measured using FRET [64]. Because the data in DPC micelles and lipid bilayers are consistent, the inclusion of restraints from a number of different techniques, including NOEs from solution NMR, DEER distance measurements from EPR, rotational-echo double-resonance (REDOR) distances from solid-state NMR, and PISEMA solid-state NMR restraints, should be used. This inclusion will reduce the ambiguity associated with data interpretation from one technique, further validating a structural model.

Although there are differences between a lipid bilayer and a detergent micelle (surface curvature, dynamics, *etc*.), the careful choice of a micelle has been shown to be a

good mimic for a physiological lipid environment [111, 112]. Furthermore, for our system, biological function can be tested directly under the conditions used for NMR experiments [18, 113]. In our case, DPC preserves both SERCA function and PLN inhibitory activity under NMR conditions [18, 75]. In the present study, our results in DPC micelles indicate that the monomer tree and within the pentamer adopt a similar structural and topological arrangement. Using both solid-state NMR and EPR, we also show that these structures are essentially the same in lipid bilayers.

A weakness of the previous studies is the complete reliance on the single data sets provided by each technique employed. For instance, the structure proposed by Oxenoid and Chou is heavily based on the use of residual dipolar couplings (RDCs). In fact, there are no distance restraints that keep the cytoplasmic domains perpendicular to the plane of the lipid bilayers. Although RDC measurements are a well-established method for obtaining long-range restraints and domain orientations [114-116], protein dynamics modulates the observed dipolar coupling [114, 117], complicating the interpretation of RDCs [117, 118]. Our analysis of RDC values for PLN monomer show that multiple orientations of the cytoplasmic domains are compatible with the RDC data, including the *L-shaped* and the *bellflower* conformations [104]. However, we selected those solutions that satisfied structural restraints as well as paramagnetic quenching experiments, simultaneously [47, 104].

In this article, we show that only a multitechnique approach is capable of converging to a unique solution. Specifically, anisotropic PISEMA solid-state NMR (Figure 25 and Figure 26), paramagnetic quenching data obtained by both solution NMR (Figure 28) and EPR (Figure 30E), and the long-range distance restraints provided by

EPR (DEER) data (Figure 29) all clearly demonstrate that only the *pinwheel* model is supported in both DPC micelles and in lipid bilayers. Finally, as illustrated in Figure 30, the EPR dynamics data (Figure 30B) show that the cytoplasmic domain of PLN is just as dynamic in the pentamer as in the monomer. The extended R state is dynamically disordered (order parameter, $S < 0.1$) and is a minor component (< 10%), whereas the bent T state (*pinwheel* structure) is the predominant population in both monomeric and pentameric PLN. Given the highly structured and tight ensemble of PDB ID code 1ZLL (*bellflower* structure), it is implausible that the dynamically disordered R state of pentameric wt-PLN detected in our experiments resembles the *bellflower* structure. One possibility, strongly indicated by the two-component EPR spectra of Figure 7B, is that the two states (T and R) represent the conformational equilibrium between a more stable, predominantly α-helical ensemble, and a more dynamic, less populated unfolded state [51]. Interestingly, phosphorylation at Ser16 by protein kinase A and single-site mutations at position 21, show the R state to become more populated, indicating the importance of preexisting equilibria necessary for SERCA recognition [17, 18, 59]. Similar conformational interconversions have also been detected for fd coat protein, in which lipids may induce different topologies consistent with either the arrangement in the virus coat or in the interaction with the lipid membrane [119-121].

In addition to our study, other spectroscopic data suggest association of the cytoplasmic domains of the pentamer with the lipid membrane. In particular, membrane association has been detected using ^{2}H and ^{31}P solid-state NMR with cytoplasmic domain peptides and full-length versions of wt-PLN by the Middleton [70, 71] and Lorigan groups [69, 96]. The interactions with the membranes or membrane-mimicking systems

induce a stable α-helical conformation. This process is reminiscent of the membrane association mechanisms proposed for small hormone or antimicrobial peptides [122] and of the prefolding states of membrane proteins identified by Engelmann and co-workers [123, 124].

Our results strongly support a *pinwheel* geometry as the predominant arrangement for the pentamer. In addition to this major conformation, we propose that the entire ensemble of conformations sampled by PLN and mediated by lipids is necessary for recognition by the main interacting partners: SERCA, protein kinase A, calmodulin-dependent protein kinase II, protein phosphatase 1, and the more recently found HS-1 associated protein X-1.

Materials and Methods

Protein Preparation

[U-^{15}N] wt-PLN (rabbit) was grown and purified in *E. coli* bacteria as previously described [97]. Selectively labeled wt-PLN was grown in a similar manner with addition of the ^{15}N labeled amino acid of interest (0.1 g/L) and the remaining 19 unlabeled amino acids (0.3 g/L).

For EPR experiments, wt-PLN or AFA-PLN samples were prepared by solid-phase peptide synthesis as described previously for AFA-PLN [51, 125]. For dynamics measurements, Ala11 was replaced by the TOAC spin label, which reports directly the dynamics of the peptide backbone [51]. For accessibility and distance measurements, wt-PLN was spin-labeled with TEMPO-succinimide at Lys3. Neither spin label had any effect on PLN function, as determined by inhibition of SERCA [51] or on pentameric

stability, as determined from SDS gels [49]. Inhibitory function was identical for expressed and synthetic PLN.

NMR Spectroscopy

Solution NMR samples were prepared by dissolving PLN in 300 mM DPC, 6M guanidinium hydrochloride, 50 mM 2-mercaptoethanol, 100 mM NaCl, and 25 mM phosphate buffer (pH 6.0). Samples were thoroughly dialyzed to remove all denaturant. PLN samples were ~0.4 mM in pentamer, and were stable over several weeks at 30°C for NMR measurements.

The [^{1}H/^{15}N]-TROSY-HSQC assignment of wt-PLN is based on the assignment previously published [63] with selectively ^{15}N labeled wt-PLN samples to resolve overlapping resonances. TROSY-HSQC experiments were used for the paramagnetic quenching experiments. Gd^{3+} (Magnevist; Bayer Schering Pharma, Berlin, Germany) and 5′- and 16′-doxyl stearic acids (Sigma-Aldrich) were titrated into wt-PLN (~0.4 mM in pentamer) to a final concentration of 3, 2, and 1 mM, respectively.

Oriented lipid bilayer preparations on glass plate supports have been described previously for a 4/1 molar mixture of DOPC/DOPE [94, 105]. Typical preparations used 4-8 mg of [^{15}N-Leu], [^{15}N-Ala], [^{15}N-Ile], [^{15}N-Cys], [^{15}N-Thr], and [^{15}N-Asn] wt-PLN. The final molar ratio of lipid/protein for all samples was ~125/1. All solid-state NMR experiments were acquired at 4°C.

PISEMA data were acquired at a 14.1 T field strength (^{1}H frequency of 600.1 MHz) equipped with a Bruker DMX spectrometer (National High Magnetic Field

Laboratory, Tallahassee, FL). The 2D PISEMA experiments [101] were performed at an RF field strength of ~60 kHz for cross-polarization, SEMA, and decoupling, using a low-E probe [126]. Additional details are provided in the Supporting Information.

EPR Spectroscopy

Spin-labeled PLN in lipid bilayer vesicles, containing 4/1 DOPC/DOPE (200/1 lipid/PLN monomer), were prepared as previously described [51]. Spin-labeled PLN in DPC micelles were prepared by dissolving the protein in DPC as described for solution NMR experiments (no reducing or denaturant agent) to a final PLN concentration of 0.3 mM.

EPR spectra were acquired using a Bruker EleXsys 500 spectrometer with the SHQ cavity. Samples (20 μL) were maintained at 4 ºC. The field modulation frequency was 100 kHz, with a peak-to-peak amplitude of 1 G. Accessibility of the spin label to the membrane surface was determined from progressive power saturation measurements, by g Ni^{2+} ions chelated to the lipid head group as previously described [51, 55].

Spin-spin distances were measured by DEER with a Bruker E680 pulsed EPR spectrometer (Billerica, MA) at X-band (9.5 GHz) [127]. One hundred-microliter samples were contained in 3 mm I.D. quartz tubes and flash-frozen in liquid nitrogen. The static field was set to the low-field resonance of the nitroxide signal. A four-pulse sequence was used with a 16 ns π/2 pulse [109, 127]. Temperature was controlled at 65° K during spectral acquisition, which lasted 8-12 hours. Data manipulations and other details are provided in the Supporting Information.

We thank P. Gor'Kov, W. Brey, R. Fu, and T. Cross for solid-state NMR experiments and M. Bonora, P. Fajer, and E. Howard for DEER experiments and simulations. We also thank L. Shi, J. Buffy, M. Gustavsson and Z. Zhang for technical support and discussion. This work was supported by National Institutes of Health Grants GM64742 and HL80081 and American Heart Association Grant 0160465Z (to G.V.); National Institutes of Health Grant GM27906 (to D.D.T.); American Heart Association Grant 0515491Z (to N.J.T.); and American Heart Association Grant 0615710Z (to K.D.T.). PISEMA spectra were acquired at the National High Magnetic Field Laboratory, Tallahassee, FL (DMR-0084173).

Supporting Information

Figure 31

Gel shift assays in denaturing (A, SDS-PAGE) and non-denaturing (B, native) gels. A) AFA-PLN monomer in 4/1 DOPC/DOPE lipids (lane 1) and DPC micelles (lane 3), and wt-PLN pentamer in DOPC/DOPE lipids (lane 2) and DPC micelles (lane 4). B) wt-PLN (lane 1) and AFA-PLN (lane 2) in DPC detergent micelles.

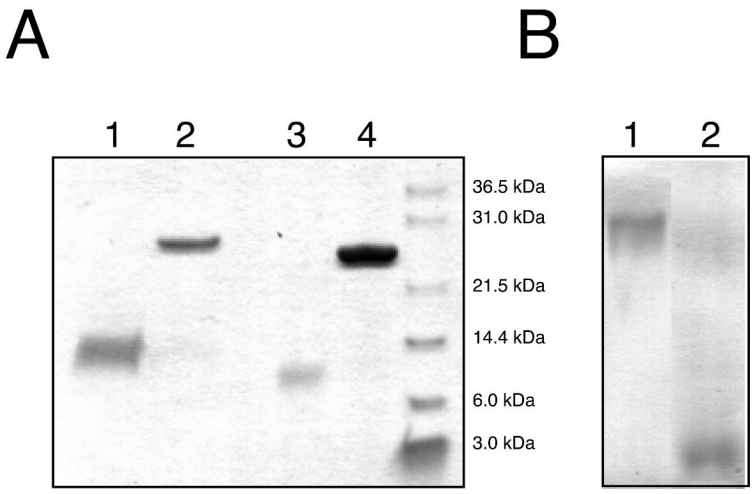

Figure 32

1D ^{15}N cross-polarization and PISEMA spectra of wt-PLN pentamer. A) Representative 1D cross-polarization spectrum of [^{15}N-Cys] wt-PLN. The three cysteine residues in the transmembrane domain (Cys-36, Cys-41 and Cys-46) indicate uniform alignment with no powder pattern present. The corresponding PISEMA spectrum is shown in the panel to the right. B) PISEMA spectra for the selective labels as indicated within the figure. The data are exactly the same as those shown in the Figure 25.

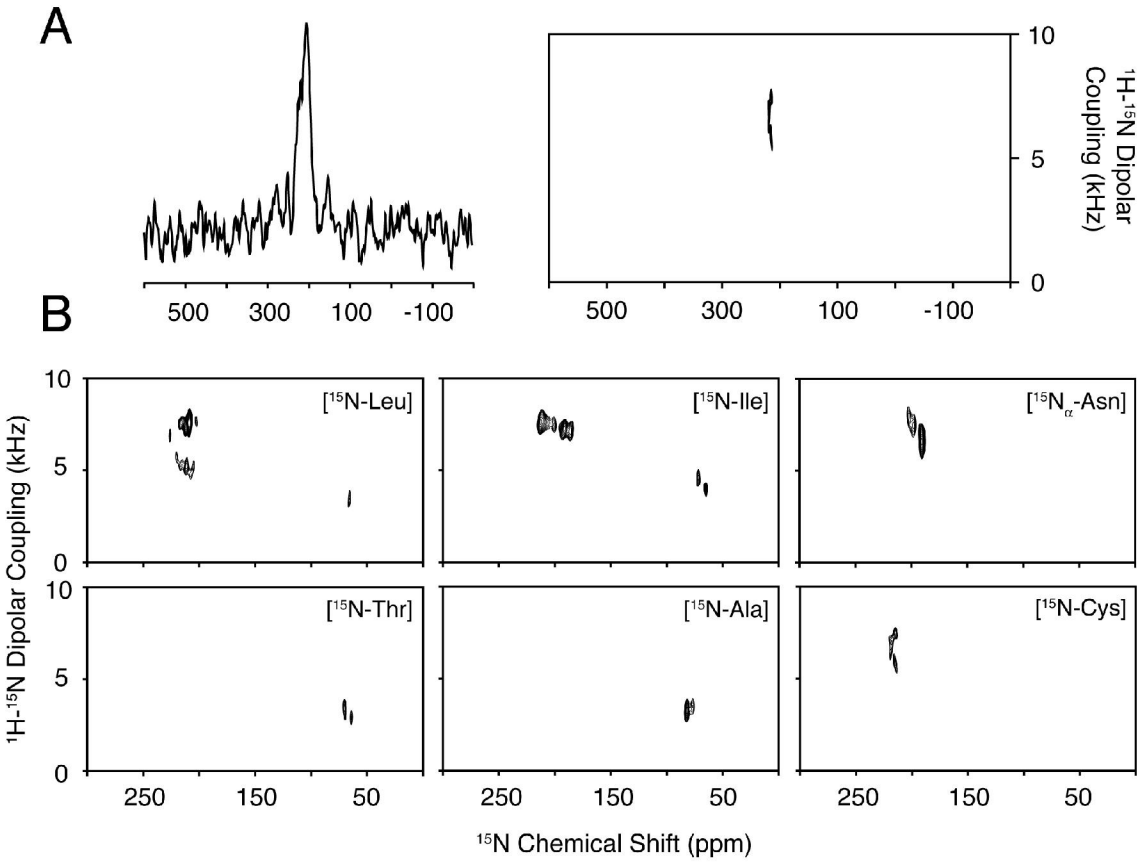

Figure 33

Supporting information for Figure 29C, illustrating the relationship between distance distributions (right) and DEER simulations (left) in DPC micelles. (Left) DEER data (black squares, same as in Fig. 6C) and simulated decays (colored curves). (Right) Distance distributions used to simulate the decays at left (with corresponding colors). Green curve: best fit single Gaussian distance distribution. Other colored curves correspond to simulations of the pinwheel model (upper) and bellflower model (lower), with distances shown in Fig. 6, convoluted with Gaussian functions having the indicated widths (HWHM). Note that (*i*) at least 1 nm (HWHM) of disorder is necessary to dampen the oscillations in the simulated decays, in agreement with data, and (*ii*) no amount of disorder in the *bellflower* simulations yields any overlap with the data.

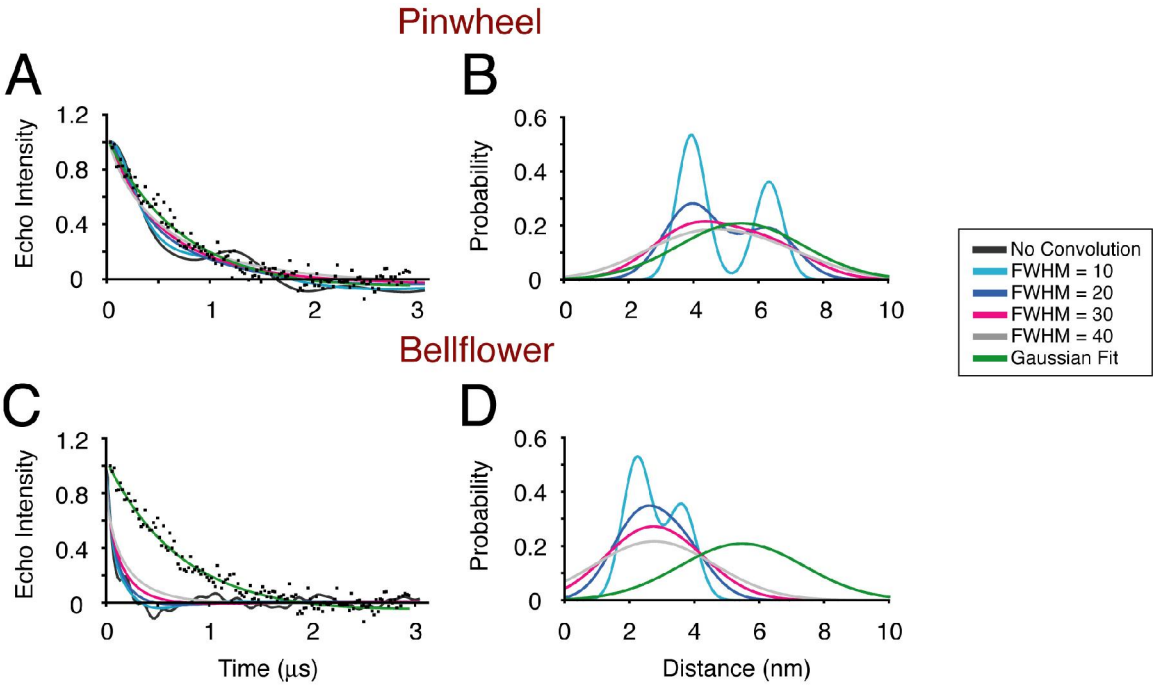

Figure 34

Supporting Information for Fig. 6D, illustrating the relationship between distance distributions (right) and DEER simulations (left) in lipid bilayers. Details are described in the legend to Figure 33.

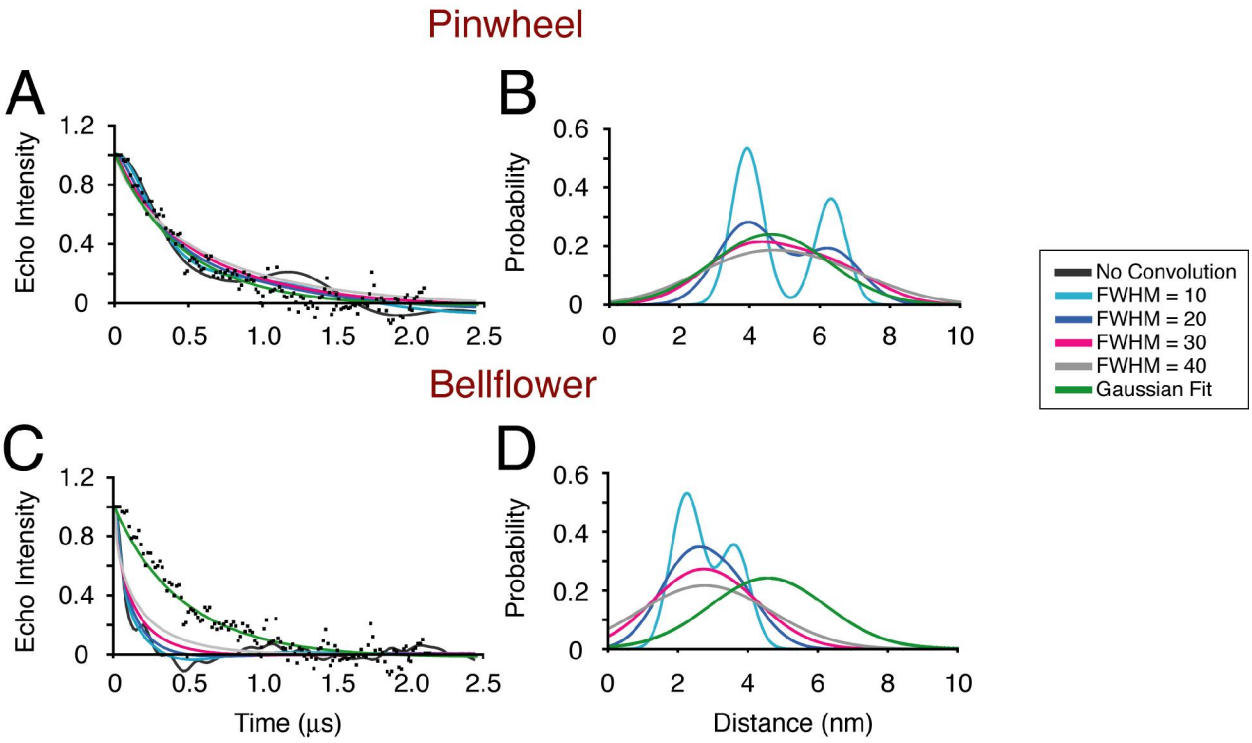

Supporting Information Methods

Solid-State NMR

PISEMA data were acquired at a 14.1 T field strength (^{1}H frequency of 600.1 MHz) equipped with a Bruker DMX spectrometer [National High Magnetic Field Laboratory (NHMFL), Tallahassee, FL]. The 2D polarization inversion spin exchange at the magic angle (PISEMA) experiment [101] was performed at a RF field strength of ~60 kHz for cross-polarization, SEMA (^{1}H effective RF field of ~ 60 kHz), and TPPM decoupling [128], by using low-E probes utilizing a doubly-tuned, low-inductance resonator built by the RF program at the NHMFL [126]. Both 4k scans and 12 t_1 increments were acquired for [^{15}N-Leu], [^{15}N-Cys] and [^{15}N-Ile] wt-PLN, 12k scans and eight t_1 increments for [^{15}N-Ala] and [^{15}N-Asn] wt-PLN, and 20k scans and eight t_1 increments for [^{15}N-Thr], using a recycling delay of 4 s. Data were processed with NMRPipe [129] software and viewed using NMRVIEW [130]. An exponential window function was applied utilizing 100-250 Hz line-broadening along the ^{15}N chemical shift dimension (t_2). After Fourier transformation and zero-filling, the data consisted of a total matrix size of 2k x 1k points.

EPR Spectroscopy

Spin-labeled PLN in lipid bilayer vesicles, containing 4/1 DOPC/DOPE (same as solid-state NMR; 200/1 lipid/PLN monomer), were prepared as previously described [51]. EPR samples of spin-labeled PLN in DPC micelles were prepared by dissolving the

protein in the DPC buffer (no reducing or denaturant agent) as described for solution NMR experiments to a final PLN concentration of 0.3 mM.

EPR spectra were acquired using a Bruker EleXsys 500 spectrometer with the SHQ cavity. Samples (20 μL in a 0.6 mm i.d. quartz capillary) were maintained at 4ºC. The field modulation frequency was 100 kHz, with a peak-to-peak amplitude of 1 G. The microwave power was 12.6 mW, producing moderate saturation (so that signal intensity was at least 50% of maximum) without significant perturbation to the spectral lineshape. Dynamics was analyzed using the NLSL program in terms of a two-component model for restricted rotational motion [51]. Accessibility of the spin label to the membrane surface was determined from progressive power saturation measurements, as described previously [51, 55]. In these experiments, spin-labeled PLN was reconstituted in lipid bilayers as described above, except that 5 mole % of the lipids contained Ni^{2+} ions chelated to the lipid head group (DOGS-NTA-Ni(II), Avanti Polar Lipids). Because of the extremely fast spin-lattice relaxation rate of Ni(II) (250 GHz) [131], the mechanism of relaxation enhancement is purely collisional, so this experiment measures directly the contact of the spin label with the membrane surface [55, 132].

Spin-spin distances were measured by DEER (double-electron-electron resonance), using a Bruker E680 pulsed EPR spectrometer (Bruker Spectrospin, Billerica, MA) at X-band (9.5 GHz) [127]. One hundred-microliter samples were contained in 3 mm I.D. quartz tubes and flash-frozen in liquid nitrogen, then loaded into an over-coupled MD5 dielectric resonator. The static field was set to the low-field resonance of the nitroxide signal. A four-pulse sequence was used with a 16 ns $\pi/2$ pulse [109, 127]. A 65 MHz frequency offset was used for the ELDOR pulse. Temperature was controlled at

65 K during spectral acquisition, which lasted 8-12 hours. In Figures 6, 10, and 11, echo intensity, with background signal subtracted (see below), is plotted as a function of evolution time. Data manipulations were accomplished with software developed by P. Fajer, and DEER simulations were performed from distance distributions with a program written by E. Howard; both were based on the software of G. Jeschke (available at http://www.mpip-mainz.mpg.de/_jeschke/). An exponential function fit to the tail of the raw data was used to subtract the homogenous background signal, so that the remaining signal reflects only intramolecular dipolar coupling; the evolution time was sufficiently long to ensure accurate observation of the background signal [133]. Two kinds of simulations were performed. First, discrete distance distributions were calculated directly from each of the two PDB models (*pinwheel* and *bellflower*), then convoluted by Gaussian functions of varying width (HWHM). Second, a simple Gaussian distance distribution was assumed, characterized by center and width, and these two parameters were varied in a least-squares minimization fit (Monte Carlo). In all cases in this work, the inclusion of a second Gaussian did not significantly improve the fits.

Blue native-PAGE

Blue native gels with 14% acrylamide separating gel and 4% stacking gel were prepared as described previously [134]. Cathode buffer was 50 mM tricine, 7.5 mM imidazole and 0.02% Coomassie blue G-250 at pH 7.0. Anode buffer was 25 mM imidazole at pH 7.0. Solution NMR samples (300 mM DPC in phosphate buffer) and solid-state NMR samples were diluted 1:10 with phosphate buffer and loaded onto the dry wells. Electrophoresis was carried out at 4 °C at constant voltage (30 V) for ~12 hr.

SDS-PAGE

Tris-tricine gels were prepared as described previously [135], containing 12% acrylamide in the separating gel and 4% in the stacking gel. Samples were diluted 1:10 in SDS sample buffer before loading. Running was carried out at 40 mA at 25°C. Gels were stained with 0.02% Coomassie brilliant blue R250.

Phosphorylation-Dependent Conformational Switch in Spin-Labeled Phospholamban Bound to SERCA

Christine B. Karim*, Zhiwen Zhang, Edmund C. Howard, Kurt D. Torgersen, and David D. Thomas

Department of Biochemistry, Molecular Biology and Biophysics, University of Minnesota, Minneapolis, Minnesota 55455

Corresponding author

***J Mol Biol*. 2006 358: 1032-1040.**

Running title: *Phosphorylation of spin-labeled PLB bound to SERCA*

Abbreviations used: EPR, electron paramagnetic resonance; PLB, phospholamban; SERCA, Sarco-endoplasmic reticulum Ca-ATPase; TOAC, 2,2,6,6-tetramethylpiperidine-1-oxyl-4-amino-4-carboxylic acid.

We have used chemical synthesis, functional reconstitution, and electron paramagnetic resonance (EPR) to probe the functional dynamics of phospholamban (PLB), which regulates the Ca-ATPase (SERCA) in cardiac sarcoplasmic reticulum. The transmembrane domain of PLB inhibits SERCA at low Ca^{2+}, but the cytoplasmic domain relieves this inhibition upon Ser 16 phosphorylation. Monomeric PLB was synthesized with Ala 11 replaced by the TOAC spin label, which reports peptide backbone dynamics directly. PLB was reconstituted into membranes in the presence or absence of SERCA. TOAC-PLB showed normal inhibitory function, which was reversed by phosphorylation at Ser 16 or by micromolar [Ca^{2+}]. EPR showed that the PLB cytoplasmic domain exhibits two resolved conformations, a tense *T* state that is ordered and a relaxed *R* state that is dynamically disordered and extended. PLB phosphorylation shifts this equilibrium toward the *R* state and makes it more dynamic (hyperextended). Phosphorylation strongly perturbs the dynamics of SERCA-bound PLB without dissociating the complex, while micromolar Ca^{2+} has no effect on PLB dynamics. A lipid anchor synthetically attached to the N terminus of PLB permits Ca-dependent SERCA inhibition but prevents the phosphorylation-induced disordering and reversal of inhibition. We conclude that the relief of SERCA inhibition by PLB phosphorylation is due to an order-to-disorder transition in the cytoplasmic domain of PLB, which allows this domain to extend above the membrane surface and induce a structural change in the cytoplasmic domain of SERCA. This mechanism is distinct from the one that relieves PLB-dependent SERCA inhibition upon the addition of micromolar [Ca^{2+}].

Keywords: Ca-ATPase, cardiac, EPR, calcium transport, regulation

Introduction

Phospholamban (PLB)[1] is a 52-residue integral membrane protein that regulates the enzymatic activity of SERCA in cardiac sarcoplasmic reticulum (SR) [136]. The SERCA-PLB calcium-regulatory system has been implicated in cardiovascular disease [7, 83, 85, 137-139]. Clarification of the physical mechanism by which PLB regulates SERCA is needed to develop strategies for rescuing the failing heart muscle.

Relief of inhibition does not require PLB dissociation from SERCA.

It has been suggested that relief of inhibition, due to phosphorylation of PLB, micromolar [Ca^{2+}], or mutation, is due to dissociation of PLB from SERCA, in a dynamic binding equilibrium, which also involves oligomeric interactions within PLB and within SERCA [7, 8, 14-16, 60, 140]. However, fluorescence resonance energy transfer (FRET) in functionally reconstituted membranes has shown that PLB binds tightly to SERCA in both the presence and absence of micromolar [Ca^{2+}], so Ca-dependent relief of inhibition must be due to structural rearrangement within the SERCA-PLB complex [15]. Similarly, other spectroscopic studies suggest that phosphorylation of PLB does not dissociate PLB from SERCA [141-144]. Thus in the present study we focus our attention on changes in the structure of the SERCA-PLB complex that occur with relief of inhibition due to phosphorylation of PLB or [Ca^{2+}] binding to SERCA.

Structural dynamics of PLB in micelles and lipids

PLB is predominantly a homopentamer in membranes, with a small fraction of monomer [6, 8], but it has been shown by electron paramagnetic resonance (EPR) [8, 60], fluorescence [145], and mutagenesis [6, 14, 146] that the less predominant monomeric

form of PLB is primarily responsible for inhibition of SERCA. Therefore, as in our previous studies, the present study focuses on a stable and fully functional PLB monomer, designated AFA-PLB, obtained by replacing the three Cys residues (36, 41, and 46) to Ala, Phe, and Ala, respectively [54]. A high-resolution structural model of AFA-PLB has been obtained by NMR in detergent micelles [47], and its orientation in lipid bilayers has been determined by solid-state NMR [95] and EPR [51, 55]. The result is a model in which two helical domains are connected by a five-residue (17-21) semi-flexible loop in an L-shaped configuration (Figure 35). NMR relaxation studies showed that PLB backbone structure in detergent micelles is actually quite dynamic throughout the cytoplasmic domain, especially in the region near the hinge-like loop [59].

TOAC spin label

In order to elucidate PLB structural dynamics with high resolution in lipid bilayers, we previously synthesized monomeric AFA-PLB with a spin label ("TOAC") rigidly coupled to the alpha carbon, which thus reports directly the nanosecond rotational dynamics of the peptide backbone at the labeled site [51]. A probe in the transmembrane domain showed little nanosecond motion, indicating a stable α-helix in this region,

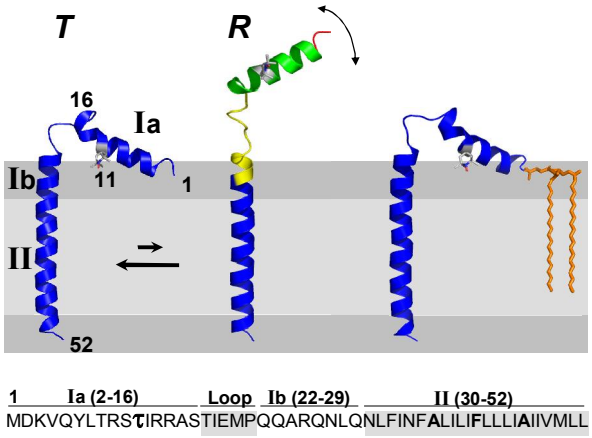

Figure 35: Two-state model for PLB structural dynamics in lipid bilayers, based on EPR of TOAC-spin-labeled PLB. Bottom: sequence of AFA-PLB with TOAC (τ) substituted for Ala at position 11. Left: cytoplasmic domain undergoes a dynamic equilibrium between *T* and *R* states. Right: a lipid anchor attached to the N-terminus stabilizes only the *T* state. The *T* state is depicted as the average NMR solution structure [47], while the *R* state (colored spectrally to indicate backbone dynamics increasing from blue to yellow to green to red [51]) is depicted as one of the more extended conformations from the ensemble of structures in that same NMR study.

whereas three probes in different parts of the cytoplasmic domain all exhibited clearly a dynamic equilibrium between two conformational states, a predominant one (*T*, "tense") that is helically ordered, and a minor population (*R*, "relaxed") that is dynamically disordered on the nanosecond time scale, and is probably extended. The "*T*" and "*R*" nomenclature is used to discuss the cooperative allosteric interactions with SERCA that perturb the equilibrium between these two states [75]. We showed that the ordered conformation is stabilized by interaction with the membrane surface (Figure 35*T*), whereas the dynamically disordered (extended) form (Figure 35*R*) is poised to interact with SERCA, shifting the cytoplasmic domain above the membrane surface [55]. Both EPR and NMR studies in detergent micelles, and EPR in lipid bilayers, indicate that SERCA binds preferentially to the *R* conformation, consistent with an allosteric regulation mechanism [75]. NMR relaxation studies in micelles show that this conformational switch is affected by phosphorylation, which induces a further disorder-to-order transition [59].

In the present study we use TOAC-spin-labeled PLB to determine the changes in PLB structural dynamics in its regulatory complex with SERCA in lipid bilayers, when inhibition is relieved by Ca^{2+} binding to SERCA or phosphorylation of PLB. The effects of phosphorylation on these EPR spectra, in the presence and absence of SERCA, reveal new details about the role of structural dynamics in PLB regulation of SERCA. The effect of a lipid anchor attached to the N-terminus of the cytoplasmic domain provides new insight into the importance of the cytoplasmic domain for the reversal of inhibition by phosphorylation.

Results

Secondary structure

Circular dichroism (CD) spectra (Figure 36) show that both AFA-PLB and its phosphoserine 16 derivative (Ser(P)16-AFA-PLB) are 85-90% α-helical in lipid bilayers under EPR conditions, with a negligible change in helicity due to phosphorylation (-3% ± 5%). Similarly, phosphorylation had a negligible effect on the CD spectrum (not shown) under NMR conditions [59] (phosphate-buffered saline, pH 6.0, containing 300 mM DPC, at 37° C).

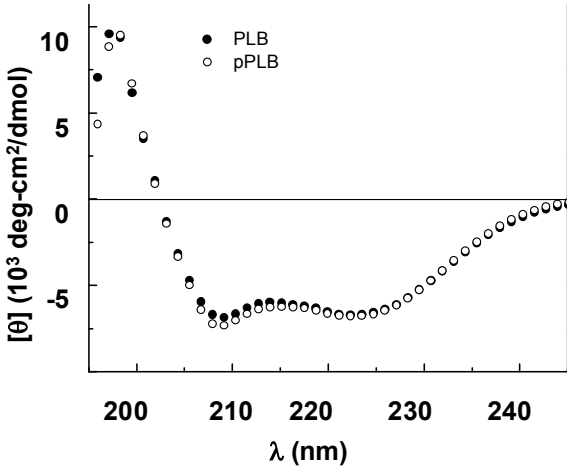

Figure 36: CD spectra of AFA-PLB , and its phosphorylated derivatives – in DOPC/DOPE bilayers (50:1 lipid: peptide) 10 mM Tris, pH 7.0. CD spectra were recorded on a Jasco J-710 spectrophotometer at 25°C and analyzed as previously reported (Lockwood 2003). Spectra are plotted as mean residue ellipticity, [θ].

Phosphorylation of Ser 16 relieves SERCA inhibition

The inhibition of Ca-ATPase activity was quantified by the shift in pK_{Ca} (the pCa value required for 50% activation). We showed previously that AFA-PLB has similar inhibitory activity as WT-PLB, and that AFA-PLB retains inhibitory potency when Ala 11 is replaced by TOAC [51]. This is confirmed in Figure 37A, which shows that 11-TOAC-AFA-PLB induces a 3-fold increase in K_{Ca}, shifting pK_{Ca} from 6.40 ± 0.02 to 6.11 ± 0.02. This inhibitory activity was almost completely reversed by synthetically engineered phosphorylation (Figure 37A), shifting pK_{Ca} to 6.29 ± 0.02. We showed previously that essentially the same inhibitory effects are caused by unlabeled wild-type

PLB [51], except that phosphorylation completely reverses the inhibition [147]. These experiments were performed in the presence of excess PLB (10 PLB/SERCA) in order to assess the full effect of spin-labeled PLB, whereas EPR experiments were performed with excess SERCA, in order to assess the full effect of SERCA on PLB. Under EPR conditions (0.5 PLB/SERCA, pCa 6.5) SERCA inhibition was 42 ± 10% of the maximal inhibition (10 PLB/SERCA), indicating that essentially all of the spin-labeled PLB is interacting functionally with SERCA. Under these same EPR conditions, inhibition by spin-labeled PLB was completely relieved at pCa 5, and was relieved by more than half upon PLB phosphorylation, again indicating that the EPR data comes from PLB that has normal functional coupling with SERCA.

Effect of SERCA and phosphorylation on EPR-detected dynamics

As we showed previously [51], the cytoplasmic domain at position 11 reveals a dynamic equilibrium between two resolved conformations of the peptide backbone, corresponding to ordered (helical, "*T* state") and dynamically disordered (extended, "R state") conformations, as shown in Figure 37B. Addition of SERCA increases substantially the population in the *R* state (Figure 37B to C), suggesting that SERCA binds preferentially to this extended state [75], as depicted in Figure 37C. Phosphorylation at S16 (Figure 37B to D) has a qualitatively similar but much greater effect on PLB, increasing substantially the population in the *R* state. On the other hand, SERCA *decreases* the dynamics (decreases the *R* state population) of phosphorylated PLB (Figure 37D to E); and phosphorylation *decreases* the dynamics of SERCA-bound PLB (Figure 37C to E). If phosphorylation caused PLB to dissociate from SERCA, there would be no difference between spectra D and E in Figure 37, and phosphorylation of

SERCA-bound PLB would increase the *R* state population. Neither is observed; indeed, phosphorylation of SERCA-bound PLB causes the opposite of the predicted effect. *Thus phosphorylation, which relieves SERCA inhibition by PLB (Figure 37A), does not dissociate PLB from SERCA, but rather changes the conformation of SERCA-bound PLB.* As illustrated in Figure 37 and discussed below, these results support a model in which the dynamically disordered (*R*) conformation of the PLB cytoplasmic domain facilitates the binding of PLB to SERCA in an inhibitory complex, but phosphorylation produces an even more disordered PLB conformation that binds differently to SERCA and relieves inhibition.

Lipid anchor prevents functional and structural effects of phosphorylation

In the presence of the N-terminal lipid anchor, normal inhibition was observed, but phosphorylation failed to reverse this inhibition (Figure 38A) as it does in the absence of the anchor (Figure 37A). EPR shows that the ordered (*T*) conformation of PLB is stabilized by the lipid anchor, and the dynamically disordered (*R*) conformation is virtually absent, regardless of the presence of SERCA or phosphorylation (Figure 38B-E). As illustrated in Figure 38 and discussed below, these results support the conclusion that *neither the R state nor interaction with the SERCA cytoplasmic domain are requried for SERCA inhibition, but both are required for reversal of inhibition due to phosphorylation*, as illustrated in Figure 37.

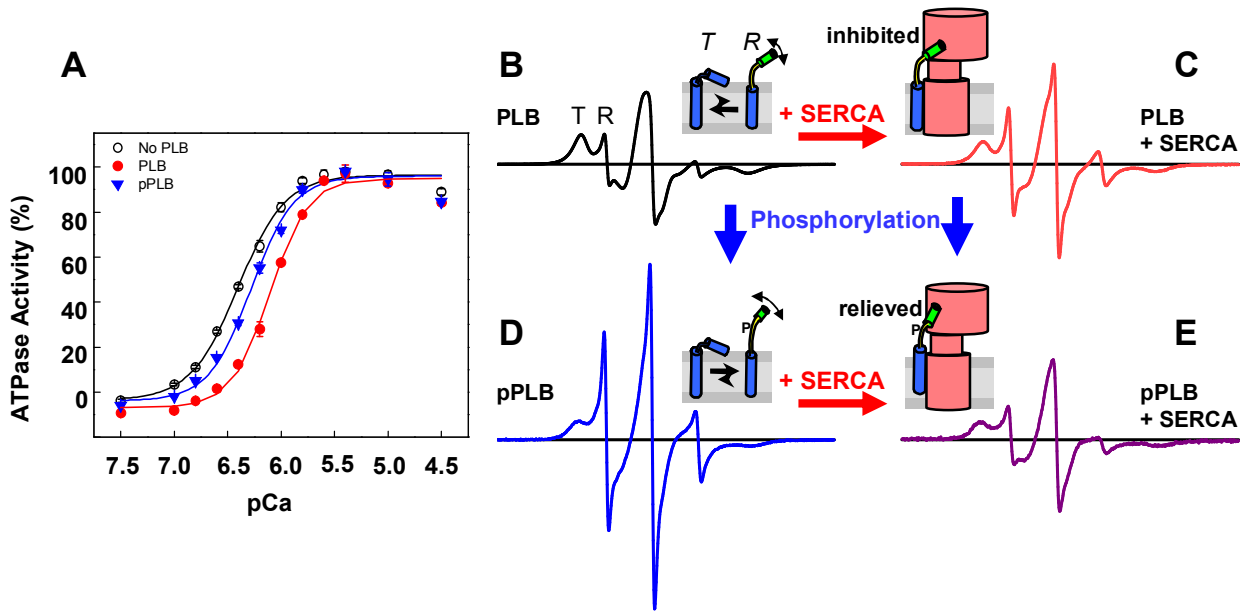

Figure 37: Effect of phosphorylation at Ser 16 on inhibitory function (A) and EPR-detected dynamics (B-E) of AFA-PLB, spin-labeled with TOAC at position 11 and reconstituted with SERCA in lipid bilayers. A: Data sets were fit by Eq. 1 and plotted as V/V_{max}. Each point represents the mean ($n \geq 6$); in most cases, SEM was smaller than the plotted symbol. B-E: EPR spectra. Top row (B, C) unphosphorylated. Bottom row (D, E): phosphorylated. Left column (B, D): no SERCA. Right column (C, E): 2 SERCA per PLB. Spectra were normalized to unit concentration by dividing by the double integral. Scan width 120G, 4° C. Drawings illustrate a structural model consistent with the data, as discussed in more detail in Figure 41.

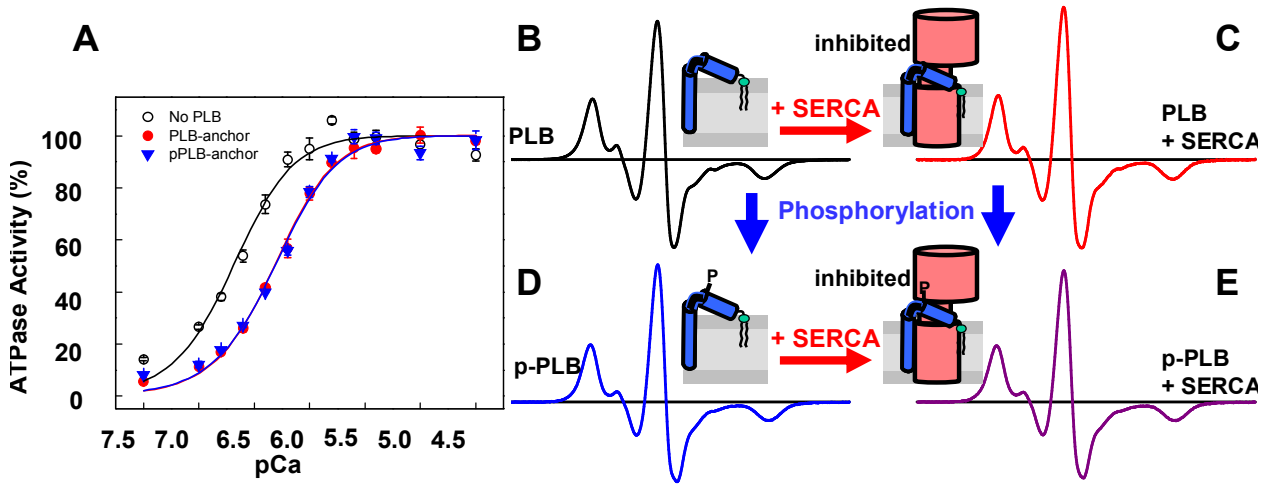

Figure 38: Effect of a lipid anchor, attached to the N terminus of 11-TOAC-AFA-PLB, on the data in Figure 37.

Quantitative analysis of dynamics

The results of Figure 37 and Figure 38 are represented more quantitatively in Figure 39, which shows rotational dynamics parameters obtained from spectral simulation and fitting. In the absence of the lipid anchor (Figure 39, left), unphosphorylated PLB (black) spends only 7% of its time in the dynamically disordered *R* state ($X(R)$ = .07), which is characterized by a subnanosecond correlation time (τ_R = 0.3 ns) and a very low order parameter (S = 0.2, implying an angular amplitude exceeding 70 degrees). The predominant *T* state is much less dynamic, with a much higher order parameter (S = 0.62, corresponding to an angular amplitude of about 40 degrees) and much longer correlation time (τ_R = 3 ns). The primary effect of phosphorylation on isolated PLB (Figure 39, blue) is to increase $X(R)$ by a factor of 3, while increasing the dynamics of this population (decreasing both S and τ_R). Thus phosphorylation increases PLB dynamics in two ways, shifting the equilibrium toward *R* and making the *R* state even more dynamic, causing it to be hyperextended, as illustrated in Figure 37B and Figure 40B. There was little or no effect

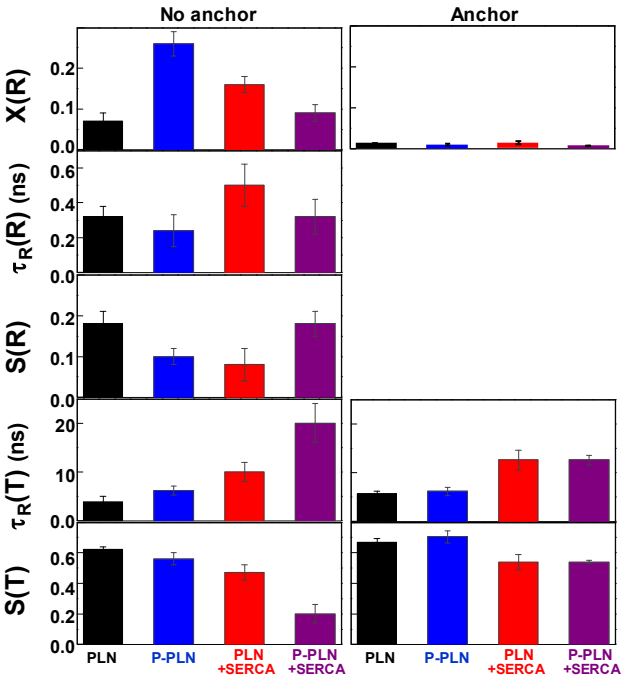

Figure 39: Results of EPR spectral analysis of rotational dynamics, for spectra in **Figure 37**B (left) and **Figure 38**B (right). $X(R)$ is the mole fraction of the *R* component. S = order parameter, τ_R = rotational correlation time. Parameters $S(R)$ and $\tau_R(R)$ were not determined in the presence of the lipid anchor, due to the small values of $X(R)$.

of phosphorylation on the mobility of the more restricted *T* state (characterized by $S(T)$ and $\tau_R(T)$) , which is stabilized by its contact with the lipid surface.

When unphosphorylated PLB binds to SERCA (Figure 39, red), the *R* state becomes more populated and more disordered. Thus the effect of SERCA is similar to that of phosphorylation, in that it induces an order-to-disorder transition, but the effect is clearly different: SERCA causes a much smaller increase in $X(R)$, and it induces much slower dynamics (greater τ_R) for both components. When PLB is phosphorylated in the presence of SERCA (Figure 39, purple), the *R* state becomes less populated (decreased *X*) and more ordered (increased S), producing dynamics that are quite different from that of phosphorylated PLB in absence of SERCA (Figure 39, blue). Thus it is clear that phosphorylation does not relieve inhibition by dissociating PLB from SERCA, but rather decreases the dynamics of bound PLB (Figure 39).

The principal effect of the lipid anchor (Figure 39, right) is to virtually eliminate the dynamic *R* state, reducing $X(R)$ to very low values. The remaining *T* state is similar to that observed in the absence of the anchor (Figure 39, right), supporting the conclusion that the *T* state is stabilized by contact with the lipid surface. There are slight but significant effects of SERCA on the *T* state, increasing $\tau_R(T)$ but decreasing $S(T)$, so it is not clear whether the anchored cytoplasmic domain interacts with SERCA at all. The lipid anchor completely prevents the effects of phosphorylation. These results support the conclusion that phosphorylation acts through its effects on the *R* state, which (in the absence of the anchor) increases in population, becomes hyperextended, and interacts with the cytoplasmic domain of SERCA, relieving inhibition (Figure 37).

Ca^{2+} has no effect on PLB dynamics in the presence of SERCA.

The experiments on SERCA-PLB complexes in Figure 37C and E (no lipid anchor) and in Figure 37C and E (lipid anchor) were carried out at both pCa = 6.5 (where SERCA inhibition is maximal) and pCa = 5.0 (where SERCA is not inhibited by PLB), with no difference detected. The EPR spectra at the two pCa values were essentially identical. Quantitatively, it was found that this variation in pCa changed the mole fraction X(R) by no more than 0.01. We can not rule out the possibility that Ca^{2+} affects the structure of PLB, or its interactions with SERCA, at a site distant from the spin-labeled site (position 11) [148]. However, it is quite clear that *(a) Ca^{2+} does not relieve inhibition by dissociating PLB from SERCA , (b) relief of SERCA inhibition by Ca^{2+} does not require the PLB cytoplasmic domain to rise above the membrane surface, and (c) phosphorylation and Ca^{2+} relieve SERCA inhibition through different mechanisms.*

Discussion

Phosphorylation or SERCA induces an order-to-disorder transition in PLB.

Figure 40 illustrates a model for a two-state conformational equilibrium in PLB, consistent with the data in Figure 37 (B to D), and with previously published EPR and NMR studies [47, 51, 55, 75]. The cytoplasmic domain of PLB undergoes an equilibrium between at least two states, an ordered state that is similar to the L-shaped NMR solution structure (Figure 40A, T) and a dynamically disordered state in which the central part of this domain is unfolded (Figure 40A, R) and thus able to extend above the membrane surface and interact with the SERCA cytoplasmic domain. Phosphorylation increases PLB disorder in two ways, shifting the equilibrium toward the *R* state (increasing X(R), Figure 39), and making the *R* state itself even more disordered (decreasing S(R), Figure 39), justifying the new label R' for this hyperextended state (Figure 40B). This phosphorylation-induced order-to-disorder transition is consistent with previous NMR relaxation studies in DPC micelles [59]. Since only the phosphorylated state relieves SERCA inhibition, we propose that the hyperextended R'

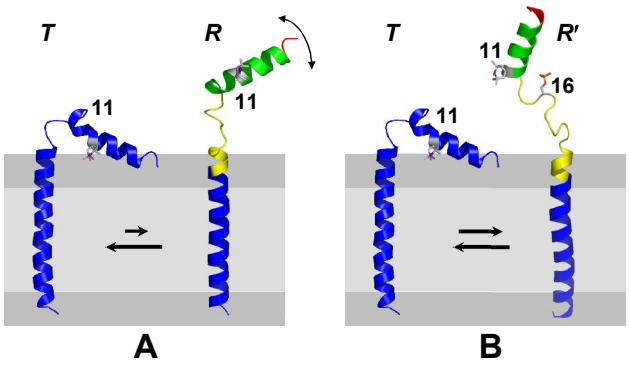

Figure 40: Two-state model for PLB conformational dynamics. (A) Unphosphorylated PLB is in equilibrium between ordered (*T*) and dynamically disordered (*R*) conformers. The disordered (extended) *R* form binds preferentially to SERCA but does not relieve inhibition. (B) Phosphorylation at Ser 16 disorders PLB further, shifting the equilibrium toward the disordered form (right), which itself is more dynamically disordered (hyperextended), and can thus bind to the relief site on SERCA, as depicted by the black spot on SERCA in **Figure 37**B. Structures are from solution NMR of un-[47] and phosphorylated PLB [59]. The disordered forms (right) are colored spectrally to indicate backbone dynamics, increasing from blue to yellow to green to red.

state is required to make the proper contact with SERCA to reverse the inhibitory interaction in the transmembrane domain, as illustrated in .

At first glance, it is surprising that CD data indicates a negligible effect of phosphorylation on helicity (-3 ± 5%) for isolated PLB, while both EPR and NMR indicate a substantial decrease in helical order. However, both EPR and NMR indicate that the portion of PLB that takes part in the order-to-disorder transition is small. NMR and EPR data together suggest that the affected region extends approximately from residue 10 to 27 [50, 51, 59]. Of these 18 residues, 13 are helical in the proposed *T* state. Thus, even if we assume that all 13 of these residues shift from helix to coil in the *T* to *R* transition, the predicted change in helicity over the entire PLB would be -13/52 = -25%. The EPR observation is that the labeled site increases its fraction disordered by 19 ± 5% upon phosphorylation (Figure 39). If this corresponds to the magnitude of the *R*-to-*T* transition induced by phosphorylation, it predicts a change in helicity by -4%, which is well within the range of values consistent with the CD measurement (-3 ± 5%).

A phosphorylation-induced change in structural dynamics of SERCA-bound PLB relieves inhibition.

Figure 41 illustrates a model, elaborating on the illustrations in Figure 37 and Figure 40, consistent with the EPR data in the present study and the NMR data in the related paper [149]. PLB is in a dynamic equilibrium between ordered (*T*)

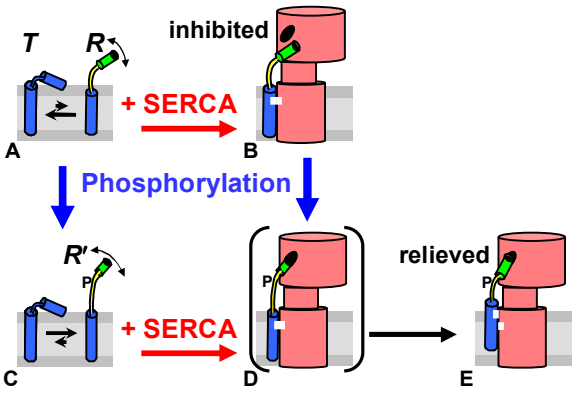

Figure 41: Schematic structural model for the mechanism of SERCA inhibition and relief by PLB.

and dynamically disordered (*R*) structural states (Figure 41A). SERCA binds preferentially to the *R* state of PLB in both the absence (Figure 41B) and presence (Figure 41D) of phosphorylation. In the absence of phosphorylation (Figure 41B), PLB is not sufficiently extended to reach the relief site on SERCA (depicted as a black target zone on SERCA) so SERCA remains inhibited due to interactions between specific portions of the two transmembrane domains (highlighted in white in Figure 41). In contrast, the hyperextended form of pPLB (Figure 41C) does reach the relief site on SERCA, transiently forming the collision complex of Figure 41D. SERCA binding then reduces the dynamics of phosphorylated PLB (as shown in Figure 37 and Figure 39), resulting in a less extended, more ordered form, which could cause the loss of SERCA inhibition by displacing the inhibitory transmembrane interactions between PLB and SERCA, as illustrated by the separation of white zones in Figure 41E.

Lipid anchor prevents reversal of inhibition by blocking formation of disordered state of PLB

The N-terminal lipid stabilizes the ordered *T* state of PLB and prevents the formation of the disordered (extended) *R* state (Figure 38B-E), but does not prevent inhibition by PLB (Figure 38A), showing that inhibition does not require an interaction between the extended form of PLB and the SERCA cytoplasmic domain. However, the anchor does prevent reversal of inhibition due to phosphorylation (Figure 38A), probably because it blocks formation of the dynamically disordered (hyperextended) R' form of the PLB cytoplasmic domain, which reverses SERCA inhibition by contacting a specific relief site on the SERCA cytoplasmic domain (Figure 41). This provides strong support for the importance of the dynamically disordered form of PLB in reversal of SERCA inhibition.

Relationship to NMR study

This study is closely related to a parallel study in which NMR was used to detect the effects of phosphorylation on the PLB-SERCA interaction [149]. These two studies yield consistent results and are quite complementary to each other. Like the present EPR study, the NMR study observes spectroscopic signals from the peptide backbone of monomeric PLB, and inhibition of SERCA was shown to be relieved by Ca^{2+} or phosphorylation under NMR conditions. While the present study is limited to a single labeled site, the NMR study reports information from every residue of PLB. Unlike the present study in lipid membranes, the NMR study was performed in detergent micelles, as required to obtain high-resolution data. While NMR can only observe directly the signal from free (unbound) PLB and the signals are only indirectly related to peptide dynamics, EPR detects both free and bound components with equal sensitivity and reports directly on rotational dynamics of the backbone. Taken together, the EPR and NMR results show that a large portion of the cytoplasmic domain of PLB undergoes a disorder-to-order transition upon phosphorylation, and that phosphorylation changes the structural dynamics of PLB without dissociating the two proteins. NMR data also suggests that phosphorylation increases the cooperativity of the SERCA-PLB interaction, supporting a cooperative allosteric model for this regulatory system.

Conclusion

EPR spectroscopy of a TOAC spin label attached rigidly to the peptide backbone at position 11 in the cytoplasmic domain of PLB shows that PLB phosphorylation at Ser 16 induces an order-to-disorder (*T* to *R*) transition in the cytoplasmic domain of PLB, and it

is this dynamically disordered (hyperextended) *R* structural state that rises above the membrane surface and binds to the SERCA cytoplasmic domain in a conformation that relieves SERCA inhibition. An N-terminal lipid anchor, which prevents the cytoplasmic domain of PLB from rising above the membrane surface and abolishes the dynamically disordered structural state, inhibits PLB normally but prevents the relief of inhibition by phosphorylation. Micromolar [Ca^{2+}] reverses PLB-dependent inhibition without a detectable change in cytoplasmic domain dynamics and without the need for the PLB cytoplasmic domain to rise above the membrane surface. Thus it is clear that neither Ca^{2+} nor PLB phosphorylation acts by dissociating PLB from SERCA, and that Ca^{2+} and PLB phosphorylation relieve SERCA inhibition by distinct mechanisms.

Materials and Methods

Synthesis of TOAC-labeled PLB

Figure 35 (bottom) shows the sequence of the synthesized monomeric AFA-PLB peptide that incorporates the spin-labeled amino acid 2,2,6,6-tetramethylpiperidine-1-oxyl-4-amino-4-carboxylic acid (TOAC) at position 11. The solid-phase synthesis and characterization of this peptide were reported previously [49, 51, 54, 150]. In order to obtain a derivative of spin-labeled PLB that has its N-terminus anchored in the lipid bilayer, Dialkyl 1', 3'-dioctadecyl-N-succinyl-L-glutamate (lipid tail) was linked to 11-TOAC-AFA-PLB through the N-terminal amino group . The synthesis of novel dialkyl chain amphiphiles containing peptides and its application on PLB was supported previously [51, 151].

Phosphorylation at Ser16 was accomplished either by incorporation as Fmoc-Ser[PO(OBzl)OH] (Novabiochem, San Diego, CA) during peptide synthesis or by cAMP-dependent protein kinase (PKA) [59] after reconstitution [152], with essentially the same results, both on inhibitory function and on EPR. Phosphorylation by PKA was greater than 80% complete, as determined using anti-PLB antibody (1D11), and the anti-phosphoserine PLB (285) antibody [153] on western blots.

Chemical and functional analysis

Mass spectrometry (MALDI-TOF), Edman protein sequencing, amino acid analysis, circular dichroism [54], inhibitory function [51], and EPR spectroscopy were used to establish the high purity and functional integrity of the spin-labeled peptides. Each PLB derivative was co-reconstituted in lipid bilayer membranes (DOPC/DOPE 4:1) with purified SERCA at molar ratios of 10 PLB/SERCA and 700 lipids/SERCA [147, 152], and the Ca-dependence of ATPase activity was measured at 25 °C [150]. The initial ATPase rate V was measured as a function of pCa (calculated as described previously [154]), and the data were fit by the Hill equation,

$$V = V_{max}/[1 + 10^{n\,(pKCa - pCa)}] \qquad \textbf{Equation 22}$$

to determine V_{max} , pKCa (the pCa value when $V = V_{max}/2$), and n (Hill coefficient). V_{max} was obtained from the fit, and the data were plotted as V/V_{max}.*vs* p*Ca*. The main goal was to determine the shift in pKCa caused by PLB.

EPR Spectroscopy

For EPR experiments, TOAC-PLB was reconstituted into lipid vesicles containing DOPC/DOPE (4:1, 200 lipids per PLB) in the presence and absence of excess SERCA [55]. Measurements were conducted in low Ca (pCa 6.5) buffer (50mM KCl, 5mM $MgCl_2$, 0.5mM EGTA, 210□M $CaCl_2$, 50mM MOPS, pH 7.0), where the inhibitory effect of PLB was maximal, and high Ca (pCa 5.0) buffer (same as low Ca, except 489μM $CaCl_2$), where the inhibitory effect of PLB was negligible [15]. The concentration of SERCA was twice that of TOAC-PLB, such that further increase had no effect on EPR spectra. The concentration of TOAC-PLB was determined by amino acid analysis and SERCA concentration by the Lowry method [155].

EPR spectra (Figure 37, Figure 38) were acquired using a Bruker EleXsys 500 spectrometer with the SHQ cavity. Samples (20 μL in a 0.6 mm i.d. quartz capillary) were maintained at 4ºC using the Bruker temperature controller with a quartz dewar insert. The field modulation frequency was 100 kHz, with a peak-to-peak amplitude of 1 G. The microwave power was 12.6 mW, producing moderate saturation (so that signal intensity was at least 50% of maximum) without significant effect on the spectral lineshape.

EPR spectra were calculated as a sum of one or two components, each component produced by a population having a static isotropic distribution of membrane orientations and undergoing rotational diffusion in a restricting potential (defined by order parameter S) with a single rotational correlation time (τ_R). Components were simulated with NLSL [156] on an IBM SP; the MOMD model was used, and the NLSL parameters $\bar{R}$ (diffusion rate) and C_{20} (first ordering potential parameter) were set to produce the desired τ_R and S.

Magnetic tensors were determined from spectra obtained at -60 °C. Lorentzian linewidths of 1 G and 2 G were used for narrow and broad spectral components, respectively. Experimental spectra were fit by summing simulated components. Error estimates for τ_R and S (Figure 39) were determined from the range of input values of these parameters for which the spectral splittings and linewidths were within experimental uncertainty of observed values. Angular amplitudes of motion were estimated from the expression $\theta_c = \cos^{-1}[0.5(1+8S)^{1/2} - 0.5]$, where θ_c is the radius of the cone that limits the motion.

Acknowledgements

This work was supported by grants to DDT (NIH GM27906) and CBK (AHA 9930083N). Supercomputer time was provided by the Minnesota Supercomputing Institute. We thank Razvan Cornea, Gianluigi Veglia and Nathaniel Traaseth for insightful discussions, Deborah Winters for assistance in molecular modeling and graphics, Yuri Nesmelov for assistance with EPR spectroscopy, Florentin Nitu for technical assistance, Nathan Lockwood for providing the lipid anchor, Thomas Krick for assistance with mass spectrometry, Jinny Johnson and Lawrence Dangott (Protein Chemistry Laboratory, Texas A&M University) for amino acid analysis.

Oligomeric Interactions in Cardiac Calcium Transport Regulation Probed by Electron Paramagnetic Resonance

Kurt D. Torgersen, Christine B. Karim, Edmund Howard, Jesse E. McCaffrey

and David D. Thomas*

Department of Biochemistry, Molecular Biology and Biophysics, University of Minnesota Medical School, Minneapolis, Minnesota 55455

To be submitted to the Journal of Molecular Biology

This work was supported in part by a grant to DDT (NIH GM27906). KDT was supported by a predoctoral fellowship from the American Heart Association (Midwest Affiliate).

*To whom correspondence should be addressed: ddt@umn.edu.

‡University of Minnesota Medical School

Keywords: SERCA, Ca-ATPase, phospholamban, saturation transfer

Running Title: Oligomeric interactions in cardiac calcium transport regulation

ABBREVIATIONS

[1]Abbreviations: $C_{12}E_8$, octaethyleneglycol monododecyl ether; Ca, divalent calcium ion (Ca^{2+}); DOPC, dioleoyl phosphatidyl-choline; DOPE, dioleoyl phosphatidylethanolamine; EGTA, ethyleneglycol-bis-(β-aminoethyl ether)N,N,N',N'-tetraacetic acid; Fmoc, 9-fluorenylmethyloxycarbonyl; MOPS, 3-(*N*-morpholino)propanesulfonic acid; pCa, -log[Ca^{2+}]; PKA, protein kinase A; pK_{Ca}, -log(K_{Ca}), calcium concentration at half-maximal ATPase activity; PLB, phospholamban; SERCA, Sarco-endoplasmic reticulum Ca-ATPase; SR, sarcoplasmic reticulum; WT, wild-type; EPR, Electron Paramagnetic Resonance; STEPR, Saturation Transfer EPR; TOAC, 2,2,6,6-tetramethylpiperidine-1-oxyl-4-amino-4-carboxylic acid.

We have used peptide synthesis, functional co-reconstitution, and electron paramagnetic resonance (EPR) spectroscopy to probe the structural dynamics of phospholamban (PLB) and its regulatory target, the sarcoplasmic reticulum Ca-ATPase (SERCA), focusing on oligomeric interactions. A monomeric PLB mutant, AFA-PLB, was synthesized with the amino acid spin label TOAC at position 36 in the transmembrane domain and reconstituted into DOPC/DOPE vesicles in the presence and absence of SERCA, with and without phosphorylation of PLB at Ser16. Unlike conventional spin labels, TOAC is directly coupled to the peptide backbone, allowing quantitative measurements of peptide backbone dynamics. Calcium-dependent ATPase assays showed that TOAC-labeled AFA-PLB had the same inhibition and phosphorylation-dependent relief of inhibition as the unlabeled protein. Conventional EPR dynamics report a single, highly restricted component, consistent with a stable helix at position 36 in the transmembrane domain reported by NMR experiments. Order parameter calculations and linewidth measurements suggest that phosphorylation of PLB in the absence of SERCA induces PLB oligomerization and that phosphorylated PLB remains bound to active SERCA. These conclusions are supported more directly and clearly by saturation transfer EPR (STEPR), which measures microsecond rotational dynamics of PLB, and dipolar EPR, which measures PLB-PLB interactions. These data support a proposed model in which the PLB monomer binds to and inhibits SERCA, and phosphorylation of PLB stabilizes PLB oligomers but does not dissociate PLB from SERCA.

Introduction

Muscle contraction and relaxation are controlled by calcium flux within the muscle cell. Muscle contraction is initiated after calcium is released from the sarcoplasmic reticulum (SR) by the ryanodine receptors, raising cytoplasmic calcium concentration to micromolar levels . In order for muscular relaxation, calcium must be sequestered back into the SR [157]. The sarco(endo)plasmic reticulum calcium ATP-ase (SERCA) is a P-type ATPase embedded in the SR membrane which pumps two calcium ions into the SR at the expense of one ATP molecule to facilitate muscular relaxation [1-3]. In cardiac muscle, the activity of SERCA is regulated by phospholamban (PLB), a 52 residue integral membrane protein [5]. PLB binds to SERCA and decreases the apparent calcium affinity, effectively decreasing SERCA activity [5]. PLB phosphorylation at Ser16 and/or Thr17 following *B*-adrenergic stimulation has been shown to restore SERCA activity [5, 158, 159]. In addition to PLB phosphorylation, micromolar calcium concentration levels in the cytoplasm also act to relieve PLB inhibition of SERCA activity [15].

PLB exists in a dynamic equilibrium between monomeric and pentameric species but data shows that the PLB monomer is the primary regulator of SERCA activity [6-8]. Cryo-EM data [66] and a recently published PLB pentamer structure [63] propose a model in which the PLB pentamer binds to SERCA, however the general consensus of opinion is that the PLB pentamer functions as a storage form rather than a regulator of SERCA activity [6, 140, 160]. We recently published a paper using both EPR and NMR in DPC micelles and lipid bilayers showing that, like the monomer, the pentamer adopts a L-shaped structure in which the cytoplasmic domains strongly interact with the bilayer

surface [65]. Previous studies using various types of spectroscopy or gel electrophoresis have shown that phosphorylation of PLB induces oligomerization [8, 60].

A fully functional monomeric PLB mutant, AFA-PLB, has been synthesized by replacing the three transmembrane Cys residues with Ala, Phe and Ala [48, 49]. A high resolution NMR structure of AFA-PLB resolving both secondary structure and topology in lipid bilayers shows an amphipathic cytoplasmic helix (residues 1-16) connected to the C-terminal helix (residues 22-52) by a flexible loop [52]. The transmembrane helix is nearly collinear with the membrane normal, while the cytoplasmic helix is almost perpendicular to the membrane normal and strongly interacting with the lipid bilayer surface. EPR data using a unique amino acid spin label, TOAC, which directly reports the peptide backbone dynamics show that while the transmembrane helix adopts a single conformation, the cytoplasmic helix is in an equilibrium between an ordered T-state and a dynamically disordered R-state [17, 51, 161]. Additional biochemical and biophysical data have lead to the hypothesis that the TM domain of PLB is responsible for SERCA inhibition, but the PLB cytoplasmic domain, specifically the R-state, is necessary for phosphorylation induced inhibition relief [17, 54, 162-166].

Data from mutagenesis and cross-linking experiments propose that both the phosphorylation and calcium induced inhibition relief require complete dissociation of the SERCA-PLB complex [7, 11-14]. However, fluorescence, EPR and NMR data from fully functional reconstituted systems show that PLB is still bound to SERCA following phosphorylation or micromolar calcium concentration (Figure 42) [15-19]. Here, we use a fully functional monomeric mutant labeled at residue 36 with the TOAC spin label to show the effects of SERCA binding and phosphorylation on PLB dynamics and to determine if phosphorylation of PLB at Ser16 dissociates the SERCA-PLB complex.

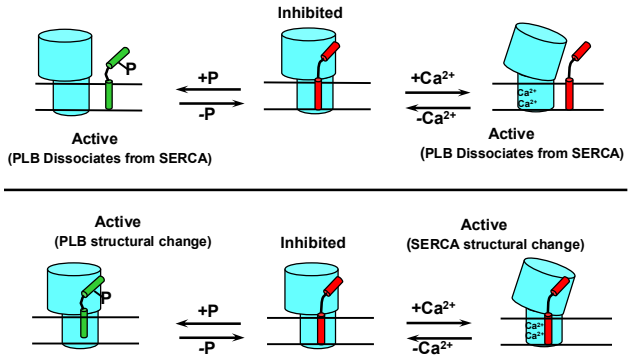

Figure 42. Proposed models of phosphorylation and calcium induced inhibition relief. Top: PLB phosphorylation (left) or micromolar Ca^{2+} (right) dissociates PLB from SERCA, relieving inhibition. Bottom: PLB phosphorylation induces a structural change in PLB and micromolar Ca^{2+} induces a structural change in SERCA; both relieve inhibition without dissociating the SERCA-PLB complex.

Materials and Methods

PLB Synthesis and Co-Reconstitution. PLB derivatives were synthesized using Fmoc solid-phase peptide synthesis as previously described [17, 51, 125]. Briefly, the peptide was synthesized using a PE Biosystems PioneerTM peptide synthesis system, cleaved from the support resin and purified using reverse-phase HPCL. After purification, the peptide was lyophilized and finally dissolved in methanol in preparation for reconstitution into proteoliposomes .

SERCA was purified from fast-twitch skeletal muscle of New Zealand white rabbits as previously described [44] and co-reconstituted with PLB using previously established methods [147, 152, 167]. PLB in a methanol stock solution was added to DOPE and DOPE lipids dissolved in chloroform. Organic solvents were removed under a high vacuum. PLB was then hydrated with a solution containing 5mM $MgCl_2$, 0.1M KCl, 10% glycerol, 20mM MOPS, pH 7.0, vortexed and briefly sonicated to form unilamellar vesicles. Following vesicle formation, the detergent, $C_{12}E_8$, was added (2 mg/mg lipid) prior to SERCA addition. Phosphorylation was accomplished by the addition of the catalytic subunit of PKA and ATP prior to SERCA addition. PLB phosphorylation was quantified using the fluorescent dyes Pro-Q Diamond and SYPRO Ruby [168] and synthetic phosphorylated PLB standards. Detergent was removed by the addition of Biobeads SM2 (25mg/mg $C_{12}E_8$) and the samples were stirred at 25 °C for three hours.

Functional Assays. PLB derivatives were individually co-reconstituted with purified SERCA in DOPC/DOPE lipid bilayers (4/1, mol/mol) at molar ratios of 10 SERCA/PLB and 700 lipids/SERCA [147, 152]. The initial ATPase rate (V) was measured as a function of calcium concentration at 25°C and the data were fit to the Hill equation:

$$V = V_{max}/[1+ 10^{-n}(pK_{Ca} - p_{Ca})] \qquad \textbf{Equation 23}$$

to determine V_{max}, pK_{Ca} (the p_{Ca} value where $V = V_{max}/2$) and n (Hill coefficient) [150, 154]. The data were then normalized to V_{max} and plotted as a function of p_{Ca} to show the effect of PLB and phosphorylation on SERCA activity.

EPR Spectroscopy. EPR samples consisted of TOAC-PLB, reconstituted in lipid vesicles consisting of a 4/1 molar ratio of DOPC/DOPE (200 lipids/PLB) in the presence or absence of 2 molar excess SERCA [17, 55]. Proteoliposomes were suspended in a low calcium (*pCa* 6.5) solution consisting of 50mM KCl, 5mM $MgCl_2$, 0.5mM EGTA, 210 μM $CaCl_2$, 50mM MOPS (pH 7.0). Typical [PLB] was 400μM. PLB concentration was confirmed by amino acid analysis and SERCA concentration was confirmed by the bicinchoninic acid assay.

EPR experiments were performed on a Bruker EleXsys E500 spectrometer at X-band (9.4 GHz) with the SHQ cavity (ER4122 ST). Samples, typically 5 μL, were loaded into a Wilmad quartz capillary (0.6 mm i.d., 0.8 mm o.d.), sealed with Critoseal and centered in the cavity. Samples were maintained at 4°C, except dipolar broadening experiments which were performed at 200K, using a Bruker temperature controller equipped with a quartz dewar insert. Spectra were recorded over a 120 G scan width with 1024 points, unless otherwise noted.

Conventional (first harmonic absorption in-phase V_1) spectra were recorded with 100 kHz field modulation, a peak-to-peak modulation amplitude H_m = 3.0 G and a microwave field amplitude H_1 = 0.14 G to reduce modulation and saturation effects on lineshape. Spectra were analyzed by measuring the outer splitting ($2T_{II}'$) and the outer half-width at half-height of the low field line (Γ_L). The splitting values were compared to the rigid limit splitting value ($2T_{II}$) obtained from a sample at 170K and the rapid limit value (T_0) typical of a nitroxide undergoing isotropic rotational diffusion in an aqueous solution. The order parameter (S) was calculated using the following equation [87]:

$$S = [2T_{II}' - 2T_0]/[2T_{II} - 2T_0] \quad \textbf{Equation 24}$$

STEPR (second harmonic out-of-phase V_2') spectra were recorded as previously described [169, 170] with 50 k H_m = 5.0 G and H_1 = 0.25 G. In order to accurately and reproducibly set H_1, the SHQ cavity was calibrated with a solution of peroxylamine disulfonate [169]. STEPR (V_2') spectra were analyzed by measuring the ratio L''/L to determine the rotational correlation time τ_R. L'' is defined as the height of the spectrum above the baseline 10 G upfield of L [169]. The L''/L ratio was then compared to a model system to determine the rotational correlation time [88].

Dipolar EPR experiments were performed at 200K to ensure any lineshape changes were due to dipolar broadening and not rotational motion [171]. Samples were flash frozen in liquid N_2 and centered in a 200K quartz dewar. Spectra were recorded with 0.20 mW of power and a peak-to-peak modulation amplitude of H_m = 1.0 G to avoid lineshape broadening due to overmodulation or power saturation [171]. The scan width was increased to 200 G to detect broadening in the spectral wings. Dipolar EPR spectra were analyzed using the WACY program (developed in-house by E. Howard) to determine the distance distribution. Dipolar broadening of a non-interacting spectrum (unphosphorylated PLB) was simulated from Gaussian distance distributions convoluted by a Pake function [90]. The simulated spectra were fit to experimental spectra and the quality of the fits were assessed by the residual plots and the residual sum of squares.

Results

Activity Assays.

We quantified the inhibition of SERCA by measuring the shift in pK_{Ca} (the pCa value for 50% activity). Previous data have shown that AFA-PLB has the same inhibitory function as WT-PLB and phosphorylation reverses WT-PLB inhibition while significantly reducing AFA-PLB inhibition [49, 51, 147]. Here we show that the inhibition of 36-TOAC-AFA-PLB (pK_{Ca} = 0.65 ± 0.05) is identical to AFA-PLB (pK_{Ca} = 0.65 ± 0.03) and the effect of phosphorylation is also identical for both 36-TOAC-AFA-PLB (pK_{Ca} = 0.33 ± 0.03) and AFA-PLB (pK_{Ca} = 0.34 ± 0.03) (Figure 43).

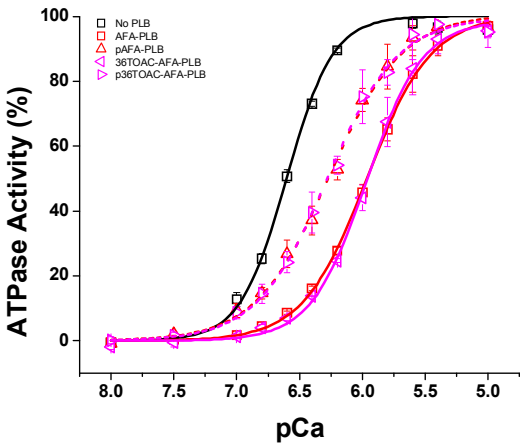

Figure 43 PLB inhibition of SERCA. Each data set (n=3) was fit to Equation 23 and plotted as V/V_{max}.

Conventional EPR at 4 °C: Dynamics of the PLB backbone

We have shown that the TOAC spin label reports directly the dynamics of the PLB backbone and that TOAC at position 11 resolves two conformational states of the PLB cytoplasmic domain, including a minor population in which the spin label becomes dynamically disordered

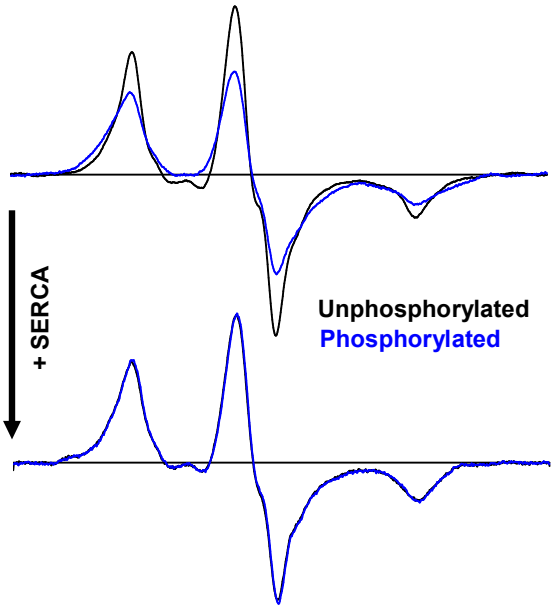

Figure 44. Effect of SERCA binding and phosphorylation on conventional EPR spectra. Top: reconstituted PLB. Bottom: PLB co-reconstituted with SERCA (2 SERCA/PLB mol/mol). Black: unphosphorylated PLB. Blue: phosphorylated PLB. Spectra were recorded at 4°C with a 120 G scan width and normalized to the double integral.

on the ns time scale, indicating local unfolding [17, 51, 65, 161]. The dynamics and mol fractions of these two states are affected by both phosphorylation and SERCA binding [17]. Figure 44 shows that TOAC at position 36, in the transmembrane domain of AFA-PLB, has the lineshape characteristic of a strongly immobilized spin label, undergoing little or no ns rotational dynamics.

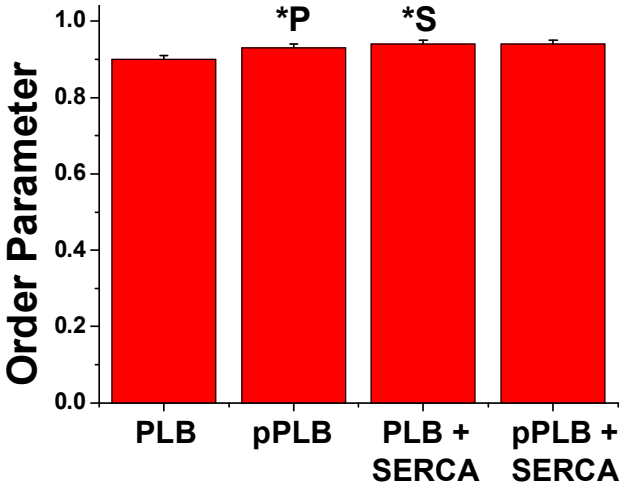

Figure 45. Order parameters derived from conventional EPR spectra (Figure 44). The order parameter was calculated using Equation 24. Values and error bars reflect the mean and SEM with n = 4. Significant changes due to phosphorylation and SERCA binding are indicated by "*P" and "*S", respectively.

Thus, in the vicinity of position 36 in the TM domain, there is a single conformation, corresponding to a highly ordered helix, regardless of phosphorylation or SERCA binding, consistent with other NMR and EPR data on the dynamics of the TM domain [18, 47, 50-52, 59, 161]. While all spectra are near the rigid limit, indicating very little ns rotational motion, both phosphorylation and SERCA binding restrict significantly the transmembrane helix rotational motion (Figure 45, *): phosphorylation increases the order parameter from 0.90 $\pm$ 0.01 to 0.93 $\pm$ 0.01, and SERCA increases the order parameter of unbound PLB from 0.90 $\pm$ 0.01 to 0.94 $\pm$ 0.01. However phosphorylation of SERCA-bound PLB does not affect the order parameter (Figure 45, right) in comparison to pPLB or SERCA-bound PLB.

The only obvious effect in Figure 44 is the increased linewidth due to phosphorylation of isolated PLB (Figure 44, top left). The outer half-width at half-height

of the low-field EPR line (Γ_L) increased from 3.46 $\pm$ 0.25 G to 5.17 $\pm$ 0.09 G. In principle, this linewidth increase could be due to an increase in nanosecond rotational motion, but this is not consistent with the restriction decrease in mobility indicated by the increased order parameter (Figure 45, *P). Therefore, the line broadening must be caused by dipolar broadening due to the proximity of other spin labels [172]. In order to examine this spin-spin interaction quantitatively, we recorded EPR spectra on frozen samples, thus eliminating rotational mobility as a variable.

Conventional EPR at 200^{o}K: PLB Oligomeric Interactions

EPR spectra were recorded on the same samples as in (Figure 45), except that the temperature was 200K (Figure 46). Only the pPLB spectrum in the absence of SERCA showed significant line broadening and signal intensity attenuation, which must be due to spin-spin dipolar interactions (Figure 46). Analysis of this spectrum, correcting for the fraction of unlabeled PLB, revealed that virtually all PLB molecules were in a dimeric complex, in which the interspin distance was 1.39 ± 0.11 nm, and the best-fit Gaussian distribution had a FWHM = 0.76 ± 0.12 nm (Figure 47).

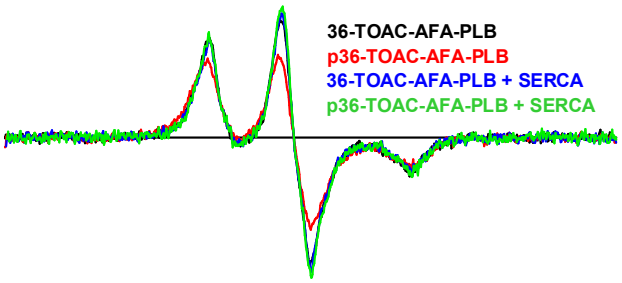

Figure 46. **Dipolar broadening due to spin-spin interaction**. Conventional EPR spectra were acquired at 200K with a 200 G scan width, from the same samples as in Figure 45.

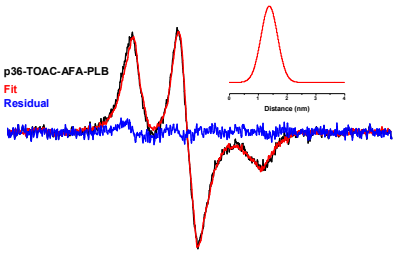

Figure 47. Interprobe distance distributions determined from dipolar broadening. Spectra of pPLB alone (Figure 46, red) Plots showing the dipolar broadened pPLB spectrum (black), the best fit (red) and the residual (blue). The distance distribution from the best fit is shown in the inset.

STEPR: Microsecond Dynamics

Conventional EPR spectra are sensitive only to rotational motions on the picosecond to nanosecond timescale (Figure 48, left). Spectra of 36-TOAC-PLB (Figure 44) show little or no motion on this time scale, indicating the lack of significant peptide backbone flexibility. It is likely that both PLB and SERCA undergo global (rigid-body) motions in the membrane, but even a fluid lipid bilayer is at least 100 times more viscous than water, so global motions of membrane proteins are expected to occur in the μs time scale, where only saturation transfer EPR is sensitive to rotational motion (Figure 48, right).

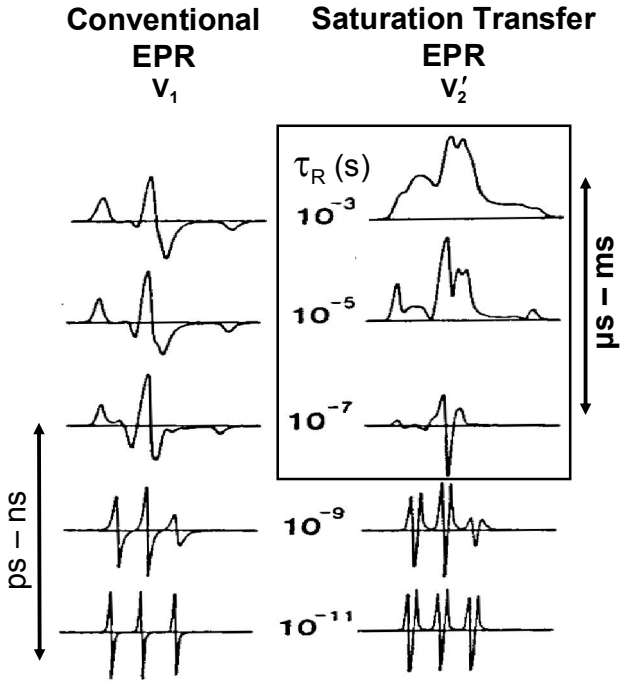

Figure 48. Rotational correlation time effects on conventional (V_1, *left*) and saturation transfer (V_2', *right*) EPR spectra [88].

STEPR experiments were performed on the same samples shown in Figure 44. While the conventional EPR spectra showed only slight

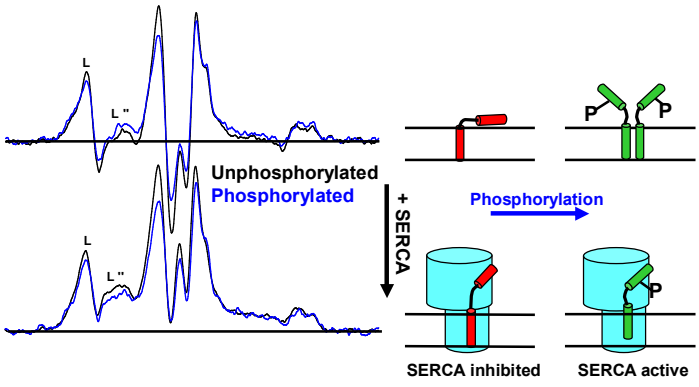

Figure 49. Phosphorylation and SERCA binding effects on PLB microsecond dynamics. Spectra were recorded at 4°C with a 120 G scan width and normalized to H_1 and the double integral of the V_1 corresponding spectrum.

effects of phosphorylation and SERCA binding Figure 44, STEPR spectra showed substantial effects (Figure 49). Peak-height ratios (L″/L) were measured to estimate rotational correlation times. PLB alone has the shortest correlation time of 6 ± 2 μs, near the rapid limit of the STEPR time scale. PLB phosphorylation leads to about a four fold increase in rotational correlation time, to 25 ± 5 μs, consistent with oligomer formation. SERCA binding further decreased the rotational correlation time to 60 ± 7 μs, in agreement with the measured correlation time of spin labeled SERCA alone [173]. Most importantly, phosphorylation of SERCA-bound PLB had no significant effect on the rotational correlation (55 ± 5 μs). This motion is at least twice as slow as for pPLB in the absence of SERCA, showing directly that phosphorylated PLB remains bound to active SERCA.

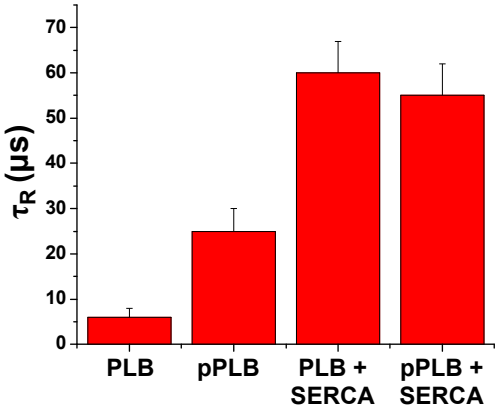

Figure 50. Rotational correlation times of PLB as a function of phosphorylation and SERCA binding. τ_R values from STEPR spectra estimated from an empirical plot in [88]. Values and error bars reflect the mean and SEM with n = 4.

Discussion

Summary of Results. We have synthesized a fully functional (Figure 43) monomeric mutant of PLB (AFA-PLB) labeled with the amino acid spin label TOAC at position 36 in the transmembrane domain, in order to test distinct models for phosphorylation-dependent inhibition of SERCA (Figure 42). Spectroscopic and functional data show directly that monomeric PLB binds to and inhibits SERCA at sub-micromolar [Ca^{2+}] and that phosphorylation of PLB relieves SERCA inhibition without

significant dissociation of the SERCA-PLB complex. Phosphorylation of unbound PLB induces peptide oligomerization (probably forming a dimer of AFA-PLB), but that SERCA dissociates these oligomers, presumably due to its preferential binding to the monomer.

Phosphorylation of unbound PLB induces peptide oligomerization. The conventional dynamics data of both PLB and pPLB labeled with TOAC at position 36 in the TM domain report order parameters near the rigid limit consistent with a stable, well ordered helix reported previously by EPR and NMR data [18, 47, 50-52, 59, 161]. Phosphorylation increases the order parameter from 0.90 $\pm$ 0.01 to 0.93 $\pm$ 0.01 (Figure 45) indicating that the amplitude of peptide backbone motion is further restricted. This phosphorylation-dependent decrease in backbone dynamics could be a result of increased helix rigidity or tertiary contacts due to oligomerization. Previously published NMR data of AFA-PLB in DPC micelles shows that phosphorylation at S16 slightly increases the dynamics of the TM domain [59]. STEPR data (Figure 49) shows that phosphorylation of unbound PLB increases the correlation time from 6 μs to 25 μs, a four-fold increase. This significant increase in microsecond dynamics could not result from a slight reduction in nanosecond peptide backbone dynamics but from decreased rotational correlation time of a pPLB oligomer. It is possible that increased interaction between the cytoplasmic domain and the lipid bilayer due to phosphorylation could increase the correlation time of monomeric PLB, but a significant amount of data indicate that phosphorylation of PLB causes an order-to-disorder conformational change in the cytoplasmic domain [17, 18, 59] and decreases the interaction between the cytoplasmic domain and the lipid bilayer surface [69].

Although the conventional and STEPR dynamics data strongly indicate that phosphorylation of unbound PLB induces oligomerization, the dipolar data confirm the presence of pPLB oligomers (Figure 46 & Figure 47) due to phosphorylation. This is consistent with data from previous experiments in our lab [8]. Here, researchers used spin-labeled lipids and SDS-PAGE to show that phosphorylation increases both the mol fraction and oligomeric size of WT-PLB. In addition, the same studies on a monomeric mutant (L37A-PLB) conclude that the unphosphorylated form of L37A-PLB was primarily monomeric and that the phosphorylated form was primarily dimeric. Finally, *in-vivo* fluorescence experiments on phosphomimetic mutant PLB derivatives also showed that pseudophosphorylation induced oligomerization [174].

Phosphorylated PLB is still bound to active SERCA. We have previously reported that phosphorylation of SERCA bound PLB acts to relieve inhibition by inducing a structural change within PLB [17, 18] and that micromolar calcium concentration relieves inhibition by inducing a structural change within SERCA [15, 16] but neither mechanism results in the dissociation of the SERCA-PLB complex (Figure 42). Although the EPR and NMR data on peptide backbone and side chain dynamics agree and indirectly support the model that pPLB is still bound to active SERCA, the combination of conventional EPR and STEPR measuring both peptide backbone dynamics and rotational correlation times directly show that pPLB is still bound to active SERCA.

The conventional dynamics data of SERCA-bound PLB show the TM domain at position 36 undergoes very little ns motion. These data are consistent with a SERCA-PLB complex model proposing that the TM domain of PLB binds to SERCA in a groove

formed by helices M2, M4, M6 and M9 [74]. In this model, SERCA binds to an extended state of PLB in which the loop and domain 1b residues are unstructured, allowing the helical domain 1a to interact with cytoplasmic residues in SERCA nucleotide binding domain. Although domain 1b residues are unstructured, the model predicts that the peptide backbone at position 36 remains helical, consistent with the conventional dynamics reported here (Figure 44, Figure 45). Interestingly, the SERCA-PLB model proposing and extended PLB structure is consistent with EPR and NMR dynamics data showing that SERCA preferentially binds to an extended "R-state" of PLB [17] and that SERCA binding increases the helicity of the PLB TM domain at residue 36 [18, 75], again consistent with an increase in the order parameter reported here.

Conventional EPR data reported previously [17, 51, 161] and here are a measure of the peptide backbone dynamics while saturation transfer EPR is a measure of the rotational diffusion of PLB in the lipid bilayer and is a much more direct measurement of PLB binding to SERCA. Here we report that rotational correlation time of PLB is increased by a factor of ten upon the addition of SERCA a clear indicator of PLB binding to SERCA. Furthermore, the estimated rotational correlation time of PLB bound to SERCA is within 15% of the reported correlation time of SERCA in lipid bilayers [173]. Only a slight decrease in correlation time upon phosphorylation of PLB bound to SERCA directly shows that pPLB is still bound to active SERCA. This decrease in correlation time could be due to a structural rearrangement in the SERCA-PLB complex, reducing the cross-sectional area in the lipid bilayer and consequently decreasing the rotational correlation time of the complex.

Conclusions. We have performed conventional, saturation transfer and dipolar EPR experiments on a fully functional monomeric mutant of PLB labeled with TOAC at position 36 in the TM domain as a function of phosphorylation and SERCA binding. This is the first time saturation transfer EPR of PLB has been used to assess PLB binding to SERCA. Our results clearly show that monomeric PLB binds to and inhibits SERCA, phosphorylation of PLB in the absence of SERCA forms oligomers and that SERCA destabilizes the pPLB oligomers. Most importantly we have shown that phosphorylated PLB is still bound to active SERCA (Figure 51). This shows clearly that phosphorylation induced inhibition relief is not due to dissociation of the complex, but rather a structural change of the complex.

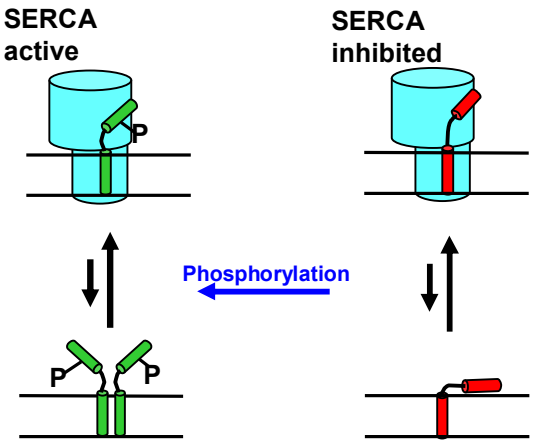

Figure 51. Oligomeric interactions between SERCA and PLB. Structural model consistent with the data shows that SERCA binds PLB and is inhibited. Phosphorylation of PLB in the absence of SERCA induces oligomerization and the addition of SERCA destabilizes the pPLB oligomer. Phosphorylation of SERCA bound PLB relieves inhibition without dissociating the SERCA-PLB complex.

Future studies. The data show clearly that monomeric PLB binds to and inhibits SERCA activity, consistent with previous reports that the PLB monomer is the primary regulator of SERCA activity and the pentamer is most likely a storage form of PLB. Although a model and cryo EM data have been generated proposing that the pentamer can bind to and inhibit SERCA [63, 66] , there has not been any direct evidence reported so far. Based on results shown here, it should be possible to directly determine if the PLB pentamer does bind to SERCA by co-reconstituting spin labeled SERCA with

monomeric or pentameric PLB and using STEPR to measure the rotational diffusion of the SERCA-PLB complex. As a control we measured the rotational correlation time of pentameric PLB labeled with TOAC at position 36 and determined it to be on the order of 200 μs while the rotational correlation time of monomeric PLB is 6 μs. Consequently, these data should be clear whether SERCA binds the PLB pentamer or destabilizes the pentamer and binds only the monomer as previously reported [6].

ACKNOWLEDGEMENTS

We thank Elizabeth Lockamy and Zach James for assistance and advice in SERCA purification and the phosphorylation quantitation assays. We thank Ryan Mello for assistance on STEPR experiments, and Octavian Cornea for assistance with manuscript preparation and publication. We thank Dr. Gianluigi Veglia for critical manuscript review.

CHAPTER 6. Future Directions

Although it is widely accepted that the PLB monomer is the active regulator of SERCA activity and the pentamer is merely a storage form, it has never been shown directly that SERCA does not bind pentameric PLB. The saturation transfer EPR results from chapter 5 show that the rotational correlation time of 36-TOAC-AFA-PLB co-reconstituted with SERCA is on the same order as spin-labeled SERCA but that the rotational correlation time of 36-WT-PLB is much slower than spin-labeled SERCA, probably due to the interaction between the PLB cytoplasmic domains and the lipid bilayer The correlation times of all three samples are several orders or magnitude faster than the rigid limit of saturation transfer EPR. Therefore it should be possible to compare the rotational correlation times of spin-labeled SERCA co-reconstituted with unlabeled AFA or WT PLB. If SERCA does indeed bind the PLB pentamer, the rotational correlation time spin-labeled SERCA co-reconstituted with the pentamer should be significantly slower than spin labeled SERCA co-reconstituted with monomeric PLB.

Data acquired during my thesis project clearly show that PLB phosphorylation does not dissociate the SERCA-PLB complex. This thesis work supports other work from the Thomas lab and the Veglia lab. Although the collaborative work between the two labs over the years clearly show that phosphorylated PLB is still bound to active SERCA, we have yet to determine how PLB phosphorylation relieves SERCA inhibition without dissociating the complex. To this end, I have been working on a project to test one hypothesis.

It has previously been shown that only the TM domain of PLB is necessary to inhibit SERCA and that the cytoplasmic domain is necessary to relieve inhibition. In fact, the cytoplasmic domain must be able to adopt the dynamically disordered R-state for phosphorylation dependent inhibition relief to occur. Data from our lab and others have shown that PLB phosphorylation at Ser16 induces an order-to-disorder conformational change in the absence of SERCA which increases both the mol fraction and dynamics of the R-state. However, when PLB is bound to SERCA, phosphorylation has the opposite effect, inducing a disorder-to-order conformational change. We have also shown that SERCA preferentially binds to the R-state, a conclusion supported by the SERCA-PLB complex models. Based on these data, we hypothesize that phosphorylation of SERCA bound PLB produces a transient dynamically disordered R-state which is able to interact and bind to sites on the cytoplasmic domain of SERCA. Subsequent to binding, the cytoplasmic domain of pPLB becomes more ordered which pulls the TM domain of PLB vertically out of the

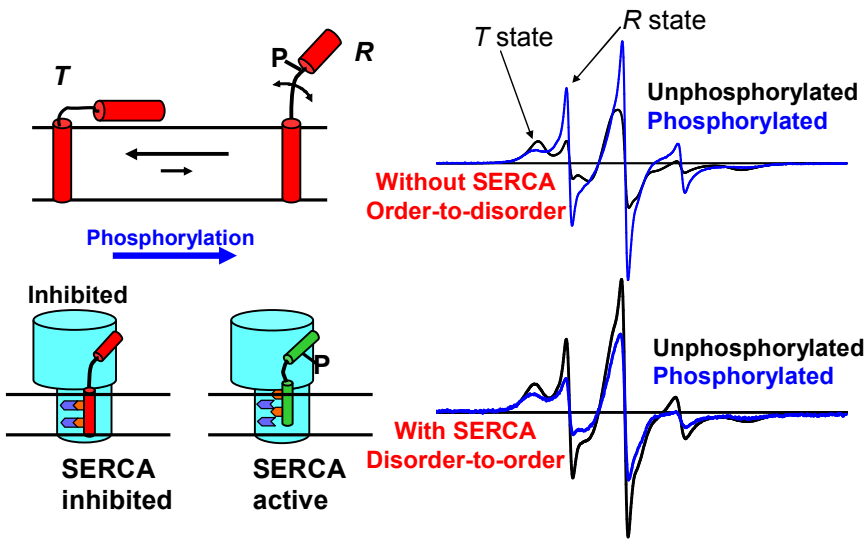

Figure 52. PLB structural changes as a function of phosphorylation and SERCA binding.

EPR spectra of PLB (black) and phosphorylated PLB (blue) in the absence of SERCA (top) and presence of SERCA (bottom) and corresponding cartoons representing structural models consistent with the data. In the absence of SERCA, PLB phosphorylation induces an order-to-disorder transition increasing the dynamics and mold fraction of the R state. In the presence of SERCA, PLB phosphorylation produces the opposite effects.

membrane, disrupting the TM domain inhibitory interactions and thereby activating SERCA without dissociating the complex (Figure 52).

I have begun testing this model by measuring the accessibility of spin labeled PLB to the lipid bilayer, bilayer interface and aqueous phase (Figure 53) using the saturation rollover curve method described in Chapter 2.5. Accessibility to the lipid bilayer the bilayer interface and the aqueous phase has been probed using O_2, DOGS-NTA-Ni and NiAA, respectively.

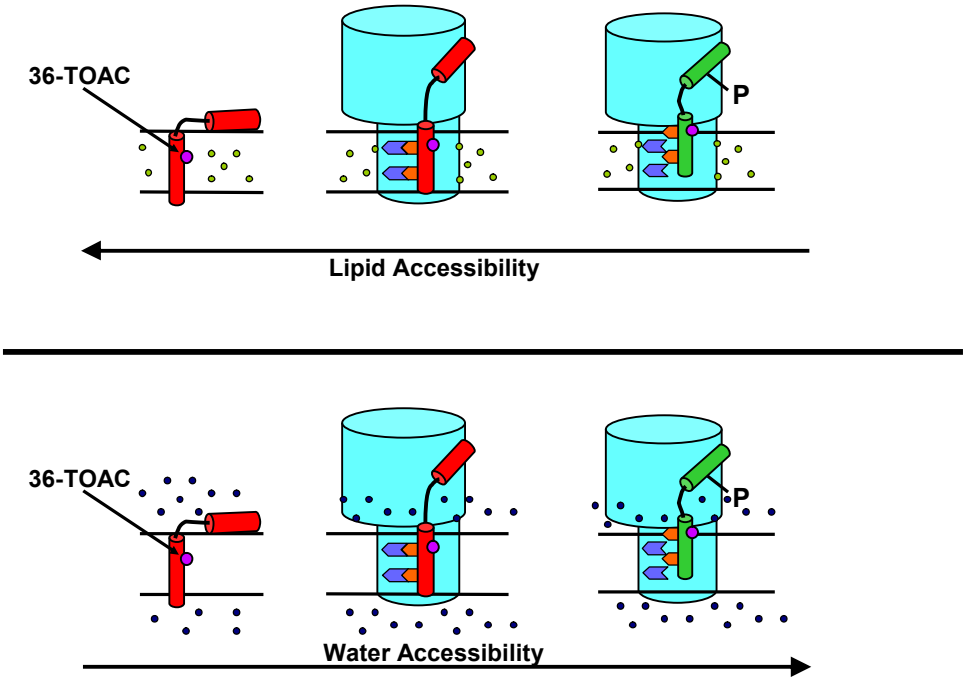

Figure 53. Predicted 36-TOAC accessibility changes

Top panel: The phosphorylation dependent inhibition relief model predicts that the accessibility of 36-TOAC-PLB to the lipid bilayer will decrease upon SERCA binding. This effect will be enhanced upon phosphorylation. Bottom panel: The model predicts that the accessibility of 36-TOAC-PLB to the aqueous phase will increase upon SERCA binding with a further increase upon phosphorylation.

I have created a model system of DOPC/DOPE vesicles doped with a small amount of commercially available spin labeled lipid to ensure that accessibility to the different PREs is dependent on the depth of the spin label in the bilayer. In order to ensure homogenous distribution of NiAA across the bilayer membrane, those specific samples were made with a buffer containing 20mM NiAA. Samples were loaded into a TPX (gas permeable teflon) capillary and inserted into a dielectric resonator at 25 °C. Lipid (O_2) accessibility was measured by passing zero-grade air over the samples during spectral acquisition while aqueous solvent (NiAA) and N_2 (no PRE control) accessibilities were measured by passing N_2 gas over the samples during spectral acquisition. $P_{1/2}$ and $\Delta P_{1/2}$ were determined as described in chapter 2.5 using Equation 13.

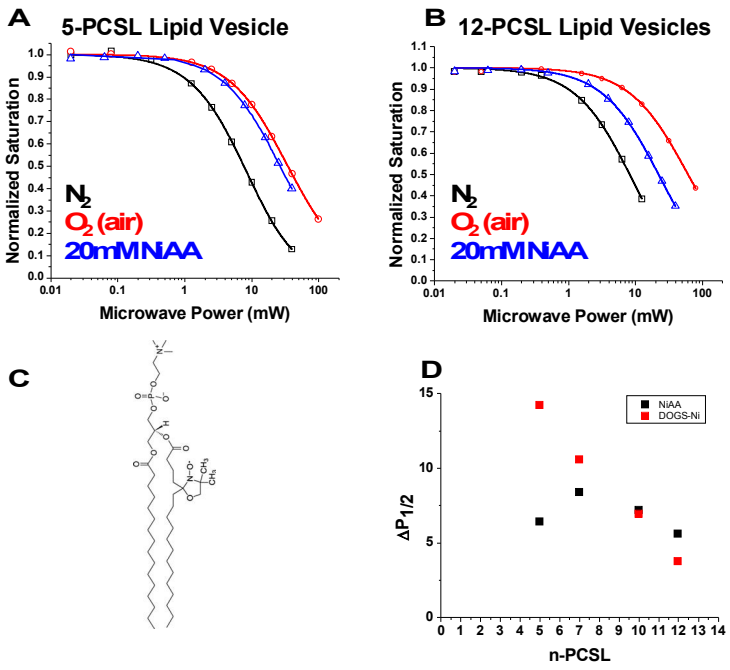

Figure 54. Spin labeled lipid accessibility measurements.

(A) Normalized saturation rollover curve measuring the accessibility of a lipid spin labeled at position five of the hydrocarbon chain to O_2 (red), 20mM NiAA (blue) and N_2 (black). The N_2 data set is the no PRE control used to calculate $\Delta P_{1/2}$. (B) Normalized saturation rollover curve of a lipid spin labeled at position 12 of the hydrocarbon chain. The color scheme is the same as in panel A. (C) Structure of the lipid spin labeled at position five. (D) Plot of $\Delta P_{1/2}$ as a function of spin label position for 20mM NiAA (black) and DOGS-NTA-Ni (red) showing that spin label depth in the membrane is more sensitive to DOGS-NTA-Ni.

Indeed, accessibility to different PREs (Oxygen data not shown) is dependent in the depth of the spin label in the lipid bilayer (Figure 54).

Using the procedure outlined above, I have made accessibility measurements on a monomeric mutant of PLB labeled at position 36 with TOAC (36-TOAC-AFA-PLB). PLB was co-reconstituted with a 2 molar excess of SERCA as previously described. Samples were loaded into a TPX capillary and inserted into a dielectric resonator and saturation rollover curves were acquired. $P_{1/2}$ and $\Delta P_{1/2}$ were determined as described in chapter 2.5 using Equation 13 and the fractional accessibility data is plotted in (Figure 55). Fractional accessibility is commonly used to show how a ligand or other perturbing factor (phosphorylation or SERCA binding here) affects the spin label's accessibility to the PRE and is determined using the following function:

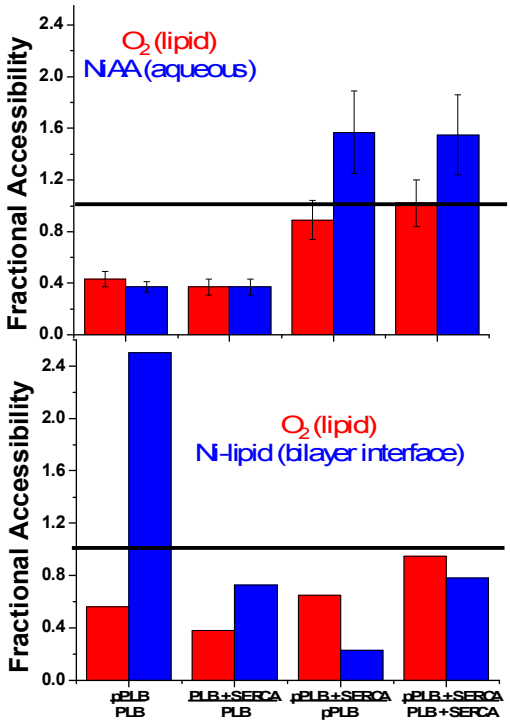

Figure 55. Fractional accessibility of 36-TOAC-AFA-PLB.

Fractional accessibility (FA) values of 36-TOAC-AFA-PLB to O_2 (lipid bilayer), 20mM NiAA (aqueous phase) or Ni-lipid (bilayer interface). In both graphs O_2 data are plotted in red. In the top graph NiAA data are plotted in blue and in the bottom graph DOGS-NTA-Ni data are plotted in blue.

$$FA = \frac{\Lambda P^{*}_{1/2}}{\Lambda P_{1/2}} \qquad \textbf{Equation 25}$$

where $\Delta P_{1/2}^{*}$ and $\Delta P_{1/2}$ are the accessibilities in the presence and absence of the perturbing factor, respectively. While some of the data support our hypothesis, at this point no clear conclusions can be drawn. It is possible that the hypothesis is incorrect but it is also possible and probable that PLB oligomerization and/or binding to SERCA produces steric effects which reduce the collisions with the PREs. In order to test this, Zach James is performing pulsed EPR experiments which can measure the vertical movement of the spin label via though-space interactions.

In addition to the accessibility project, I have also been working on a project to measure the topology of PLB in macroscopically aligned lipid bilayer samples. Data from these experiments will help determine if PLB phosphorylation or SERCA binding changes the topology of PLB in the lipid bilayer and can be used to refine PLB and SERCA-PLB structural models.

The bilayer normal is often used as a reference frame in topological measurements. Consequently, topology can be defined as θ_{AM}, the angle between the molecular director axis, the PLB TM domain for example, and the bilayer normal. If aligned samples are made where the membrane normal is co-linear with the magnetic field, the EPR spectra can be analyzed to determine the topology of the spin-labeled protein

Currently, aligned membrane samples are made using one of two different methods, both of which result in the bilayer normal being aligned with the magnetic field. Mechanically aligned samples are created by first drying proteolipid suspensions on glass plates and then rehydrating the plates in a humidity chamber for several days. The plates are then carefully stacked and sealed to prevent dehydration. The stacked plate sample is

then placed on a flat cell sample holder so the membrane normal may be oriented either perpendicular or parallel to the magnetic field. Bicelles are a fairly new technique for making oriented lipid samples and are made by mixing long chain (usually DMPC) and short chain (usually DHPC) lipids at specific ratios. Instead of forming spherical vesicles, they form disc-like bilayers. Because of their shape, they can be oriented in a magnetic field. In fact, in the presence of a magnetic field, they naturally align so that the membrane normal is perpendicular to the magnetic field. However, at the X-band EPR field strength of ~ 3,500 gauss, the alignment is rather weak. In order to align bicelles at X-band field strengths, the samples are doped with a small amount of lanthanide. The ions bind to the lipid headgroups and produce aligned bicelles at X-band field strength. Dysprosium ions or thulium ions are routinely used to align the bicelles so that the membrane normal is perpendicular or parallel to the magnetic field, respectively.

I have created a model system using a lipid spin labeled at position five (5-PCSL) in the hydrocarbon chain to optimize sample preparation, alignment and data acquisition at X-band field strengths. The 5-PCSL spin label has been extensively used in EPR experiments, including bicelle alignment, over the last two decades and is well characterized. The principal axis of the nitroxide ring is co-linear with the bilayer normal. Consequently, when the bilayer normal is parallel to the magnetic field, the principal axis is parallel with the magnetic field and maximal hyperfine splitting in the spectrum is observed. The opposite is true when the bilayer normal is perpendicular to the magnetic field, i.e. minimal hyperfine splitting is observed (Figure 56A). Spectra from bicelle samples made with 5-PCSL show larger splitting for the thulium doped bicelles than the dysprosium doped bicelles, indicating that the bilayer normal is parallel and perpendicular to the magnetic field, respectively (Figure 56B) No spectral changes are observed in identical samples made with a small amount of AFA-PLB, indicating that the peptide does not affect bicelle alignment. It should be noted that

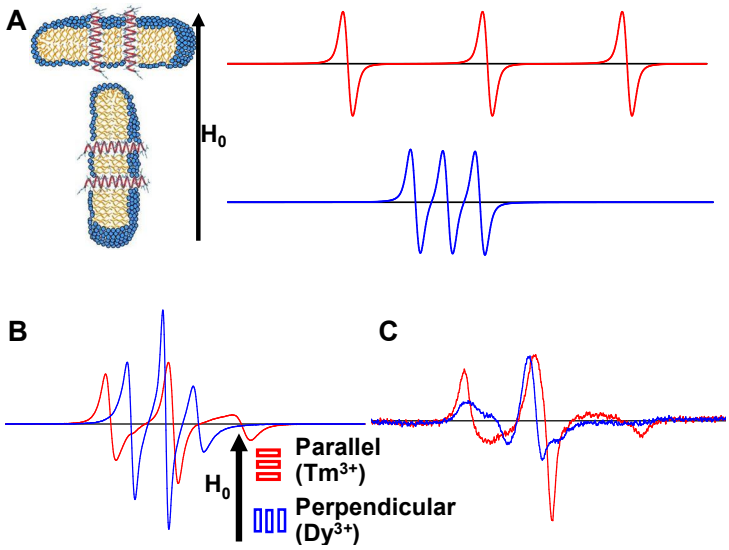

Figure 56. Oriented bicelle spectra.

(A) Illustrations and spectra of bicelles with the bilayer normal oriented parallel (top) and perpendicular (bottom) to the magnetic field, H_0. Spectra were simulated assuming the membrane normal is perfectly aligned with H_0 and there are no orientational distributions due to disorder. (B) Spectra of spin-labeled lipid bicelles $\pm$ unlabeled AFA-PLB doped with thulium (Tm^{3+}) or dysprosium (Dy^{3+}). (C) Spectra of 36-TOAC-AFA-PLB reconstituted into bicelles doped with thulium (Tm^{3+}) or dysprosium (Dy^{3+}).

the splittings and linewidths of the bicelle samples do not match the simulations of perfectly aligned samples with no orientational disorder shown in (Figure 56A). This is due to the fact that the spin label is undergoing rotational motion which results in an angular distribution with respect to the magnetic field that alters the ERP lineshape. For more information, refer to chapter 2.3.

After verifying that thulium doped bicelles containing unlabeled PLB are aligned with the magnetic field, I removed the 5-PCSL and replaced the unlabeled PLB with 36-TOAC-AFA-PLB. The spectra of spin-labeled PLB (Figure 56C) indicate that the TM domain of PLB is co-linear with the bilayer normal as shown by the Veglia lab using solid-state NMR spectroscopy. I have begun using NLSL to fit the oriented spectra using motional parameters obtained from randomly oriented samples to determine the tilt of the PLB transmembrane domain with respect to the bilayer normal (θ_{AM}). I have also developed the technique using oriented lipid bilayers on glass plates to measure $\theta_{AM.}$ The work I have begun will be used as the basis for other graduate students in the lab to measure the topology of PLB domains as a function of phosphorylation and/or SERCA binding to help refine the structural models of PLB and the SERCA-PLB complex.

REFERENCES

1. **Toyoshima, C. and G. Inesi, *Structural basis of ion pumping by Ca2+-ATPase of the sarcoplasmic reticulum.* Annu Rev Biochem, 2004. 73: p. 269-92.**
2. **MacLennan, D.H. and T. Toyofuku, *Regulatory interactions between calcium ATPases and phospholamban.* Soc Gen Physiol Ser, 1996. 51: p. 89-103.**
3. **Inesi, G., et al., *Concerted conformational effects of Ca2+ and ATP are required for activation of sequential reactions in the Ca2+ ATPase (SERCA) catalytic cycle.* Biochemistry, 2006. 45(46): p. 13769-78.**
4. **Chien, K.R., J. Ross, Jr., and M. Hoshijima, *Calcium and heart failure: the cycle game.* Nat Med, 2003. 9(5): p. 508-9.**
5. **Simmerman, H.K. and L.R. Jones, *Phospholamban: protein structure, mechanism of action, and role in cardiac function.* Physiol Rev, 1998. 78(4): p. 921-47.**
6. **Reddy, L.G., L.R. Jones, and D.D. Thomas, *Depolymerization of phospholamban in the presence of calcium pump: a fluorescence energy transfer study.* Biochemistry, 1999. 38(13): p. 3954-62.**
7. **MacLennan, D.H. and E.G. Kranias, *Phospholamban: a crucial regulator of cardiac contractility.* Nat Rev Mol Cell Biol, 2003. 4(7): p. 566-77.**
8. **Cornea, R.L., et al., *Mutation and phosphorylation change the oligomeric structure of phospholamban in lipid bilayers.* Biochemistry, 1997. 36(10): p. 2960-7.**
9. **Wegener, A.D., et al., *Phospholamban phosphorylation in intact ventricles. Phosphorylation of serine 16 and threonine 17 in response to beta-adrenergic stimulation.* J Biol Chem, 1989. 264(19): p. 11468-74.**
10. **Simmerman, H.K., et al., *Sequence analysis of phospholamban. Identification of phosphorylation sites and two major structural domains.* J Biol Chem, 1986. 261(28): p. 13333-41.**
11. **Chen, Z., B.L. Akin, and L.R. Jones, *Ca2+ binding to site I of the cardiac Ca2+ pump is sufficient to dissociate phospholamban.* J Biol Chem, 2010. 285(5): p. 3253-60.**
12. **Chen, Z., et al., *Cross-linking of C-terminal residues of phospholamban to the Ca2+ pump of cardiac sarcoplasmic reticulum to probe spatial and functional interactions within the transmembrane domain.* J Biol Chem, 2006. 281(20): p. 14163-72.**
13. **Jones, L.R., R.L. Cornea, and Z. Chen, *Close proximity between residue 30 of phospholamban and cysteine 318 of the cardiac Ca2+ pump revealed by intermolecular thiol cross-linking.* J Biol Chem, 2002. 277(31): p. 28319-29.**
14. **Kimura, Y., et al., *Phospholamban inhibitory function is activated by depolymerization.* J Biol Chem, 1997. 272(24): p. 15061-4.**
15. **Mueller, B., et al., *Direct detection of phospholamban and sarcoplasmic reticulum Ca-ATPase interaction in membranes using fluorescence resonance energy transfer.* Biochemistry, 2004. 43(27): p. 8754-65.**
16. **Mueller, B., et al., *SERCA structural dynamics induced by ATP and calcium.* Biochemistry, 2004. 43(40): p. 12846-54.**

17. **Karim, C.B., et al., *Phosphorylation-dependent conformational switch in spin-labeled phospholamban bound to SERCA.* J Mol Biol, 2006. 358(4): p. 1032-40.**
18. **Traaseth, N.J., D.D. Thomas, and G. Veglia, *Effects of Ser16 phosphorylation on the allosteric transitions of phospholamban/Ca(2+)-ATPase complex.* J Mol Biol, 2006. 358(4): p. 1041-50.**
19. **Traaseth, N.J., et al., *Structural and dynamic basis of phospholamban and sarcolipin inhibition of Ca(2+)-ATPase.* Biochemistry, 2008. 47(1): p. 3-13.**
20. **Morth, J.P., et al., *Crystal structure of the sodium-potassium pump.* Nature, 2007. 450(7172): p. 1043-9.**
21. **Beevers, A.J. and A. Kukol, *Phospholemman transmembrane structure reveals potential interactions with Na+/K+-ATPase.* J Biol Chem, 2007. 282(45): p. 32742-8.**
22. **Beevers, A.J. and A. Kukol, *Secondary structure, orientation, and oligomerization of phospholemman, a cardiac transmembrane protein.* Protein Sci, 2006. 15(5): p. 1127-32.**
23. **Teriete, P., et al., *Structure of the Na,K-ATPase regulatory protein FXYD1 in micelles.* Biochemistry, 2007. 46(23): p. 6774-83.**
24. **Bibert, S., et al., *Phosphorylation of phospholemman (FXYD1) by protein kinases A and C modulates distinct Na,K-ATPase isozymes.* J Biol Chem, 2008. 283(1): p. 476-86.**
25. **Crambert, G., et al., *Phospholemman (FXYD1) associates with Na,K-ATPase and regulates its transport properties.* Proc Natl Acad Sci U S A, 2002. 99(17): p. 11476-81.**
26. **Strehler, E.E., et al., *Plasma-membrane Ca(2+) pumps: structural diversity as the basis for functional versatility.* Biochem Soc Trans, 2007. 35(Pt 5): p. 919-22.**
27. **Periasamy, M. and A. Kalyanasundaram, *SERCA pump isoforms: their role in calcium transport and disease.* Muscle Nerve, 2007. 35(4): p. 430-42.**
28. **Moller, J.V., et al., *Transport mechanism of the sarcoplasmic reticulum Ca2+ -ATPase pump.* Curr Opin Struct Biol, 2005. 15(4): p. 387-93.**
29. **MacLennan, D.H., W.J. Rice, and N.M. Green, *The mechanism of Ca2+ transport by sarco(endo)plasmic reticulum Ca2+-ATPases.* J Biol Chem, 1997. 272(46): p. 28815-8.**
30. **MacLennan, D.H. and N.M. Green, *Structural biology. Pumping ions.* Nature, 2000. 405(6787): p. 633-4.**
31. **Vilsen, B., *Structure-function relationships in the Ca(2+)-ATPase of sarcoplasmic reticulum studied by use of the substrate analogue CrATP and site-directed mutagenesis. Comparison with the Na+,K(+)-ATPase.* Acta Physiol Scand Suppl, 1995. 624: p. 1-146.**
32. **Andersen, J.P. and B. Vilsen, *Structure-function relationships of cation translocation by Ca(2+)- and Na+, K(+)-ATPases studied by site-directed mutagenesis.* FEBS Lett, 1995. 359(2-3): p. 101-6.**

33. **Mahaney, J.E., J.P. Froehlich, and D.D. Thomas, *Conformational transitions of the sarcoplasmic reticulum Ca-ATPase studied by time-resolved EPR and quenched-flow kinetics.* Biochemistry, 1995. 34(14): p. 4864-79.**
34. **Toyoshima, C. and H. Nomura, *Structural changes in the calcium pump accompanying the dissociation of calcium.* Nature, 2002. 418(6898): p. 605-11.**
35. **Jensen, A.O., et al., *Chronic diseases requiring hospitalization and risk of non-melanoma skin cancers--a population based study from Denmark.* J Invest Dermatol, 2008. 128(4): p. 926-31.**
36. **Moller, J.V., et al., *The structural basis for coupling of Ca2+ transport to ATP hydrolysis by the sarcoplasmic reticulum Ca2+-ATPase.* J Bioenerg Biomembr, 2005. 37(6): p. 359-64.**
37. **Obara, K., et al., *Structural role of countertransport revealed in Ca(2+) pump crystal structure in the absence of Ca(2+).* Proc Natl Acad Sci U S A, 2005. 102(41): p. 14489-96.**
38. **Ogawa, H., et al., *Structure of the Ca2+ pump of sarcoplasmic reticulum: a view along the lipid bilayer at 9-A resolution.* Biophys J, 1998. 75(1): p. 41-52.**
39. **Ma, H., et al., *Functional and structural roles of critical amino acids within the"N", "P", and "A" domains of the Ca2+ ATPase (SERCA) headpiece.* Biochemistry, 2005. 44(22): p. 8090-100.**
40. **Zhang, Z., et al., *Detailed characterization of the cooperative mechanism of Ca(2+) binding and catalytic activation in the Ca(2+) transport (SERCA) ATPase.* Biochemistry, 2000. 39(30): p. 8758-67.**
41. **Olesen, C., et al., *The structural basis of calcium transport by the calcium pump.* Nature, 2007. 450(7172): p. 1036-42.**
42. **Hua, S., et al., *Functional role of "N" (nucleotide) and "P" (phosphorylation) domain interactions in the sarcoplasmic reticulum (SERCA) ATPase.* Biochemistry, 2002. 41(7): p. 2264-72.**
43. **Xu, C., et al., *Specific structural requirements for the inhibitory effect of thapsigargin on the Ca2+ ATPase SERCA.* J Biol Chem, 2004. 279(17): p. 17973-9.**
44. **Stokes, D.L. and N.M. Green, *Three-dimensional crystals of CaATPase from sarcoplasmic reticulum. Symmetry and molecular packing.* Biophys J, 1990. 57(1): p. 1-14.**
45. **Toyoshima, C., et al., *Crystal structure of the calcium pump of sarcoplasmic reticulum at 2.6 A resolution.* Nature, 2000. 405(6787): p. 647-55.**
46. **Winters, D.L., et al., *Interdomain fluorescence resonance energy transfer in SERCA probed by cyan-fluorescent protein fused to the actuator domain.* Biochemistry, 2008. 47(14): p. 4246-56.**
47. **Zamoon, J., et al., *NMR solution structure and topological orientation of monomeric phospholamban in dodecylphosphocholine micelles.* Biophys J, 2003. 85(4): p. 2589-98.**
48. **Karim, C.B., et al., *Cysteine reactivity and oligomeric structures of phospholamban and its mutants.* Biochemistry, 1998. 37(35): p. 12074-81.**

49. **Karim, C.B., et al., *Synthetic null-cysteine phospholamban analogue and the corresponding transmembrane domain inhibit the Ca-ATPase.* Biochemistry, 2000. 39(35): p. 10892-7.**
50. **Metcalfe, E., Zamoon, J, Thomas, DD, and Veglia, G, *(1)H/(15)N heteronuclear NMR spectroscopy shows four dynamic domains for phospholamban reconstituted in dodecylphosphocholine micelles.* Biophys J, 2004. 87(2): p. 1205-14.**
51. **Karim, C.B., et al., *Phospholamban structural dynamics in lipid bilayers probed by a spin label rigidly coupled to the peptide backbone.* Proc Natl Acad Sci U S A, 2004. 101(40): p. 14437-42.**
52. **Traaseth, N.J., et al., *Structure and topology of monomeric phospholamban in lipid membranes determined by a hybrid solution and solid-state NMR approach.* Proc Natl Acad Sci U S A, 2009. 106(25): p. 10165-70.**
53. **Jones, L.R. and L.J. Field, *Residues 2-25 of phospholamban are insufficient to inhibit Ca2+ transport ATPase of cardiac sarcoplasmic reticulum.* J Biol Chem, 1993. 268(16): p. 11486-8.**
54. **Lockwood, N.A., et al., *Structure and function of integral membrane protein domains resolved by peptide-amphiphiles: application to phospholamban.* Biopolymers, 2003. 69(3): p. 283-92.**
55. **Kirby, T.L., C.B. Karim, and D.D. Thomas, *Electron paramagnetic resonance reveals a large-scale conformational change in the cytoplasmic domain of phospholamban upon binding to the sarcoplasmic reticulum Ca-ATPase.* Biochemistry, 2004. 43(19): p. 5842-52.**
56. **Kim, T., J. Lee, and W. Im, *Molecular dynamics studies on structure and dynamics of phospholamban monomer and pentamer in membranes.* Proteins, 2009. 76(1): p. 86-98.**
57. **Pantano, S. and E. Carafoli, *The role of phosphorylation on the structure and dynamics of phospholamban: a model from molecular simulations.* Proteins, 2007. 66(4): p. 930-40.**
58. **Sugita, Y., et al., *Structural changes in the cytoplasmic domain of phospholamban by phosphorylation at Ser16: a molecular dynamics study.* Biochemistry, 2006. 45(39): p. 11752-61.**
59. **Metcalfe, E.E., N.J. Traaseth, and G. Veglia, *Serine 16 phosphorylation induces an order-to-disorder transition in monomeric phospholamban.* Biochemistry, 2005. 44(11): p. 4386-96.**
60. **Thomas, D.D., et al., *Direct spectroscopic detection of molecular dynamics and interactions of the calcium pump and phospholamban.* Ann N Y Acad Sci, 1998. 853: p. 186-94.**
61. **Tatulian, S.A., et al., *Secondary structure and orientation of phospholamban reconstituted in supported bilayers from polarized attenuated total reflection FTIR spectroscopy.* Biochemistry, 1995. 34(13): p. 4448-56.**
62. **Arkin, I.T., et al., *Structural model of the phospholamban ion channel complex in phospholipid membranes.* J Mol Biol, 1995. 248(4): p. 824-34.**

63. **Oxenoid, K. and J.J. Chou, *The structure of phospholamban pentamer reveals a channel-like architecture in membranes.* Proc Natl Acad Sci U S A, 2005. 102(31): p. 10870-5.**
64. **Robia, S.L., N.C. Flohr, and D.D. Thomas, *Phospholamban pentamer quaternary conformation determined by in-gel fluorescence anisotropy.* Biochemistry, 2005. 44(11): p. 4302-11.**
65. **Traaseth, N.J., et al., *Spectroscopic validation of the pentameric structure of phospholamban.* Proc Natl Acad Sci U S A, 2007. 104(37): p. 14676-81.**
66. **Stokes, D.L., et al., *Interactions between Ca2+-ATPase and the pentameric form of phospholamban in two-dimensional co-crystals.* Biophys J, 2006. 90(11): p. 4213-23.**
67. **Arkin, I.T., et al., *Structural organization of the pentameric transmembrane alpha-helices of phospholamban, a cardiac ion channel.* Embo J, 1994. 13(20): p. 4757-64.**
68. **Simmerman, H.K., et al., *A leucine zipper stabilizes the pentameric membrane domain of phospholamban and forms a coiled-coil pore structure.* J Biol Chem, 1996. 271(10): p. 5941-6.**
69. **Abu-Baker, S. and G.A. Lorigan, *Phospholamban and its phosphorylated form interact differently with lipid bilayers: a 31P, 2H, and 13C solid-state NMR spectroscopic study.* Biochemistry, 2006. 45(44): p. 13312-22.**
70. **Clayton, J.C., E. Hughes, and D.A. Middleton, *The cytoplasmic domains of phospholamban and phospholemman associate with phospholipid membrane surfaces.* Biochemistry, 2005. 44(51): p. 17016-26.**
71. **Clayton, J.C., E. Hughes, and D.A. Middleton, *Spectroscopic studies of phospholamban variants in phospholipid bilayers.* Biochem Soc Trans, 2005. 33(Pt 5): p. 913-5.**
72. **Hughes, E., J.C. Clayton, and D.A. Middleton, *Probing the oligomeric state of phospholamban variants in phospholipid bilayers from solid-state NMR measurements of rotational diffusion rates.* Biochemistry, 2005. 44(10): p. 4055-66.**
73. **Hutter, M.C., et al., *A structural model of the complex formed by phospholamban and the calcium pump of sarcoplasmic reticulum obtained by molecular mechanics.* Chembiochem, 2002. 3(12): p. 1200-8.**
74. **Toyoshima, C., et al., *Modeling of the inhibitory interaction of phospholamban with the Ca2+ ATPase.* Proc Natl Acad Sci U S A, 2003. 100(2): p. 467-72.**
75. **Zamoon, J., et al., *Mapping the interaction surface of a membrane protein: unveiling the conformational switch of phospholamban in calcium pump regulation.* Proc Natl Acad Sci U S A, 2005. 102(13): p. 4747-52.**
76. **Odermatt, A., et al., *Mutations in the gene-encoding SERCA1, the fast-twitch skeletal muscle sarcoplasmic reticulum Ca2+ ATPase, are associated with Brody disease.* Nat Genet, 1996. 14(2): p. 191-4.**
77. **Dhitavat, J., et al., *Mutations in the sarcoplasmic/endoplasmic reticulum Ca2+ ATPase isoform cause Darier's disease.* J Invest Dermatol, 2003. 121(3): p. 486-9.**

78. **Dash, R., et al., *Gender influences on sarcoplasmic reticulum Ca2+-handling in failing human myocardium.* J Mol Cell Cardiol, 2001. 33(7): p. 1345-53.**
79. **Meyer, M., et al., *Alterations of sarcoplasmic reticulum proteins in failing human dilated cardiomyopathy.* Circulation, 1995. 92(4): p. 778-84.**
80. **Pieske, B., et al., *Alterations in intracellular calcium handling associated with the inverse force-frequency relation in human dilated cardiomyopathy.* Circulation, 1995. 92(5): p. 1169-78.**
81. **Schmitt, J.P., et al., *Dilated cardiomyopathy and heart failure caused by a mutation in phospholamban.* Science, 2003. 299(5611): p. 1410-3.**
82. **Haghighi, K., et al., *A mutation in the human phospholamban gene, deleting arginine 14, results in lethal, hereditary cardiomyopathy.* Proc Natl Acad Sci U S A, 2006. 103(5): p. 1388-93.**
83. **Haghighi, K., et al., *Human phospholamban null results in lethal dilated cardiomyopathy revealing a critical difference between mouse and human.* J Clin Invest, 2003. 111(6): p. 869-76.**
84. **Medin, M., et al., *Mutational screening of phospholamban gene in hypertrophic and idiopathic dilated cardiomyopathy and functional study of the PLN -42 C>G mutation.* Eur J Heart Fail, 2007. 9(1): p. 37-43.**
85. **Minamisawa, S., et al., *Mutation of the phospholamban promoter associated with hypertrophic cardiomyopathy.* Biochem Biophys Res Commun, 2003. 304(1): p. 1-4.**
86. **Haghighi, K., et al., *A human phospholamban promoter polymorphism in dilated cardiomyopathy alters transcriptional regulation by glucocorticoids.* Hum Mutat, 2008. 29(5): p. 640-7.**
87. **Campbell, I.D. and R.A. Dwek, *Biological Spectroscopy*. 1984, Menlo Park, CA: Benjamin/Cummings Publishing Company.**
88. **Thomas, D.D., *Saturation transfer EPR.* Trends Biochem Sci, 1977. 2: p. N62-N63.**
89. **Altenbach, C., et al., *A collision gradient method to determine the immersion depth of nitroxides in lipid bilayers: application to spin-labeled mutants of bacteriorhodopsin.* Proc Natl Acad Sci U S A, 1994. 91(5): p. 1667-71.**
90. **Pake, G.E., *Nuclear Resonance Absorption in Hydrated Crystals: Fine Structure of the Proton Line.* Journal of Chemical Physics, 1948. 16: p. 327-336.**
91. **Kovacs, R.J., et al., *Phospholamban forms Ca2+-selective channels in lipid bilayers.* J Biol Chem, 1988. 263(34): p. 18364-8.**
92. **Smith, S.O., et al., *Helical structure of phospholamban in membrane bilayers.* J Mol Biol, 2001. 313(5): p. 1139-48.**
93. **Metcalfe, E.E., et al., *(1)H/(15)N heteronuclear NMR spectroscopy shows four dynamic domains for phospholamban reconstituted in dodecylphosphocholine micelles.* Biophys J, 2004. 87(2): p. 1205-14.**
94. **Traaseth, N.J., et al., *Structural dynamics and topology of phospholamban in oriented lipid bilayers using multidimensional solid-state NMR.* Biochemistry, 2006. 45(46): p. 13827-34.**

95. **Mascioni, A., et al., *Solid-state NMR and rigid body molecular dynamics to determine domain orientations of monomeric phospholamban.* J Am Chem Soc, 2002. 124(32): p. 9392-3.**
96. **Dave, P.C., et al., *Investigating structural changes in the lipid bilayer upon insertion of the transmembrane domain of the membrane-bound protein phospholamban utilizing 31P and 2H solid-state NMR spectroscopy.* Biophys J, 2004. 86(3): p. 1564-73.**
97. **Buck, B., et al., *Overexpression, purification, and characterization of recombinant Ca-ATPase regulators for high-resolution solution and solid-state NMR studies.* Protein Expr Purif, 2003. 30(2): p. 253-61.**
98. **Opella, S.J. and F.M. Marassi, *Structure determination of membrane proteins by NMR spectroscopy.* Chem Rev, 2004. 104(8): p. 3587-606.**
99. **Marassi, F.M. and S.J. Opella, *NMR structural studies of membrane proteins.* Curr Opin Struct Biol, 1998. 8(5): p. 640-8.**
100. **Luca, S., H. Heise, and M. Baldus, *High-resolution solid-state NMR applied to polypeptides and membrane proteins.* Acc Chem Res, 2003. 36(11): p. 858-65.**
101. **Wu, C.H., Ramamoorthy, A., Opella, S.J., J Mag Res, 1994. 109: p. 270-272.**
102. **Wang, J., et al., *Imaging membrane protein helical wheels.* J Magn Reson, 2000. 144(1): p. 162-7.**
103. **Marassi, F.M. and S.J. Opella, *A solid-state NMR index of helical membrane protein structure and topology.* J Magn Reson, 2000. 144(1): p. 150-5.**
104. **Mascioni, A. and G. Veglia, *Theoretical analysis of residual dipolar coupling patterns in regular secondary structures of proteins.* J Am Chem Soc, 2003. 125(41): p. 12520-6.**
105. **Buffy, J.J., et al., *Two-dimensional solid-state NMR reveals two topologies of sarcolipin in oriented lipid bilayers.* Biochemistry, 2006. 45(36): p. 10939-46.**
106. **Nevzorov, A.A. and S.J. Opella, *Structural fitting of PISEMA spectra of aligned proteins.* J Magn Reson, 2003. 160(1): p. 33-9.**
107. **Adams, P.D., et al., *Computational searching and mutagenesis suggest a structure for the pentameric transmembrane domain of phospholamban.* Nat Struct Biol, 1995. 2(2): p. 154-62.**
108. **Columbus, L. and W.L. Hubbell, *A new spin on protein dynamics.* Trends Biochem Sci, 2002. 27(6): p. 288-95.**
109. **Pannier, M., et al., *Dead-time free measurement of dipole-dipole interactions between electron spins.* J Magn Reson, 2000. 142(2): p. 331-40.**
110. **Chou, J.J., et al., *Micelle-induced curvature in a water-insoluble HIV-1 Env peptide revealed by NMR dipolar coupling measurement in stretched polyacrylamide gel.* J Am Chem Soc, 2002. 124(11): p. 2450-1.**
111. **Tamm, L.K., et al., *Structure, dynamics and function of the outer membrane protein A (OmpA) and influenza hemagglutinin fusion domain in detergent micelles by solution NMR.* FEBS Lett, 2003. 555(1): p. 139-43.**
112. **Fernandez, C. and K. Wuthrich, *NMR solution structure determination of membrane proteins reconstituted in detergent micelles.* FEBS Lett, 2003. 555(1): p. 144-50.**

113. **Buffy, J.J., et al., *Defining the intramembrane binding mechanism of sarcolipin to calcium ATPase using solution NMR spectroscopy.* J Mol Biol, 2006. 358(2): p. 420-9.**
114. **Tolman, J.R., et al., *Structural and dynamic analysis of residual dipolar coupling data for proteins.* J Am Chem Soc, 2001. 123(7): p. 1416-24.**
115. **Tjandra, N. and A. Bax, *Direct measurement of distances and angles in biomolecules by NMR in a dilute liquid crystalline medium.* Science, 1997. 278(5340): p. 1111-4.**
116. **Bax, A., *Weak alignment offers new NMR opportunities to study protein structure and dynamics.* Protein Sci, 2003. 12(1): p. 1-16.**
117. **Ryabov, Y. and D. Fushman, *Analysis of interdomain dynamics in a two-domain protein using residual dipolar couplings together with 15N relaxation data.* Magn Reson Chem, 2006. 44 Spec No: p. S143-51.**
118. **Al-Hashimi, H.M., et al., *Variation of molecular alignment as a means of resolving orientational ambiguities in protein structures from dipolar couplings.* J Magn Reson, 2000. 143(2): p. 402-6.**
119. **Marassi, F.M. and S.J. Opella, *Simultaneous assignment and structure determination of a membrane protein from NMR orientational restraints.* Protein Sci, 2003. 12(3): p. 403-11.**
120. **Nozaki, Y., J.A. Reynolds, and C. Tanford, *Conformational states of a hydrophobic protein. The coat protein of fd bacteriophage.* Biochemistry, 1978. 17(7): p. 1239-46.**
121. **Thiriot, D.S., et al., *Structure of the coat protein in Pf1 bacteriophage determined by solid-state NMR spectroscopy.* J Mol Biol, 2004. 341(3): p. 869-79.**
122. **Epand, R.M. and H.J. Vogel, *Diversity of antimicrobial peptides and their mechanisms of action.* Biochim Biophys Acta, 1999. 1462(1-2): p. 11-28.**
123. **Engelman, D.M., et al., *Membrane protein folding: beyond the two stage model.* FEBS Lett, 2003. 555(1): p. 122-5.**
124. **Popot, J.L. and D.M. Engelman, *Helical membrane protein folding, stability, and evolution.* Annu Rev Biochem, 2000. 69: p. 881-922.**
125. **Karim, C.B., Z. Zhang, and D.D. Thomas, *Synthesis of TOAC spin-labeled proteins and reconstitution in lipid membranes.* Nat Protoc, 2007. 2(1): p. 42-9.**
126. **Gor'kov, P.L., et al., *Using low-E resonators to reduce RF heating in biological samples for static solid-state NMR up to 900 MHz.* J Magn Reson, 2007. 185(1): p. 77-93.**
127. **Sen, K.I., et al., *Mn(II) binding by the anthracis repressor from Bacillus anthracis.* Biochemistry, 2006. 45(13): p. 4295-303.**
128. **Bennett, A.E., Rienstra, C.M., Auger, M., Lakshmi, K.V., Griffin, R.G., J Chem Phys, 1995. 103: p. 6951-6958.**
129. **Delaglio, F., et al., *NMRPipe: a multidimensional spectral processing system based on UNIX pipes.* J Biomol NMR, 1995. 6(3): p. 277-93.**
130. **Johnson, B.A., Blevins, R.A., J Biolmol NMR, 1994. 4: p. 603-614.**
131. **Anisimov, O.A., Nikitaev, A.T., Zamaraev, K.L., Molin, Theor Exper Chem, 1971. 7: p. 556-559.**

132. **Gross, A. and W.L. Hubbell, *Identification of protein side chains near the membrane-aqueous interface: a site-directed spin labeling study of KcsA.* Biochemistry, 2002. 41(4): p. 1123-8.**
133. **Jeschke, G., et al., *Sensitivity enhancement in pulse EPR distance measurements.* J Magn Reson, 2004. 169(1): p. 1-12.**
134. **Wittig, I., H.P. Braun, and H. Schagger, *Blue native PAGE.* Nat Protoc, 2006. 1(1): p. 418-28.**
135. **Schagger, H., *Tricine-SDS-PAGE.* Nat Protoc, 2006. 1(1): p. 16-22.**
136. **Lindemann, J.P., et al., *beta-Adrenergic stimulation of phospholamban phosphorylation and Ca2+- ATPase activity in guinea pig ventricles.* J Biol Chem, 1983. 258(1): p. 464-71.**
137. **Sande, J.B., et al., *Reduced level of serine(16) phosphorylated phospholamban in the failing rat myocardium: a major contributor to reduced SERCA2 activity.* Cardiovasc Res, 2002. 53(2): p. 382-91.**
138. **Schmidt, A.G., I. Edes, and E.G. Kranias, *Phospholamban: a promising therapeutic target in heart failure?* Cardiovasc Drugs Ther, 2001. 15(5): p. 387-96.**
139. **Minamisawa, S., et al., *Chronic phospholamban-sarcoplasmic reticulum calcium ATPase interaction is the critical calcium cycling defect in dilated cardiomyopathy.* Cell, 1999. 99(3): p. 313-22.**
140. **MacLennan, D.H., Y. Kimura, and T. Toyofuku, *Sites of regulatory interaction between calcium ATPases and phospholamban.* Ann N Y Acad Sci, 1998. 853: p. 31-42.**
141. **Negash, S., et al., *Phospholamban remains associated with the Ca2+- and Mg2+-dependent ATPase following phosphorylation by cAMP-dependent protein kinase.* Biochem J, 2000. 351(Pt 1): p. 195-205.**
142. **Chen, B. and D.J. Bigelow, *Phosphorylation induces a conformational transition near the lipid-water interface of phospholamban reconstituted with the Ca-ATPase.* Biochemistry, 2002. 41(47): p. 13965-72.**
143. **Li, J., D.J. Bigelow, and T.C. Squier, *Conformational changes within the cytosolic portion of phospholamban upon release of Ca-ATPase inhibition.* Biochemistry, 2004. 43(13): p. 3870-9.**
144. **Li, J., et al., *Phospholamban binds in a compact and ordered conformation to the Ca-ATPase.* Biochemistry, 2004. 43(2): p. 455-63.**
145. **Li, M., et al., *A fluorescence energy transfer method for analyzing protein oligomeric structure: application to phospholamban.* Biophys J, 1999. 76(5): p. 2587-99.**
146. **Autry, J.M. and L.R. Jones, *Functional Co-expression of the canine cardiac Ca2+ pump and phospholamban in Spodoptera frugiperda (Sf21) cells reveals new insights on ATPase regulation.* J Biol Chem, 1997. 272(25): p. 15872-80.**
147. **Reddy, L.G., et al., *Co-reconstitution of phospholamban mutants with the Ca-ATPase reveals dependence of inhibitory function on phospholamban structure.* J Biol Chem, 1999. 274(12): p. 7649-55.**

148. **Jones, L.R., R.L. Cornea, and Z. Chen, *Close Proximity between Residue 30 of Phospholamban and Cysteine 318 of the Cardiac Ca2+ Pump Revealed by Intermolecular Thiol Cross-linking.* J Biol Chem, 2002. 277(31): p. 28319-29.**
149. **Traaseth, N.J., D.D. Thomas, and G. Veglia, *Effects of Ser16 Phosphorylation on the Allosteric Transitions of Phospholamban/Ca2+ -ATPase complex.* J Mol Biol, 2005. submitted.**
150. **Karim, C.B., et al., *Role of cysteine residues in structural stability and function of a transmembrane helix bundle.* J Biol Chem, 2001. 26: p. 26.**
151. **Berndt, P., G.B. Fields, and M. Tirrell, *Synthetic lipidation of peptides and amino acids: monolayer structure and properties.* Journal of the American Chemical Society, 1995. 117: p. 9515-9522.**
152. **Reddy, L.G., et al., *Defining the molecular components of calcium transport regulation in a reconstituted membrane system.* Biochemistry, 2003. 42(15): p. 4585-92.**
153. **Mayer, E.J., et al., *Characterization and quantitation of phospholamban and its phosphorylation state using antibodies.* Biochem Biophys Res Commun, 2000. 267(1): p. 40-8.**
154. **Fabiato, A. and F. Fabiato, *Calculator programs for computing the composition of the solutions containing multiple metals and ligands used for experiments in skinned muscle cells.* J Physiol (Paris), 1979. 75(5): p. 463-505.**
155. **Lowry, O.H., et al., *Protein measurement with the Folin phenol reagent.* J Biol Chem, 1951. 193(1): p. 265-75.**
156. **Budil, D.E., et al., *Nonlinear-least-squares analysis of slow-motion EPR spectra in one and two dimensions using a modified Levenberg-Marquardt algorithm.* J. Magn. Reson., 1996. A 120: p. 155 - 189.**
157. **Bers, D.M., *Cardiac excitation-contraction coupling.* Nature, 2002. 415(6868): p. 198-205.**
158. **Katz, A.M., M. Tada, and M.A. Kirchberger, *Control of calcium transport in the myocardium by the cyclic AMP-Protein kinase system.* Adv Cyclic Nucleotide Res, 1975. 5: p. 453-72.**
159. **Tada, M. and M. Kadoma, *Regulation of the Ca2+ pump ATPase by cAMP-dependent phosphorylation of phospholamban.* Bioessays, 1989. 10(5): p. 157-63.**
160. **Robia, S.L., et al., *Forster transfer recovery reveals that phospholamban exchanges slowly from pentamers but rapidly from the SERCA regulatory complex.* Circ Res, 2007. 101(11): p. 1123-9.**
161. **Nesmelov, Y.E., et al., *Rotational dynamics of phospholamban determined by multifrequency electron paramagnetic resonance.* Biophys J, 2007. 93(8): p. 2805-12.**
162. **Kimura, Y., et al., *Phospholamban domain Ib mutations influence functional interactions with the Ca2+-ATPase isoform of cardiac sarcoplasmic reticulum.* J Biol Chem, 1998. 273(23): p. 14238-41.**
163. **Kimura, Y., et al., *Phospholamban domain I/cytochrome b5 transmembrane sequence chimeras do not inhibit SERCA2a.* FEBS Lett, 1998. 425(3): p. 509-12.**

164. **Kimura, Y., et al., *Phospholamban regulates the Ca2+-ATPase through intramembrane interactions.* J Biol Chem, 1996. 271(36): p. 21726-31.**
165. **Reddy, L.G., et al., *Functional reconstitution of recombinant phospholamban with rabbit skeletal Ca(2+)-ATPase.* J Biol Chem, 1995. 270(16): p. 9390-7.**
166. **Toyofuku, T., et al., *Amino acids Glu2 to Ile18 in the cytoplasmic domain of phospholamban are essential for functional association with the Ca(2+)-ATPase of sarcoplasmic reticulum.* J Biol Chem, 1994. 269(4): p. 3088-94.**
167. **Reddy, L.G., et al., *Purified, reconstituted cardiac Ca2+-ATPase is regulated by phospholamban but not by direct phosphorylation with Ca2+/calmodulin-dependent protein kinase.* J Biol Chem, 1996. 271(25): p. 14964-70.**
168. **Bryan, P.M., et al., *A sensitive method for determining the phosphorylation status of natriuretic peptide receptors: cGK-Ialpha does not regulate NPR-A.* Biochemistry, 2006. 45(4): p. 1295-303.**
169. **Squier, T.C. and D.D. Thomas, *Methodology for increased precision in saturation transfer electron paramagnetic resonance studies of rotational dynamics.* Biophys J, 1986. 49(4): p. 921-35.**
170. **Thompson, A.R., et al., *Structural dynamics of the actomyosin complex probed by a bifunctional spin label that cross-links SH1 and SH2.* Biophys J, 2008. 95(11): p. 5238-46.**
171. **Klein, J.C., et al., *Actin-binding cleft closure in myosin II probed by site-directed spin labeling and pulsed EPR.* Proc Natl Acad Sci U S A, 2008. 105(35): p. 12867-72.**
172. **Steinhoff, H.J., *Inter- and intra-molecular distances determined by EPR spectroscopy and site-directed spin labeling reveal protein-protein and protein-oligonucleotide interaction.* Biol Chem, 2004. 385(10): p. 913-20.**
173. **Squier, T.C. and D.D. Thomas, *Applications of new saturation transfer electron paramagnetic resonance methodology to the rotational dynamics of the Ca-ATPase in sarcoplasmic reticulum membranes.* Biophys J, 1986. 49(4): p. 937-42.**
174. **Hou, Z., E.M. Kelly, and S.L. Robia, *Phosphomimetic mutations increase phospholamban oligomerization and alter the structure of its regulatory complex.* J Biol Chem, 2008. 283(43): p. 28996-9003.**